

University of Southern Denmark

PhD Thesis

**Linear and Nonlinear Plasmonics
with Monocrystalline Gold Flakes**

Author:

Sergejs Boroviks

Supervisors:

Prof. N. Asger Mortensen

Prof. Sergey I. Bozhevolnyi

Assist. Prof. Christian Wolff

*A thesis submitted in partial fulfillment of the requirements for the degree of
Doctor of Philosophy at the*

Centre for Nano Optics

Mads Clausen Institute

December 2020

Linear and Nonlinear Plasmonics with Monocrystalline Gold Flakes

PhD Thesis

December 31, 2020

Author: Sergejs Boroviks

Copyright: Reproduction of this publication in whole or in part must include the customary bibliographic citation, including author attribution, title, etc.

University of Southern Denmark
SDU Nano Optics, Campusvej 55, 5230 Odense M, Denmark
https://sdu.dk/en/0m_SDU/Institutter_centre/NanoOptics

Quantum Plasmonics group
<https://mortensen-lab.org/>

Abstract

Modern plasmonics strives to meet the demands of next-generation quantum technologies while opening new research frontiers in mesoscopic solid-state physics. However, the success of these advancements largely depends on the reduction of electromagnetic losses in metallic materials, which constitutes the most ubiquitous problem of current nanoplasmonic devices.

This thesis presents experimental investigations of the plasmonic properties of (quasi-) monocrystalline gold flakes, which emerged recently as a material platform to supersede the traditionally-used polycrystalline gold films. First, the optical response in the linear regime, including nonlocal effects, is discussed in detail, and prospective functionalities for advanced plasmonic devices are experimentally demonstrated. Second, the nonlinear response arising from the interaction of crystalline gold with intense ultrashort light pulses is considered, with experiments revealing that monocrystalline flakes produce a strong anisotropic second-order nonlinear response which is markedly absent in polycrystalline films. In addition, two-photon luminescence microscopy is used to study the nonlinear absorption dynamics in gold flakes that are few tens of nanometers in thickness, exploiting their strong intrinsic third-order susceptibility. Preliminary results indicate that hot carrier excitation and relaxation dynamics is significantly altered when the gold thickness approaches mesoscopic dimensions.

The results presented in this thesis confirm that monocrystalline gold flakes are among the best candidates for the experimental exploration of nonlocal and nonlinear plasmonic phenomena, and can be used for substantial improvement of existing plasmonic devices.

Resumé

Moderne plasmonik stræber efter at imødekomme behovene i den næste generations kvanteteknologier og åbne nye grænser inden for forskning i mesoskopisk faststoffysik. Imidlertid afhænger succesen af disse fremskridt stort set af evnen til at reducere de elektromagnetiske tab i metalliske materialer, hvilket gør det mest allestedsnærværende problem med de nuværende nanoplasmoniske enheder.

Denne ph.d.- afhandling præsenterer en eksperimentel undersøgelse af de plasmoniske egenskaber af (kvasi-) monokrystallinske guldfleger, som for nylig opstod som en materialeplatform til at erstatte de traditionelt anvendte polykrystallinske guldfilm. For det første diskuteres den optiske respons i det lineære regime, inklusive ikke-lokale effekter, og potentielle anvendelser i de avancerede plasmoniske enheder demonstreres eksperimentelt. For det andet overvejes det ikke-lineære respons, der opstår som følge af interaktionen mellem krystallinsk guld og ultrakorte lysimpulser. Udførte eksperimenter viser, at monokrystallinske flager producerer en stærk, anisotrop anden ordens ikke-lineær respons, som er markant fraværende i polykrystallinske film. Derudover anvendes to-foton luminescensmikroskopi til at studere den ikke-lineære absorptionsdynamik i guldfleger, der har få snesevis af nanometer i tykkelse og udnytter deres stærke følsomhed af tredje orden. Foreløbige resultater indikerer, at varmebærerens excitation og afslapningsdynamik er signifikant ændret, når gulddykkelsen nærmer sig mesoskopiske dimensioner.

Resultaterne præsenteret i denne afhandling bekræfter, at de monokrystallinske guldfleger er blandt de bedste kandidater til den eksperimentelle udforskning af ikke-lokale og ikke-lineære plasmoniske fænomener og kan bruges til væsentlig forbedring af de eksisterende plasmoniske enheder.

Acknowledgments

First and for most, I must thank my supervisor, Prof N. Asger Mortensen, and co-supervisors, Prof. Sergey I. Bozhevolnyi and Assist. Prof. Christian Wolff for guiding me throughout my PhD studies. It is a great honour and luck to begin the academic carrier under the supervision of respected professors. In particular, I am grateful to Asger for his encouragement, support and trust in my ideas and findings, and for creating a friendly, collaborative and motivating environment in the Quantum Plasmonics group; to Sergey, who is always critical but fair and supportive, and without whom my PhD would not even begin; to Christian, who always keeps the door to his office open for all kind of bizarre questions about the physics, life, the universe and everything.

I would like to extend my thanks to Dr. Jer-Shing Huang and his group members for enlightening discussions, fruitful collaboration and a great time which I spent in Jena during my research stay. I am also thankful to all my colleagues and ex-colleagues at the Centre for Nano Optics. Especially, to Dr. Volodymyr Zenin, who is always suggesting fresh ideas and helping with all kinds of troubles; to Dr. Francesco Todisco for showing me how fun the optical spectroscopy can be; to Dr. Torgom Yezekyan, with whom we spent many days adjusting and readjusting the TPL setup and discovering weaknesses in the Philidor defence in the breaks; to Assist. Prof. Joel Cox for his help in proof-reading the draft of this thesis and elucidating explanations about the nonlinear theory; to Dr. Martin Thomaschewski and Dr. Sergii Morozov for all the inspiring discussions during the coffee breaks and trips to the sea coast; to Jeanette Holst, who was always helpful with labware procurements and other bureaucratic issues. Moreover, I must also thank all collaborators and co-authors whom I have not explicitly mentioned above. Further, I thank Prof. Uriel Levy, Prof. Olivier J.F. Martin and Prof. Sebastian Hofferberth for taking time out their busy agendas to consider this thesis and serve on the assessment committee. Also, I acknowledge financial support from the VILLUM Foundation (VILLUM Investigator Program, grant No. 16498).

I should remember to thank my teachers and old friends Dr. Sergejs Bratarčuks and Dr. Konstantin Filonenko, who introduced to me the world of science and research. I am also thankful to my friends, who were always beside, even being physically thousands of kilometers away. I am very grateful to my family and parents, who always encouraged me to study and supported my long journey in Denmark.

Dedicated to K., as her love made this work and everything else possible.

List of publications

Journal publications included in this thesis

- A. **Interference in edge-scattering from monocrystalline gold flakes**
S. Boroviks, C. Wolff, J. Linnet, Y. Yang, F. Todisco, A.S. Roberts, S.I. Bozhevolnyi, B. Hecht, N.A. Mortensen
Optical Materials Express 8 (12), 3688-3697 (2018); DOI: 10.1364/OME.8.003688
- B. **Use of monocrystalline gold flakes for gap plasmon-based metasurfaces operating in the visible**
S. Boroviks, F. Todisco, N.A. Mortensen, S.I. Bozhevolnyi
Optical Materials Express 9 (11), 4209-4217 (2019); DOI: 10.1364/OME.9.004209
- C. **Anisotropic second-harmonic generation from monocrystalline gold flakes**
S. Boroviks, T. Yezekyan, Á.R. Echarri, F.J. García de Abajo, J.D. Cox, S.I. Bozhevolnyi, N.A. Mortensen, C. Wolff
Submitted to journal (2020); arXiv preprint: 2010.10982v1

Other journal publications

- D. **Multifunctional metamirror: polarization splitting and focusing**
S. Boroviks, R.A. Deshpande, N.A. Mortensen, S.I. Bozhevolnyi
ACS Photonics 5 (5), 1648-1653 (2018); DOI: 10.1021/acsphotonics.7b01091
- E. **Laser writing of bright colors on near-percolation plasmonic reflector arrays**
A.S. Roberts, S. M. Novikov, Y. Yang, Y. Chen, S. Boroviks, J. Beermann, N.A. Mortensen, S.I. Bozhevolnyi
ACS Nano 13 (1), 71-77 (2018); DOI: 10.1021/acs.nano.8b07541
- F. **Ultrabright single-photon emission from germanium-vacancy zero-phonon lines: deterministic emitter-waveguide interfacing at plasmonic hot spots**
H. Siampour, O. Wang, V.A. Zenin, S. Boroviks, P. Siyushev, Y. Yang, V.A. Davydov, L.F. Kulikova, V.N. Agafonov, A. Kubanek, N.A. Mortensen, F. Jelezko, S.I. Bozhevolnyi
Nanophotonics 9 (4), 953-962 (2020); DOI: 10.1515/nanoph-2020-0036
- G. **Fractal shaped periodic metal nanostructures atop dielectric-metal substrates for SERS applications**
S.M. Novikov, S. Boroviks, A.B. Evlyukhin, D.E. Tatarkin, A.V. Arsenin, V.S. Volkov, S.I. Bozhevolnyi
ACS Photonics 7 (7), 1708-1715 (2020); DOI: 10.1021/acsphotonics.0c00257
- H. **Efficient coupling of single organic molecules to channel plasmon polaritons supported by V-grooves in monocrystalline gold**
S. Kumar, T. Leißner, S. Boroviks, S.K.H. Andersen, J. Fiutowski, H.-G. Rubahn, N.A. Mortensen, S.I. Bozhevolnyi
ACS Photonics 7 (8), 2211-2218 (2020); DOI: 10.1021/acsphotonics.0c00738
- I. **Towards ultimate light confinement in plasmonic waveguides: does nonlocality matter?**
S. Boroviks, V.A. Zenin, Z.-H. Lin, M. Ziegler, S.I. Bozhevolnyi, J.-S. Huang, N.A. Mortensen
Manuscript in preparation

Conference contributions

J. Bifunctional metamirrors for simultaneous polarization splitting and focusing

S. Boroviks, R.A. Deshpande, N.A. Mortensen, S.I. Bozhevolnyi

SPIE Photonics Europe 2018, in Strasbourg, France

Poster presentation and publication in conference proceedings

K. Interference in edge-scattering from monocrystalline gold flakes

S. Boroviks, C. Wolff, J.Linnet, Y. Yang, F. Todisco, A.S. Roberts, S.I. Bozhevolnyi and N.A. Mortensen

XXV International Summer School Nicolás Cabrera – 2018: Manipulating Light and Matter at the Nanoscale, in Miraflores de la Sierra, Spain

Poster presentation

L. Enhancing efficiency of GSP-based metasurfaces at visible wavelengths using monocrystalline gold

S. Boroviks, N.A. Mortensen, S.I. Bozhevolnyi

NANOMETA 2019, in Seefeld, Tirol, Austria

Poster presentation

M. Improving performance of gap plasmon-based metasurfaces at visible wavelengths using monocrystalline gold substrate

S. Boroviks, N.A. Mortensen, S.I. Bozhevolnyi

SPP 9 (2019), in Copenhagen, Denmark

Poster presentation

Contents

Abstract	iii
Resumé	v
Acknowledgments	vii
List of publications	ix
1 Introduction	1
2 Light-matter interaction at the nanoscale	5
2.1 Fundamentals of Electromagnetism	5
2.2 Electromagnetic waves in linear media	6
2.3 Linear optical properties of gold	8
2.4 Surface plasmon polaritons	11
2.5 Nonlocal considerations	14
3 Monocrystalline gold flakes	19
3.1 Crystal structure and principles of colloidal synthesis	19
3.2 Synthesis of monocrystalline gold flakes	20
4 Towards nonlocal plasmonics in ultrathin MIM waveguides	23
4.1 Description of the experiment	23
4.2 Design of the coupling element	25
4.3 Fabrication of ultrathin MIM waveguides	26
4.4 s-SNOM characterization of GSPs	28
5 Nonlinear light-matter interaction	31
5.1 Nonlinear susceptibility and polarization	31
5.2 The wave equation in nonlinear media	32
5.3 Second-order processes	33
5.4 Third-order processes	34
5.5 Nonlinear optical properties of gold	34
6 Nonlinear microscopy of monocrystalline gold flakes	39
6.1 Experimental setup	39
6.2 SHG and TPL imaging of monocrystalline gold flakes	41
6.3 Ultrafast measurement of nonlinear dynamics	43
7 Summary and outlook	45
Bibliography	47
A Interference in edge-scattering from monocrystalline gold flakes	55
B Use of monocrystalline gold flakes for gap plasmon-based metasurfaces	66
C Anisotropic second-harmonic generation from monocrystalline gold flakes	76
Authorship agreements	82

Acronyms

AFM Atomic Force Microscope

ALD Atomic Layer Deposition

BF Bright-Field

DF Dark-Field

DOS Density of States

FCC Face Centered Cubic

FH First Harmonic

FIB Focused Ion Beam

FWHM Full Width at Half Maximum

GSP Gap Surface Plasmon

HCP Hexagonal-Close-Packed

IAC Interferometric Autocorrelation

LDOS Local Density of States

LRA Local Response Approximation

MIM Metal-Insulator-Metal

MPA Multi-Photon Absorption

MPL Multi-Photon Luminescence

NIR Near-Infrared

NL Nonlocal

PL Photoluminescence

s-SNOM Scattering-type Scanning Nearfield Optical Microscope

SEM Scanning Electron Microscope

SH Second Harmonic

SHG Second-Harmonic Generation

SPP Surface Plasmon Polariton

TE Transverse Electric

THG Third-Harmonic Generation

TM Transverse Magnetic

TPA Two-Photon Absorption

TPL Two-Photon Luminescence

1 Introduction

“There’s Plenty of Room at the Bottom”

Richard Feynman

Plasmonic nanostructures offer unique possibilities to concentrate light in regions of space that are much smaller than the conventional diffraction limit [1]. This is possible because light can couple to collective oscillations of free carriers in metals, giving rise to electromagnetic surface waves, known as surface plasmon polaritons (SPP). SPPs can be either propagating along the metal–dielectric interfaces or localized at the surfaces of metallic nanostructures, but in both cases they are evanescently confined at the surfaces and have effective wavelengths shorter than light of the same frequency in homogeneous dielectric media. Such optical confinement is associated with the local enhancement of the electromagnetic field, a feature desired in many areas of physics, chemistry, engineering and others, as it allows controllable amplification of linear and nonlinear optical processes at nanometer and even sub-nanometer length scales [2].

The significant progress in plasmonics over the last decades owes a great deal to the development of various nanofabrication methods that made possible creation of metallic nanostructures with unprecedented tolerances and reproducibility. Utilitarian design of these nanostructures facilitates engineering of their optical properties to achieve controllable localization of strong electromagnetic fields.

However, the confinement and enhancement of electromagnetic fields enabled by plasmons is not available for free, but rather comes at the expense of losses, caused by various inelastic scattering mechanisms of free carriers in metals. Intuitively, such losses are inevitable, as they prevent plasmons from oscillating faster than is allowed by the underlying sea of electrons, which actually make up the plasmons themselves. Losses place a serious constraint on the practical application of plasmonic components as subwavelength-sized optical interconnects, which seemed to be a promising prospect in the trend of optics miniaturization at the end of the 20th century. As outlined by Jacob B. Khurgin in his commentary article entitled “How to deal with the loss in plasmonics and metamaterials”, “... *even in the noblest of metals, losses in the optical range are still too high to make most, if not all, practical devices...*” [3]. Indeed, the SPP propagation lengths at the interfaces of traditional plasmonic materials – gold and silver – do not exceed hundreds of micrometers at optical wavelengths, and it is very hard to create plasmonic resonators with quality factor greater than 100. Therefore, a lot of research is striving to minimize the dissipative losses in plasmonic systems by improving the materials and their structuring methods.

Yet, even if the material scientists came up with the ideal, lossless metal [4], it would not solve all the problems associated with losses in plasmonics: confinement of electromagnetic fields has a fundamental limit which stems from quantum-mechanical phenomena in mesoscopic physics. Effects such as quantum pressure waves, Landau damping, quantum spill-out and tunneling lead to nonlocal response, which imposes a constraint on maximum achievable confinement and creates additional loss channels.

Hence, a natural question arises: after all, should we bother about the superficial improvement of plasmonic materials if there exists an ultimate restriction, which at present seems to be fundamentally overwhelming. In this thesis, I will try to persuade the reader that “the game is worth the candle”.

First of all, the limit will be never overcome if no one tries to push or at least reach it. Luckily, the author of this work and his supervisors are not the only people who share this opinion. Many research groups all over the world make collaborative efforts in exploring this limit and if not solving the problem, then at least learning how to deal with it [5].

Secondly, plasmonic nanostructures have already found applications and advanced the state of the art in many areas of technology and research. Even though some of the proof-of-concept publications are speculative and the proposed devices are at the moment not fully functional outside laboratories, the overall progress is evident.

Among the noticeable examples are single-molecule detection using surface-enhanced Raman spectroscopy (SERS) [6] and other biomedical applications, including cancer therapy [7] and even accurate detection of the notorious SARS-CoV-2 virus [8]. While the use of plasmonic interconnects in optical integrated circuits mostly remains impractical, ultra-compact and high-speed electro-optic modulators employing plasmonic elements have been demonstrated [9, 10]. Enhancement of the emission rate of single-photon sources in plasmonic cavities, which was considered only as a perspective possibility just a few years ago [11–14], recently became if not a routine, but certainly a widespread procedure [15, 16]. Last but not least, the quality of plasmonic metamaterials and metasurfaces is being steadily improved to be used in flat optical components [17–19] and in structural coloring [20, 21]. Of course, this list of examples is very far from being exhaustive, as new developments and discoveries are published at an exponentially growing frequency [22].

This PhD thesis presents a study of (quasi-) monocrystalline gold flakes, which emerged recently as a possible replacement for the conventional polycrystalline gold thin films. Gold flakes appear as flat and smooth crystals with high aspect ratios and hundreds of micrometers in lateral sizes. The well-defined crystal structure and nearly atomic flatness of these surfaces makes them an ideal material platform for the fabrication of plasmonic devices with the ultimate quality [23] and conducting the cleanest experiments on plasmonic phenomena [24–27]. In fact, crystalline gold possesses some properties that are markedly absent in its polycrystalline counterpart: for example, appendix C contains a study of anisotropy in the second-order nonlinear response from the monocrystalline gold flakes which is not observed from the evaporated gold.

However, a direct substitution of the evaporated or sputtered gold films is not always straightforward and beneficial. Appendix B presents such an example: employing monocrystalline gold as a substrate in the well-established gap surface plasmon (GSP) metasurfaces results only in a modest performance improvement and is complicated by fabrication constraints. Nevertheless, devices which do not require fabrication of stratified structures on top do benefit substantially from the crystalline quality of the gold flakes, as demonstrated in experiments on plasmonic enhancement of emission from single-photon sources in which I was proud to collaborate. [15, 16].

Finally, and perhaps a bit frivolously for a scientific text, I would like to mention that gold crystals are inexplicably aesthetically pleasing. I remember my genuine astonishment three years ago, when I saw for the first time a batch of gold flakes that I had synthesized in an optical dark-field microscope. This fascination led to curiosity that ultimately stimulated the work presented in appendix A.

Outline

The remainder of this thesis is structured in the following way: chapter 2 provides a summary of the theoretical foundations of nanoscale light-matter interaction in the linear regime. Chapter 3 describes the employed gold flake synthesis methods and discusses aspects of their crystal structure. Chapter 4 reports an experimental investigation of nonlocal effects in GSP waveguides which were designed and fabricated during my research

stay in the group of Dr. Jer-Shing Huang at the Leibniz Institute of Photonic Technology in Jena, Germany. Chapter 5 summarizes the basic concepts in nonlinear optics and nonlinear optical response of gold. Chapter 6 presents some unpublished results on nonlinear microscopy of monocrystalline gold flakes and two-photon absorption dynamics measurements. Finally, chapter 7 provides a summary of the thesis and a brief outlook on future perspectives.

Publications with the first-author contribution to the research work (papers A-C) which was carried out during the three years of this PhD project can be found in appendix.

2 Light-matter interaction at the nanoscale

In this chapter the theoretical foundations of electromagnetism, linear optics and plasmonics are reviewed, primarily with the aim to introduce the notation and conventions to be used in this thesis. With the exception of section 2.5, which deals with the nonlocal effects in plasmonics, this chapter was written based on several excellent textbooks [28–33] that provide thorough derivations and comprehensive explanations of the facts briefly stated in the following pages.

2.1 Fundamentals of Electromagnetism

Modern theoretical description of the light-metal interaction begins with the macroscopic *Maxwell equations*. In terms of external charge density $\bar{\rho}_e$ and external current density $\bar{\mathbf{j}}_e$, in differential form and in SI units they are formulated as

$$\nabla \cdot \bar{\mathbf{D}} = \bar{\rho}_e \quad (\text{Gauss's law}), \quad (2.1a)$$

$$\nabla \cdot \bar{\mathbf{B}} = 0 \quad (\text{Gauss's law for magnetism}), \quad (2.1b)$$

$$\nabla \times \bar{\mathbf{E}} = -\frac{\partial \bar{\mathbf{B}}}{\partial t} \quad (\text{Faraday's law}), \quad (2.1c)$$

$$\nabla \times \bar{\mathbf{H}} = \frac{\partial \bar{\mathbf{D}}}{\partial t} + \bar{\mathbf{j}}_e \quad (\text{Ampère's law}), \quad (2.1d)$$

where $\bar{\mathbf{E}}$ is the electric field, $\bar{\mathbf{H}}$ is the magnetic field, $\bar{\mathbf{D}}$ is the electric displacement, and $\bar{\mathbf{B}}$ is the magnetic induction. All of these quantities are real-valued, position \mathbf{r} and time t dependent vectors. The relations between electric field and displacement, as well as magnetic field and induction are given by the *constitutive relations*:

$$\bar{\mathbf{D}} = \varepsilon_0 \bar{\mathbf{E}} + \bar{\mathbf{P}}, \quad (2.2a)$$

$$\bar{\mathbf{H}} = \frac{\bar{\mathbf{B}}}{\mu_0} - \bar{\mathbf{M}}, \quad (2.2b)$$

where $\varepsilon_0 \approx 8.854 \cdot 10^{-12}$ F/m is the permittivity of free space, $\mu_0 \approx 4\pi \cdot 10^{-7}$ H/m is the permeability of free space, $\bar{\mathbf{P}}$ is the polarization of the medium and $\bar{\mathbf{M}}$ is the magnetization of the medium.

An implicit consequence of Maxwell's equations is the existence of *electromagnetic waves*. In non-magnetic media ($\bar{\mathbf{M}} = 0$), in the absence of external charges ($\rho_e = 0$) and currents ($\bar{\mathbf{j}}_e = 0$), the *inhomogeneous wave equation* can be derived by combining Faraday's and Ampère's laws:

$$\nabla \times \nabla \times \bar{\mathbf{E}} - \frac{1}{c^2} \frac{\partial^2 \bar{\mathbf{E}}}{\partial t^2} = \mu_0 \frac{\partial^2 \bar{\mathbf{P}}}{\partial t^2}, \quad (2.3)$$

with $c = 1/\sqrt{\varepsilon_0 \mu_0} \approx 2.998 \cdot 10^8$ m/s being the speed of light in vacuum.

One of the *ansatz* solutions of this partial differential equation represents transverse plane waves, which are conveniently written in a complex form:

$$\begin{aligned} \bar{\mathbf{E}}(\mathbf{r}, t) &= \text{Re} \left\{ \mathbf{E}(\mathbf{k}, \omega) e^{i(\mathbf{k}\mathbf{r} - \omega t)} \right\} = \text{Re} \left\{ \mathbf{E}_0 e^{i(\mathbf{k}\mathbf{r} - \omega t + \phi)} \right\} \\ &= \frac{1}{2} \left(\mathbf{E} e^{i(\mathbf{k}\mathbf{r} - \omega t)} + \mathbf{E}^* e^{-i(\mathbf{k}\mathbf{r} - \omega t)} \right), \end{aligned} \quad (2.4)$$

where $\tilde{\mathbf{E}}$ is a complex field, $\mathbf{E} = \mathbf{E}_0 e^{i\phi}$ is its complex amplitude (with magnitude \mathbf{E}_0 and phase ϕ), ω and \mathbf{k} are frequency and wavevector of the wave, respectively.

The magnitude of the wavevector, $k = |\mathbf{k}|$, is related to the *wavelength* $\lambda = 2\pi/k$. In free space (implying $\bar{\mathbf{P}} = 0$), the expression $k_0 = \omega/c = 2\pi/\lambda_0$ holds, and thus the free space wavelength λ_0 is a customary quantity in optics.

The frequency of the electromagnetic wave is directly proportional to the energy of its quantum – the *photon*: $E_{\text{ph}} = \hbar\omega$ (known as Planck–Einstein relation) where $\hbar \approx 6.582 \cdot 10^{-16}$ eVs is the reduced Planck's constant. It is also customary to describe light in terms of its photon energy.

Finally, the intensity of a monochromatic plane wave in free-space is proportional to the square of the magnitude of the electric field: $I = c\varepsilon_0|E|^2/2$.

2.2 Electromagnetic waves in linear media

The definition of a linear and nonmagnetic medium assumes that relations between $\bar{\mathbf{D}}$, $\bar{\mathbf{P}}$ and $\bar{\mathbf{E}}$, as well as between $\bar{\mathbf{H}}$ and $\bar{\mathbf{B}}$ are linear:

$$\bar{\mathbf{D}} = \varepsilon_0 \bar{\varepsilon} \bar{\mathbf{E}}, \quad (2.5a)$$

$$\bar{\mathbf{P}} = \varepsilon_0 \bar{\chi} \bar{\mathbf{E}}, \quad (2.5b)$$

$$\bar{\mathbf{H}} = \frac{1}{\mu_0} \bar{\mathbf{B}}, \quad (2.5c)$$

where the proportionality constants $\bar{\varepsilon}$ and $\bar{\chi}$ are called *relative electric permittivity* (also commonly referred to as *dielectric function* of the metal) and *relative electric susceptibility* respectively, being related as $\bar{\varepsilon} = 1 + \bar{\chi}$. In general, $\bar{\chi}$ and $\bar{\varepsilon}$ are tensors, however in the case of isotropic media they have only diagonal elements, all of which are equal, and thus can be described by scalar quantities.

However, these simplified constitutive relations do not describe temporal and spatial dispersion, which is clearly an important aspect for metals, as will be shown in the following sections. In order to take dispersion into account, the relationships may be generalized as

$$\bar{\mathbf{D}}(\mathbf{r}, t) = \varepsilon_0 \int_V \int_0^\infty \bar{\varepsilon}(\mathbf{r}', t') \bar{\mathbf{E}}(\mathbf{r} - \mathbf{r}', t - t') d^3r' dt', \quad (2.6a)$$

$$\bar{\mathbf{P}}(\mathbf{r}, t) = \varepsilon_0 \int_V \int_0^\infty \bar{\chi}(\mathbf{r}', t') \bar{\mathbf{E}}(\mathbf{r} - \mathbf{r}', t - t') d^3r' dt', \quad (2.6b)$$

where the integral in space is carried out over all space V . In this equation, $\bar{\varepsilon}$ and $\bar{\chi}$ satisfy the physical causality principle (i.e. displacement field and polarization at time t do not respond to an electric field applied in future time t') and allow nonlocal interaction (i.e. the electric field at point \mathbf{r} may also cause response at another point in space \mathbf{r}'). By virtue of Fourier transformation, the constitutive relationships eq. 2.6 are cast to the frequency (\mathbf{k}, ω) space:

$$\mathbf{D}(\mathbf{k}, \omega) = \varepsilon_0 \varepsilon(\mathbf{k}, \omega) \mathbf{E}(\mathbf{k}, \omega), \quad (2.7a)$$

$$\mathbf{P}(\mathbf{k}, \omega) = \varepsilon_0 \chi(\mathbf{k}, \omega) \mathbf{E}(\mathbf{k}, \omega), \quad (2.7b)$$

where ε and χ are *complex* relative permittivity and susceptibility: $\varepsilon = \varepsilon' + i\varepsilon''$ and $\chi = \chi' + i\chi''$.

For many linear problems in optics and plasmonics, the so-called local response approximation (LRA) is valid even at the nanoscale. It assumes a spatially non-dispersive medium,

i.e. the spatial dependence of the permittivity is represented by Dirac delta function: $\bar{\varepsilon}(\mathbf{r} - \mathbf{r}', t - t') = \delta(\mathbf{r} - \mathbf{r}')\bar{\varepsilon}(t - t')$ and thus the Fourier transformed ε is only dependent on the frequency ω . The classical Drude model for the optical response of metals, which is discussed in the next section, is a model hinging on LRA. The nonlocal considerations in plasmonics are discussed in section 2.5.

With these assumptions, as well as assumption of non-magnetic medium, *the homogeneous wave equation* can be derived:

$$\nabla^2 \bar{\mathbf{E}} + \frac{n^2}{c^2} \frac{\partial^2 \bar{\mathbf{E}}}{\partial t^2} = 0, \quad (2.8)$$

where $n = \sqrt{\varepsilon}$ is the refractive index of the medium, and solution is assumed to be of the form of the transverse plane wave (which are divergence-free fields, which allows to replace the $\nabla \times \nabla \times$ with the Laplacian operator). Inserting the ansatz solution (eq. 2.4) into the eq. 2.8 or realizing that Fourier transform yields $\partial/\partial t \rightarrow -i\omega$, the *Helmholtz equation* is obtained:

$$\nabla^2 \mathbf{E} = -\frac{\varepsilon}{c^2} \omega^2 \mathbf{E}. \quad (2.9)$$

It should be also noted that the \mathbf{D} and \mathbf{P} fields can be equally well described in terms of the internal current density \mathbf{j} (not to be confused with the external current density \mathbf{j}_e), which is the time derivative of polarization:

$$\mathbf{j} = \frac{\partial \mathbf{P}}{\partial t} = \sigma \mathbf{E}, \quad (2.10)$$

with the proportionality constant $\sigma = i\varepsilon_0\omega\chi$ being the complex conductivity of the medium.

2.2.1 Linear absorption and polarization of the medium

An instructive way to describe linear light-matter interaction is to consider it from the polarization perspective, which is especially useful for understanding linear absorption as a consequence of energy exchange between the optical fields and polarization of the medium.

Omitting spatial dependence, the induced polarization in the material can be written as

$$\bar{\mathbf{P}} = \text{Re} \left\{ \varepsilon_0 \chi \mathbf{E}_0 e^{i(-\omega t + \phi)} \right\} = \varepsilon_0 \mathbf{E}_0 \left(\chi' \cos(-\omega t + \phi) - \chi'' \sin(-\omega t + \phi) \right). \quad (2.11)$$

From this follows that χ yields a phase shift between the electric field and polarization depending on the magnitudes of the values of its real and imaginary parts. Then, the rate of work done by the electromagnetic field on the medium is given by

$$\bar{\mathbf{E}} \cdot \frac{\partial \bar{\mathbf{P}}}{\partial t} = \frac{\varepsilon_0 |\mathbf{E}_0|^2 \omega}{2} \left(\chi' \sin(2(\phi - \omega t)) + \chi'' \cos(2(\phi - \omega t)) + \chi'' \right), \quad (2.12)$$

The two periodic contributions average over time to a net zero exchange of energy, but the constant term remains, resulting in a nonzero time-average:

$$\left\langle \bar{\mathbf{E}} \cdot \frac{\partial \bar{\mathbf{P}}}{\partial t} \right\rangle = \frac{\varepsilon_0 |\mathbf{E}_0|^2 \omega}{2} \chi'', \quad (2.13)$$

which describes linear absorption or gain, depending on the sign of χ'' . Since $\chi = \varepsilon - 1$, in the linear regime, absorption can be equally well described by the imaginary part of the complex permittivity, however the description above is useful for further understanding of *nonlinear absorption* which is discussed in chapter 5.

2.3 Linear optical properties of gold

In a wide wavelength range, the linear optical response of noble metals, and in particular of gold, is well described with a so-called *plasma model*, also commonly referred to as the *Drude model*. This classical model depicts the metal as an electron gas of density n that is quasi-free to move in front of a background of heavy nuclei and core electrons, which, in turn, are assumed to be stationary, as schematically illustrated in fig. 2.1a. The damping, which is caused by various electron scattering mechanisms, is included in the model via a phenomenological constant $\gamma = 1/\tau$, with τ being the mean free time between the scattering events. With the assumption of a harmonic driving field (eq. 2.4), the equation of the free electron motion reads as

$$\frac{\partial^2 \hat{\mathbf{r}}}{\partial t^2} + \gamma \frac{\partial \hat{\mathbf{r}}}{\partial t} = -\frac{e}{m^*} \mathbf{E} e^{-i\omega t}, \quad (2.14)$$

where $\hat{\mathbf{r}}$ is displacement of the electrons, e is the elementary charge and m^* is the effective electron mass. The equation of motion has a solution of the form

$$\hat{\mathbf{r}} = \frac{e}{m^*(\omega^2 + i\gamma\omega)} \mathbf{E} e^{-i\omega t}, \quad (2.15)$$

which can be used to derive an expression for the relative permittivity. The displacement of every electron contributes to the macroscopic polarization $\mathbf{P} = ne\hat{\mathbf{r}}$, so invoking eq. 2.7 and taking into account residual polarization due to the ionic background $\mathbf{P}_\infty = \varepsilon_0(\varepsilon_\infty - 1)\mathbf{E}$ gives an expression for the dielectric function:

$$\varepsilon_D(\omega) = \varepsilon_\infty - \frac{\omega_p^2}{\omega^2 + i\gamma\omega}, \quad (2.16)$$

with $\omega_p = \sqrt{ne^2/\varepsilon_0 m^*}$ being the characteristic frequency of the electron motion, known as the *plasma frequency*.

Figure 2.1b shows a comparison between the Drude model and an experimentally obtained dielectric function of the monocrystalline gold by Olmon et al. [34] in the visible and near-infrared (NIR) wavelength range. This data set is claimed to be more accurate than the widely used data from Johnson and Christy [35] or Palik [36], which were acquired more than 30 years earlier. Besides, it also presents a systematic study of the optical properties of evaporated and template-stripped gold samples. However, the data shown in fig. 2.1b was claimed to be the most appropriate for monocrystalline gold flakes [26, 37]. The parameters of the Drude dielectric function in fig. 2.1b were obtained by fitting eq. 2.16 to the experimental data with the least square method, resulting in following values: $\varepsilon_\infty = 4.69$, $\hbar\omega_p = 8.33$ eV and $\hbar\gamma = 0.047$ eV.

The validity of the free electron model breaks down at short wavelengths and strong optical fields due to the occurrence of interband transitions, which require quantum mechanical treatment and are described within the band theory of solids (briefly discussed in section 2.3.2). As can be seen from fig. 2.1b, the Drude model indeed deviates from the experimental observations at wavelengths shorter than $\lambda_0 \approx 700$ nm. This discrepancy in the visible range can be reduced by adding a Lorentz oscillator term to the model of the dielectric function [38, 39], which mimics the interband transitions:

$$\varepsilon_{DL}(\omega) = \varepsilon_\infty - \frac{a\omega_L^2}{\omega^2 - \omega_L^2 - \gamma_L\omega} - \frac{\omega_p^2}{\omega^2 + i\gamma\omega}, \quad (2.17)$$

where ω_L is the resonance frequency of the oscillator, γ_L is the damping and a is the oscillator strength. As can be seen from fig. 2.1b, adding a Lorentzian term extends the

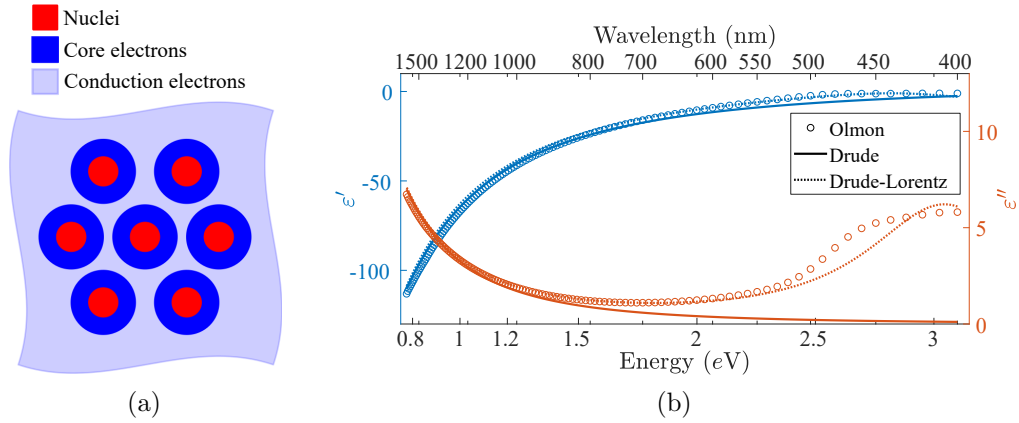


Figure 2.1: (a) Schematic illustration of the Drude metal model. (b) Real (ϵ' , blue plots, left vertical axis) and imaginary (ϵ'' , orange plots, right vertical axis) parts of the experimentally obtained complex dielectric function of monocrystalline gold in the visible and NIR wavelength range from ref. [34]. The solid and dotted lines are Drude and Drude–Lorentz model fits to the experimental data.

validity of the model significantly into the visible range, down to approximately 550 nm. The parameters of the Lorentz oscillator, also obtained by least squares fit, are $a = 0.17$, $\hbar\omega_L = 3.07$ eV and $\gamma_L = 0.8$ eV. In fact, adding multiple Lorentz oscillators to the model of the dielectric function allows to obtain a nearly perfect fit in the whole visible range [40], which may be useful in Finite-Difference Time-Domain (FDTD) simulations, however, it does not provide any new physical insight.

2.3.1 Sommerfeld theory of metals

Despite the success of the Drude model, it has limitations not only in the description of the optical properties of metals at high frequencies, but also in the description of its thermodynamic properties. Some of the discrepancies with experimental observations were resolved with the development of quantum theory and application of the *Pauli exclusion* principle to the free electron gas, implying that every electron occupies a single electron level.

The free electron gas in the Drude model is classical, and the distribution of electron velocity \mathbf{v} is described by the Maxwell–Boltzmann statistics: $f_{\text{MB}}(\mathbf{v}) = n(m^*/2\pi k_B T)^{3/2} e^{-mv^2/2k_B T}$, where $k_B \approx 1.381 \cdot 10^{-23}$ J/K is the Boltzmann constant and T is the absolute temperature. In the Sommerfeld free electron model, it is replaced with the Fermi–Dirac statistics:

$$f_{\text{FD}}(\mathbf{v}) = \frac{m^{*3}}{4\pi^3 \hbar^3} \frac{1}{e^{(m^*v^2/2 - k_B T_0)/k_B T} + 1}, \quad (2.18)$$

which implies (to some extent surprisingly) that in a Fermi gas, some electrons have a nonzero momentum even at zero temperature. As will be shown in the following, it has important consequences also for the optical response of metals. Within Sommerfeld’s model, the state of an electron, described by the wavefunction $\psi(\mathbf{r})$, satisfies the time-independent Schrödinger equation:

$$\hat{\mathcal{H}}\psi(\mathbf{r}) = \left(-\frac{\hbar^2}{2m^*} \nabla^2 + U(\mathbf{r}) \right) \psi(\mathbf{r}) = \mathcal{E}\psi(\mathbf{r}). \quad (2.19)$$

The free electron model assumes that the potential $U(\mathbf{r})$ is zero: all electron–electron and electron–nuclei interactions are neglected. Imposing periodic boundary conditions

$[\psi(r_i + R) = \psi(r_i)]$ for all r_i , the equation has a solution of the form

$$\psi_{\boldsymbol{\kappa}} = \frac{1}{\sqrt{R^3}} e^{i\boldsymbol{\kappa} \cdot \mathbf{r}}, \quad (2.20)$$

where $\boldsymbol{\kappa}$ is the electron's wavevector. This eigenstate has a $\boldsymbol{\kappa}$ -dependent energy eigenvalue:

$$\mathcal{E}(\boldsymbol{\kappa}) = \frac{\hbar^2 \boldsymbol{\kappa}^2}{2m^*}. \quad (2.21)$$

The state $\psi_{\boldsymbol{\kappa}}(\mathbf{r})$ is also an eigenstate of the momentum operator $\hat{\mathbf{p}} = \frac{\hbar}{i} \nabla$ with an eigenvalue $\mathbf{p} = \hbar \boldsymbol{\kappa}$. Furthermore, periodic boundary conditions impose the quantization condition: $\kappa_i = 2\pi n_i / R$, with n_i being an integer. This implies that electrons can only occupy discrete states which correspond to discrete values of energy. The state with the lowest energy is known as the *ground state*.

This treatment can be expanded to a system of N electrons (which are, though, still non-interacting) by successively adding electrons to unoccupied states starting from $\boldsymbol{\kappa} = 0$. In the case of large N , the occupied region in $\boldsymbol{\kappa}$ -space becomes indistinguishable from a sphere with radius κ_F , which corresponds to the wavevector of the state with the highest $\mathcal{E}_F = \hbar^2 \kappa_F^2 / 2m^*$, known as the *Fermi energy*. Furthermore, the electron corresponding to this state has momentum $p_F = \hbar \kappa_F$ (*the Fermi momentum*), velocity $v_F = p_F / m^*$ (*the Fermi velocity*), and wavelength $\lambda_F = 2\pi / \kappa_F$ (*the Fermi wavelength*). These quantities are ubiquitous in solid state physics and will be used in section 2.5 for the description of nonlocal effects in plasmonics. For gold, experimentally measured values these quantities are $\kappa_F \approx 12.1 \text{ nm}^{-1}$, $\mathcal{E}_F \approx 5.53 \text{ eV}$, $v_F \approx 1.4 \cdot 10^6 \text{ m/s}$ and $\lambda_F \approx 0.5 \text{ nm}$.

2.3.2 Electronic band theory

Even though the free electron model is relatively successful in describing the optical properties of gold in the NIR, it clearly has its limitations due to oversimplified approximations. In order to get deeper insight into the physical mechanisms of light-metal interaction, a more detailed description is required, which does not neglect electron-ion and electron-electron interactions. Since gold has atomic number 79 and $[\text{Xe}] 4f^{14} 5d^{10} 6s^1$ electron configuration, an exact quantum mechanical description of just a single gold atom is a complex many-body problem. An exact treatment of a macroscopic solid which consists of N atoms is obviously even more complicated and falls far beyond the scope of this thesis.

However, a brief intuitive understanding can be obtained by considering that electrons in a crystalline solid are subjected to a periodic potential $U(\mathbf{r}) = U(\mathbf{r} + \mathbf{R})$. Such a periodic potential leads to periodic solutions of the Schrödinger equation, which, according to Bloch's theorem, are of the form

$$\psi_{n\boldsymbol{\kappa}}(\mathbf{r}) \propto e^{i\boldsymbol{\kappa} \cdot \mathbf{r}} u_{n\boldsymbol{\kappa}}(\mathbf{r}). \quad (2.22)$$

Here, $u_{n\boldsymbol{\kappa}}(\mathbf{r})$ is a function with the same periodicity as $U(\mathbf{r})$ and n is the *band index*. It appears because for a given $\boldsymbol{\kappa}$ there are many independent solutions of eq. 2.19, which correspond to different energies, i.e. the eigenstates $\psi_{n\boldsymbol{\kappa}}(\mathbf{r})$ have a set of the corresponding energy eigenvalues $\mathcal{E}_n(\boldsymbol{\kappa})$. Due to the periodicity of the problem, the wavevector $\boldsymbol{\kappa}$ is confined to the *first Brillouin zone*, which is a uniquely defined primitive cell of the crystal in the reciprocal space (i.e. $\boldsymbol{\kappa}$ -space). A wavevector $\boldsymbol{\kappa}'$ which lies outside the first Brillouin zone corresponds to the physically identical state inside the first Brillouin zone as $\boldsymbol{\kappa}' = \boldsymbol{\kappa} + \mathbf{K}$ (with \mathbf{K} being a reciprocal lattice vector). This leads to a description of the allowed electron energy levels in a periodic crystal in terms of the *energy bands*, which constitute the *electronic band structure* of a solid.

Figure 2.2 shows the electronic band structure of gold, calculated using ab initio density-functional theory (DFT) [41], in the vicinity the Fermi level and across the important symmetry points in the first Brillouin zone. Gold has the first Brillouin zone in a shape of a truncated octahedron, as it is a face-centered cubic (FCC) crystal. The upper band, which is parabolic in a first approximation, corresponds to the conduction band. It is also referred to as the sp -band, as it arises due to the overlap of atomic $6s$ orbitals hybridize with $6p$ orbitals. The lower bands are known as valence bands or d -bands.

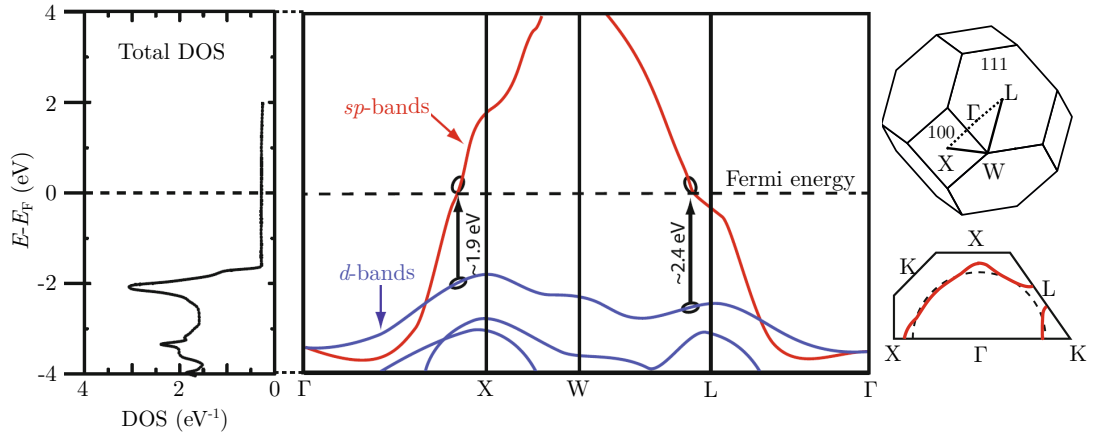


Figure 2.2: Density of states (left), electronic band structure (middle), First Brillouin zone (top right) and contour of the Fermi surface (right bottom) of gold calculated using density-functional-theory. Adapted with permission from refs. [41, 42].

Absorption of a photon leads to a transfer of its energy and momentum to an electron. Since photons do not carry a lot of momentum, their absorption corresponds to approximately vertical transitions of electrons in the energy band structure. In other words, conservation of momentum requires that the absorption of a photon happens along the light-line, which would appear nearly vertical if plotted next to the band structure in fig. 2.2. Therefore, transitions within the sp -band (called *intraband transitions*) are not possible in the vicinity of the Fermi energy due to large momentum mismatch between the allowed electronic states. However, intraband transition may occur when the momentum mismatch is compensated by a three-body scattering, for example when an electron simultaneously with the photon absorption scatters on a phonon or impurity.

In turn, the *interband transitions* (e.g. from d -band to an unoccupied state in sp -band) can happen due to absorption of a single photon. In fact, their occurrence in gold explains its characteristic color and behavior of the dielectric function. As shown in fig. 2.2, due to the anisotropy of the electronic potential, the Fermi surface of gold deviates from a free-electron-like spherical shape near the X and L symmetry points. It implies that the energy difference between the electrons in the d -band and unoccupied states in the sp -band is smallest at these points – approx. 1.9 eV near X and 2.4 eV near L . Since these energies are close to the photon energy of the visible light, the interband transitions are likely to happen these points. This explains why the imaginary part of gold's dielectric function in fig. 2.1b has a turning point at approx. 650 nm and a sharp increases at approx. 515 nm.

2.4 Surface plasmon polaritons

It is well known that metal-dielectric interfaces support guided electromagnetic surface waves that are evanescent in the surface-normal direction. These coupled oscillations of free electrons in the metal and electromagnetic waves are called *surface plasmon polaritons*

(SPP's). If the interface is assumed to be aligned in the xy plane at $z = 0$ (i.e. the permittivity of the medium changes only along z -axis), the solution of the wave equation (2.9) with the boundary conditions stemming from the Maxwell equations – continuity of the tangential component of \mathbf{E} and normal component of \mathbf{D} – results in the following solution, corresponding to the waves which are evanescent along z -axis and propagate along x -axis:

$$E_x(x, z > 0) = ik_{zd}E_0e^{-k_{zd}z}e^{ik_{spp}x}, \quad E_x(x, z < 0) = -ik_{zm}E_0e^{k_{zm}z}e^{ik_{spp}x}, \quad (2.23a)$$

$$E_z(x, z > 0) = -k_{spp}E_0e^{-k_{zd}z}e^{ik_{spp}x}, \quad E_z(x, z < 0) = -k_{spp}E_0e^{k_{zm}z}e^{ik_{spp}x}, \quad (2.23b)$$

$$H_y(x, z > 0) = \omega\varepsilon_0\varepsilon_dE_0e^{-k_{zd}z}e^{ik_{spp}x}, \quad H_y(x, z < 0) = \omega\varepsilon_0\varepsilon_dE_0e^{k_{zm}z}e^{ik_{spp}x}. \quad (2.23c)$$

A typical SPP field distribution, shown in fig. 2.3a, illustrates evanescent character in the surface-normal direction and the propagating wave behavior in the x -axis direction. It should be noted, that other components of the electric and magnetic fields (namely E_y , H_x and H_z) are equal to zero and thus SPP's are transverse magnetic (TM) modes. No surface modes exist for transverse electric (TE) polarization, since such fields do not satisfy the imposed boundary conditions. Furthermore, the boundary conditions result in the *dispersion relation* for the SPP propagation constant:

$$k_{spp} = k_0 \sqrt{\frac{\varepsilon_m \varepsilon_d}{\varepsilon_m + \varepsilon_d}}, \quad (2.24)$$

with ε_m being the dielectric function of metal and ε_d being that of dielectric medium. The surface-normal components of the wavevector in dielectric (k_{zd}) and metal (k_{zm}):

$$k_{zd} = \sqrt{k_{spp}^2 - k_0^2 \varepsilon_d}, \quad (2.25a)$$

$$k_{zm} = \sqrt{k_{spp}^2 - k_0^2 \varepsilon_m}. \quad (2.25b)$$

Several important characteristics of the SPP's, which are widely used in the literature as well as in the following sections of this thesis, are their wavelength $\lambda_{spp} = 2\pi/\text{Re}\{k_{spp}\}$, skin depth $\hat{z} = 1/|\text{Im}\{k_z\}|$, propagation length $L_{spp} = 1/2\text{Im}\{k_{spp}\}$ and effective mode index $n_{spp} = k_{spp}/k_0$.

It is instructive to first consider the SPP dispersion relation with the dielectric function of the metal described by an idealized Drude model (eq. 2.16), as shown in fig. 2.3b. In the absence of damping ($\gamma = 0$), the dispersion curves splits into two branches: at the frequencies above ω_p the metal becomes effectively transparent and thus the curve on the left from the light line corresponds to the dispersion of light in the metal, which is defined by coupling of electromagnetic waves to *bulk plasmons*. The second branch, on the right from the light line, corresponds to the dispersion of the surface plasmon polaritons. As the SPP dispersion never crosses the light line, a direct coupling of free-space light to these modes is not possible, but this obstacle can be circumvented with various phase-matching methods (e.g. grating or prism coupling).

At small wavenumbers the SPP curve asymptotically approaches the light line with the slope $c/\sqrt{\varepsilon_d}$, which is known as *the nonretarded limit*. On the other hand, in *the retarded limit*, the dispersion curve approaches the SPP resonance $\omega_s = \omega_p/\sqrt{1 + \varepsilon_d}$.

Furhtermore, fig. 2.3b demonstrates the influence of the damping parameter γ_L on the dispersion relation. In contrast to the lossless case, the SPP dispersion curve bends back to connect the two branches. This "back-bent" part of the curve corresponds to the

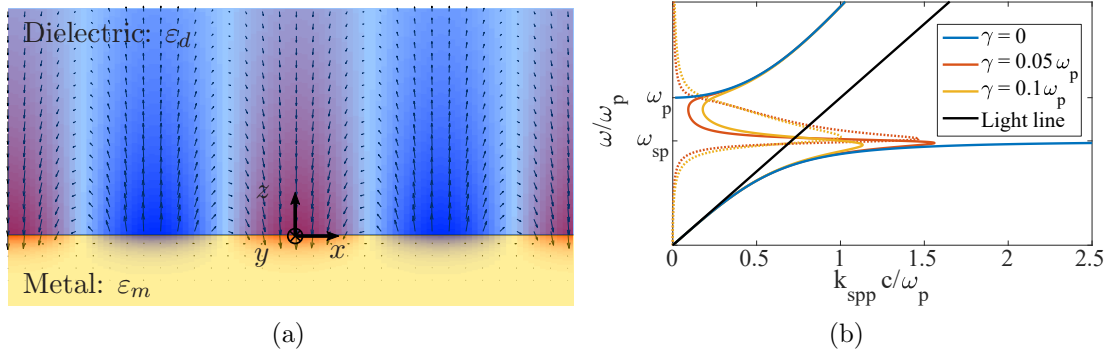


Figure 2.3: (a) Typical field distribution of a SPP at a gold-air interface: the color plot shows the amplitude of the \vec{H}_z field, the arrows indicate the \vec{E} -field vector. (b) Dispersion curves of SPPs at metal-air interface ($\epsilon_d = 1$ and ϵ_m is described by the Drude model with 3 different damping coefficient values). Solid lines correspond to the real part of the normalized propagation constant, dotted lines correspond to the imaginary part. The black solid line indicates the light line.

quasibound or *leaky* modes and limits the maximum achievable confinement of the mode in the perpendicular direction.

Next, it is interesting to investigate SPP dispersion curves obtained with the dielectric function of a real metal, rather than an idealized Drude model. Following the core interest of this thesis, fig. 2.4a shows the SPP dispersion curves at visible and NIR frequencies for monocrystalline gold-air ($\epsilon_d = 1$) and monocrystalline gold-glass ($\epsilon_d = 1.45^2$) interfaces (with ϵ_m described by interpolated experimental data from Olmon [34]). In the first case, the surface plasmon resonance occurs at the energy approx. 2.43 eV (corresponding to the free-space photon wavelength 510 nm), whereas in the latter case the resonance frequency is decreased to approx. 2.407 eV (approx. 515 nm). Both curves demonstrate strongly damped behavior, which imposes a limit on the SPP propagation length (plotted in fig. 2.4b). À propos: a comparison between SPP propagation length on the surface of monocrystalline and polycrystalline gold samples is provided in appendix B.

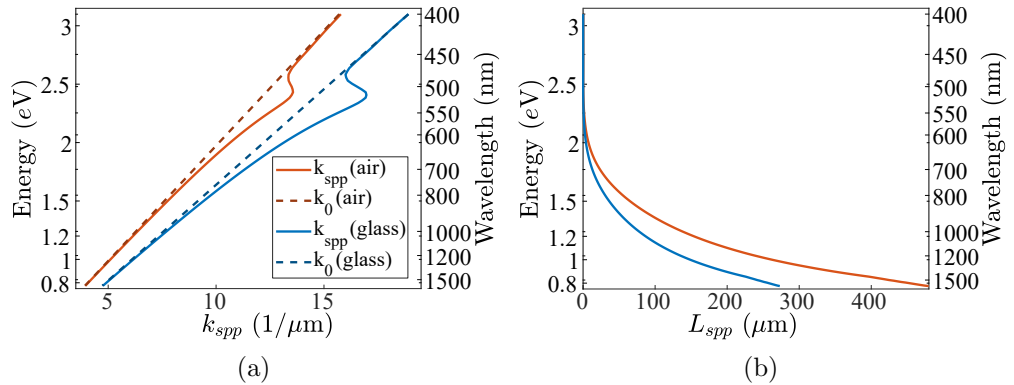


Figure 2.4: (a) Dispersion curves (solid) of the SPPs at gold-air and gold-glass interfaces and corresponding light lines (dashed) in the respective dielectric medium. (b) SPP propagation length at the corresponding interfaces.

2.4.1 Gap Surface Plasmons

In a system with two or more metal-dielectric interfaces that are separated by the distance on the order of skin depth \hat{z} , interaction of the individual SPPs gives rise to the coupled modes. In particular, a metal-insulator-metal (MIM) structure supports gap surface

plasmon (GSP) modes. The dispersion relation of the fundamental GSP mode is given implicitly by

$$\tanh\left(\frac{k_{zd}t_d}{2}\right) = -\frac{k_{zm}\varepsilon_d}{k_{zd}\varepsilon_m}, \quad (2.26)$$

where t_d is the thickness of the dielectric layer and the expressions for the k_{zm} and k_{zd} are the same as in eq. 2.25. This equation does not have a closed-form solution, however, for not too large wave numbers it can be approximated with $\tanh(\alpha) \approx \alpha$, which results in the following explicit expression for the GSP propagation constant: [43]

$$k_{\text{gsp}} \approx k_0 \sqrt{\varepsilon_d - \frac{2\varepsilon_d \sqrt{\varepsilon_d - \varepsilon_m}}{k_0 t_d \varepsilon_m}}. \quad (2.27)$$

Alternatively, eq. 2.26 can be solved numerically, for example using the Levenberg–Marquardt algorithm implemented in the `fsolve` function in various programming languages (e.g. in MATLAB, which is used for most of the calculations in this thesis).

The electromagnetic field of the GSP mode is concentrated in the dielectric layer and decays evanescently into the metal slabs. Explicit expressions for the field distribution in the dielectric gap are given by:

$$E_x(x, -t_d/2 < z < t_d/2) = ik_{zd}E_0 e^{ik_{\text{gsp}}z} \left(e^{-k_{zd}z} - e^{k_{zd}z} \right), \quad (2.28a)$$

$$E_y(x, -t_d/2 < z < t_d/2) = k_{\text{gsp}}E_0 e^{ik_{\text{gsp}}z} \left(e^{-k_{zd}z} + e^{k_{zd}z} \right), \quad (2.28b)$$

$$H_z(x, -t_d/2 < z < t_d/2) = \omega\varepsilon_0\varepsilon_d E_0 e^{ik_{\text{gsp}}z} \left(e^{-k_{zd}z} + e^{k_{zd}z} \right), \quad (2.28c)$$

whereas the fields in the metal slabs are described similarly to the usual SPP (eq. 2.23), where the only difference is that in the upper metal half-space fields have opposite sign and phase. A typical GSP field distribution is shown in fig. 2.5a.

The trade-off between mode confinement and propagation length, which is typical for all plasmonic waveguides becomes especially prominent for MIM structures. Figure 2.5 shows that much larger propagation constants are achievable with GSP as compared to a single interface SPP. Consequently, this results in strong localization of the electromagnetic field in the region of the sub-wavelength dielectric gap, albeit at the expense of decreased propagation length. Also, fig. 2.5 provides a comparison between the approximated (eq. 2.27) and numerically exact solutions of the GSP dispersion (eq. 2.26): as expected, the approximation works qualitatively well for smaller propagation constants and significantly deviates from the exact curves only for small gap thicknesses.

2.5 Nonlocal considerations

Even though the LRA is very successful in the description of experimental results in nanoplasmonics, the validity of this model is expected to break at the near-atomic length scale. At lengths comparable to the Fermi wavelength of electrons (approx. 0.52 nm in gold), screening phenomenon becomes a significant factor. It leads to charge smearing over Thomas-Fermi screening length and spill-out of free electrons beyond the classical metal boundary. In turn, this causes nonlocality in the electromagnetic response of the material, i.e. the spatial dependence of ε in eq. 2.6 cannot be described by the Dirac delta function.

Nevertheless, screening is not the only cause of nonlocal effects in plasmonics. Another mechanism which gives rise to spatial dispersion is known as *Landau damping*. It is associated with the absorption of energy by electrons which have longitudinal velocity

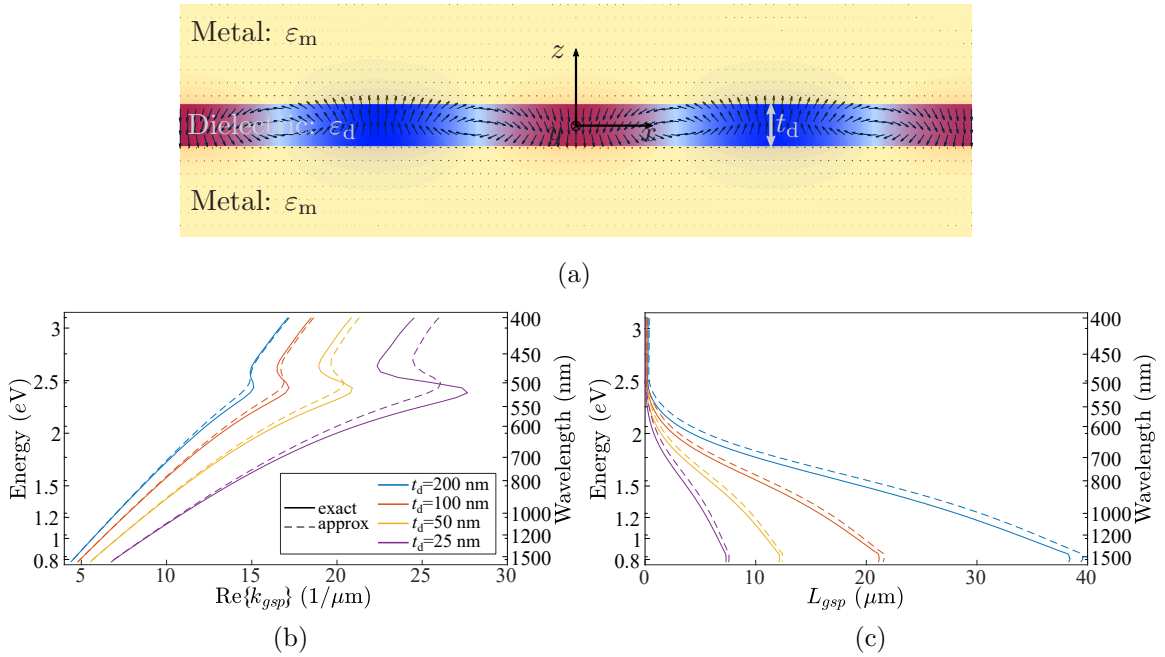


Figure 2.5: (a) Typical field distribution of a GSP at a gold-air-gold interface: the color plot shows the amplitude of \bar{H}_z and the arrows indicate the \bar{E} -field vector. (b) Dispersion curves of the GSPs at gold-air-gold interface for gap thicknesses t_d in the range 25–200 nm. Solid curves correspond to numerically exact solutions and dashed curves correspond to the approximate solutions (eq. 2.27). (c) Corresponding GSP propagation lengths.

component greater than the phase velocity of the electromagnetic surface wave. As discussed in the previous section, large propagation constants occur in plasmonic systems with small characteristic dimensions, e.g. t_d in the planar GSP waveguides, and thus nonlocal effects are expected to be an important aspect in such systems [44].

A rigorous theoretical treatment of plasmonic systems with *ab initio* methods, such as density-functional theory (DFT) [45], is computationally very heavy. Albeit some progress in this direction has been shown for a small plasmonic system [46], computational demand puts a constraint on the applicability of these methods in systems with larger dimensions, which consist of thousands of atoms. Therefore, over the last decades, significant efforts have been put into the development of semiclassical approaches, which are computationally less demanding, but capture nonlocal effects and retain physical insights. A few examples (among the vast sea of publications) of works reporting progress in this field are provided in refs. [47–52].

In this section the focus is on the *hydrodynamic model*, which was first proposed by Felix Bloch in 1933 [53]. A detailed description and derivations, as well as a discussion of physical implications and limitations can be found in several recent review papers [54–56].

2.5.1 Hydrodynamic model

Within the hydrodynamic model of plasmonics, the collective motion of the electrons is expressed in terms of the electron density $n(\mathbf{r}, t)$ and the hydrodynamic velocity $\mathbf{v}(\mathbf{r}, t)$. Under the influence of the electric and magnetic fields, the dynamics of the electron plasma

is described with the equations, which are known from fluid mechanics as *Euler equations*:

$$\frac{\partial \mathbf{v}}{\partial t} + \mathbf{v} \cdot \nabla \mathbf{v} - \gamma_L \mathbf{v} = -\frac{e}{m} (\mathbf{E} + \mathbf{v} \times \mathbf{B}) - \frac{\beta_F^2}{n} \nabla n, \quad (2.29a)$$

$$\frac{\partial n}{\partial t} = -\nabla \cdot n \mathbf{v}. \quad (2.29b)$$

The terms on the left-hand side of eq. 2.29a represent acceleration, convection and damping respectively, whereas the terms on the right-hand side correspond to the acceleration due to the Lorentz force and the pressure of the electron gas. The factor $\beta_F = v_F \sqrt{3/5}$ is the parameter arising from Thomas–Fermi theory of metals, which describes the finite compressibility of the electron gas. Equation 2.29b is the *continuity equation* which expresses the charge conservation.

Equation 2.29a can be linearized by assuming homogeneous and linear electron density (i.e. $n(\mathbf{r}, t) = n_0(\mathbf{r}) + n_1(\mathbf{r}, t)$) and dominant first order term in the Taylor expansion of the velocity field ($\mathbf{v}(\mathbf{r}, t) = 0 + \mathbf{v}_1(\mathbf{r}, t)$). In terms of the internal current densities ($\mathbf{j} = -en_0\mathbf{v}$), the linearized equation reads:

$$\beta_F^2 \nabla (\nabla \cdot \mathbf{j}) + \omega(\omega + i\gamma) \mathbf{j} = i\omega\omega_p^2 \varepsilon_0 \mathbf{E}. \quad (2.30)$$

This equation is then combined with Maxwell's equations (eq. 2.1) and after some algebra, it can be separated in transverse and longitudinal parts, which are compactly written as

$$(\nabla^2 + k_m^2) \nabla \times \mathbf{E} = 0, \quad (2.31a)$$

$$(\nabla^2 + k_{nl}^2) \nabla \cdot \mathbf{E} = 0, \quad (2.31b)$$

with $k_m = k_0 \sqrt{\varepsilon_m}$ being the usual wave number in metal and nonlocal wavenumber defined as

$$k_{nl} = \beta_F^{-1} \sqrt{\omega + i\gamma\omega - \omega_p^2/\varepsilon_\infty}. \quad (2.32)$$

Since the wavenumbers in the longitudinal and transverse parts of eq. 2.31 are different, the effective dielectric function can be described by a tensor. Components of this tensor, which are transverse and longitudinal relative to the electric field, are given by

$$\varepsilon_T(\omega) = \varepsilon_m = \varepsilon_\infty - \frac{\omega_p^2}{\omega(\omega + i\gamma)}, \quad (2.33a)$$

$$\varepsilon_L(k, \omega) = \varepsilon_\infty - \frac{\omega_p^2}{\omega(\omega + i\gamma) - \beta_F^2 k^2}. \quad (2.33b)$$

Thus, the nonlocal response manifests in the additional, longitudinal component of the metal permittivity that is absent in the local response approximation.

2.5.2 Application to the Gap Surface Plasmons

Alternatively, instead of including the nonlocal contribution in the dielectric function of the metal, it can be also captured as a correction to the dispersion relation of the plasmonic mode [57]. In the case of a GSP mode, the modified dispersion relation reads

$$\tanh\left(\frac{k_{zd} t_d}{2}\right) = -\frac{k_{zm} \varepsilon_d}{k_{zd} \varepsilon_m} (1 + \delta_{nl}), \quad (2.34)$$

where the nonlocal correction term δ_{nl} implicitly depends on both, frequency and wavevector:

$$\delta_{nl}(k_{\text{gsp}}, \omega) = \frac{k_{\text{gsp}}^2}{k_{nl} k_{zm}} \frac{\varepsilon_m - \varepsilon_\infty}{\varepsilon_\infty}. \quad (2.35)$$

Figure 2.6 shows dispersion curves in local (LRA, described by eq. 2.26) and nonlocal (NL model, eq. 2.34) approximations for a range of dielectric gap thicknesses. In these calculations, the values of ϵ_∞ , ω_p and γ are the same as as in section 2.4, and the dielectric permittivity is described by interpolated experimental values for aluminum oxide (Al_2O_3) thin film [58].

Á propos: choice of this materials is not accidental: efforts of an experimental implementation of such MIM waveguide is presented in chapter 4.

As can be seen, the two approximations differ appreciably in terms of the real part of propagation constant k_{gsp} only for very small dielectric gap thickness ($t_d \approx 1$ nm). In contrast, the corresponding curves for the plasmon propagation length in fig. 2.5c differ significantly even at larger gap thicknesses. This is not unexpected, as nonlocal corrections mostly affects the imaginary part of the propagation constant.

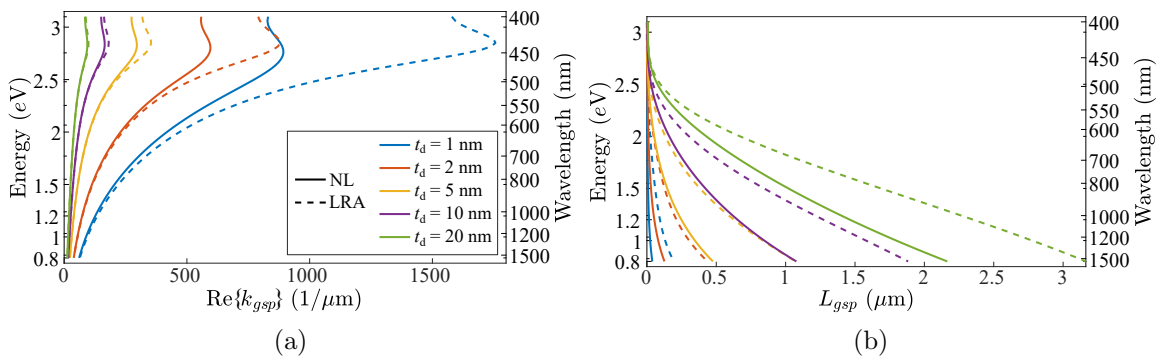


Figure 2.6: GSP dispersion curves calculated using LRA, eq. 2.26 (dashed lines) and NL model, eq. 2.34 (solid lines) for a range of dielectric gap thicknesses t_d . (a) Real part of the propagation constant; (b) plasmon propagation length.

At a first glance, one might get the impression that the nonlocal corrections to plasmon propagation length increases with increasing gap thickness t_d , but this is true only on the absolute scale. For example, at wavelength 1550 nm (corresponding to photon energy 0.79 eV) the difference between LRA and NL calculation for 10 nm gap is approximately 1 nm, whereas for 1 nm gap it is only around 0.1 nm. However in the relative comparison, in the first case the LRA and NL model are different by a factor approx. 1.5, whereas in the later they are different by nearly a factor 4.

The fact that nonlocal losses increase with decreasing gap thickness can be seen clearly in fig. 2.7, where the GSP dispersion is shown in a parametric plot as an implicit function of t_d . The plot shows the real and imaginary parts of the propagation constant calculated using the LRA and NL model for a free space wavelength 1550 nm and for a varying t_d (1 – 50 nm). The two curves nearly intersect at small values of k_{gsp} (which correspond to the larger values of t_d), however show qualitatively distinct behavior: the imaginary part of the propagation constant with the LRA increases approximately linearly with increasing $\text{Re}\{k_{\text{gsp}}\}$, whereas within the NL model it bends upwards in a parabolic shape, confirming that nonlocal losses become more pronounced with the smaller characteristic size of the plasmonic system.

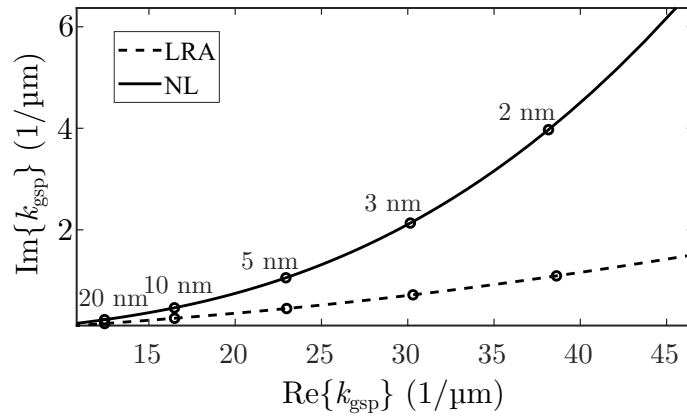


Figure 2.7: Parametric plot of the GSP dispersion for varying Al_2O_3 gap thickness (1–50 nm) at 1550 nm wavelength (corresponding to 0.79 eV) calculated using LRA (dashed line) and NL model (solid line). Points that correspond to $t_d = 2, 3, 5, 10$ and 20 nm are indicated with circles.

3 Monocrystalline gold flakes

As mentioned in chapter 1, progress in experimental plasmonics and nanophotonics over the last decades is largely due to a rapid development of nanofabrication techniques. Traditionally, nanoplasmonic devices have relied on metal thin film deposition techniques, e.g. Physical Vapor Deposition (PVD). Despite of the improvement of these techniques and the refinement of the usual protocols [59], evaporated or sputtered metal films remain polycrystalline and rough. Thus, their optical properties suffer from increased Ohmic losses caused by an additional electron scattering at crystal grain boundaries and surface irregularities. These intrinsic limitations are (at least partially) absent in chemically synthesized monocrystalline gold flakes, which recently have gained increased attention within the nanoplasmonics community [23, 25, 27, 60].

3.1 Crystal structure and principles of colloidal synthesis

In the modern history of science, Michael Faraday was one of the first to conduct experiments with light and colloidal solutions of gold nanoparticles, back in the year 1857. [61] Since then, physicists, chemists and material scientists have had tremendous progress in understanding the physical and optical properties of gold colloids and have developed chemical protocols to control their size and shape. [62–64]

One of the common precursors used for the synthesis of gold colloids is chloroauric acid HAuCl_4 . A wide variety of chemical reduction methods of this compound results in an even greater variety of shapes and sizes of synthesized nano- and microparticles. The main challenge posed by the nanoplasmonics community – synthesis of large scale crystalline gold thin films – has been addressed in many research articles (e.g. refs. [37, 65–72]), albeit with approximately similar results: gold crystals can grow in a flat, quasi-two-dimensional fashion, resulting in hexagonal or triangular flakes (or platelets), such as the ones shown in the optical micrographs in fig. 3.1.

Under normal conditions gold is a Face Centered Cubic (FCC) crystal, which has the lowest surface energy at $\{111\}$ -type facets [73]; atoms in $\{111\}$ planes are hexagonally-close-packed (HCP). Thus, an ideal crystal habit has the shape of an octahedron, bounded by $\{111\}$ facets. However, the real crystal habit is strongly dependent on the chemical environment of the process during the crystal seed formation stage. Intrinsic structure defects in the crystal

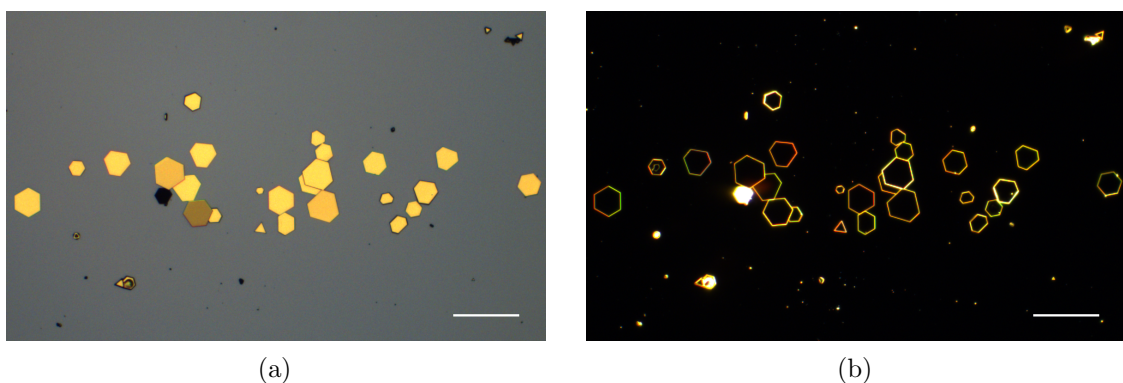


Figure 3.1: Optical micrographs of the monocrystalline gold flakes on Si substrate: (a) bright-field image; (b) dark-field image. Scale bars: 100 μm .

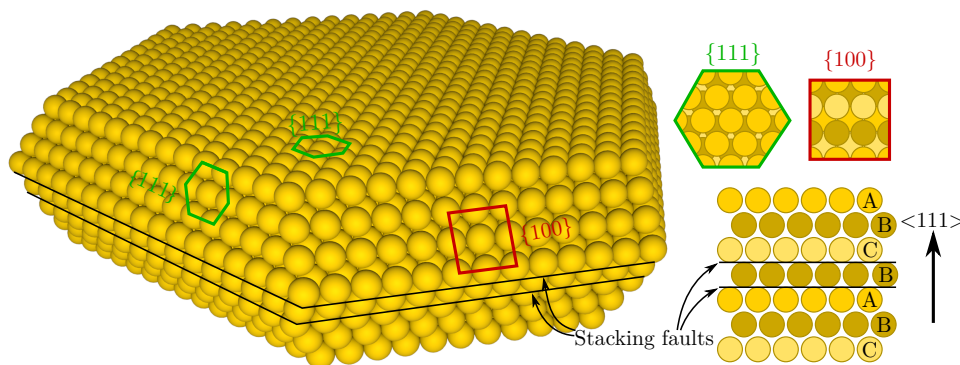


Figure 3.2: Crystal structure of a gold flake: 3 dimensional render of the crystal morphology, schematics of atom arrangements at $\{111\}$ - and $\{100\}$ -type surfaces and cross-sectional drawing illustrating the order of layers of stacking faults.

grain determine the preferred growth directions, which in turn define the macroscopic crystal morphology. Therefore, crystal shape and size can be engineered by selecting appropriate synthesis conditions, though not absolutely precisely, as even under nominally identical conditions the synthesis process remains to some degree random. The synthesis of gold flakes requires an environment that promotes anisotropic growth in lateral directions, due to the presence of multiple (at least two) stacking faults along the $\langle 111 \rangle$ -axis in the crystal seeds, as illustrated in fig. 3.2. These defects reverse the stacking order of HCP layers in the FCC lattice: the stacking order around a fault could be e.g. ...*ABCBABC*... instead of the ...*ABCBABC*... sequence in a perfect crystal. Thus, strictly speaking, the gold flakes are not exactly monocrystalline, but rather "quasi-monocrystalline", exhibiting perfect crystal lattice only in two dimensions.

Occurrence of stacking faults promotes fast growth in lateral directions, as new atoms tend to adjoin them rather than surfaces with lower energies. Hence, the resulting gold flakes often have morphology of truncated octahedrons that are squeezed along the $\langle 111 \rangle$ -axis and bounded by $\{111\}$ - and $\{100\}$ -type facets (apart from the thin region of stacking faults), since $\{100\}$ is the second lowest surface energy plane with square atom packing. It is worth to note, that a single stacking fault in the seed would be insufficient, as in this case the crystal would grow mostly along $\langle 100 \rangle$ and quickly cease the anisotropic growth. [72]

A study of the distinctive light scattering from the edges of the gold flakes, which is explained by the morphology of the flake, can be found in appendix A

3.2 Synthesis of monocrystalline gold flakes

Modified Brust-Schiffrin method

One of the gold flake synthesis recipes which was used in this PhD project (and for all works which can be found in the appendix) is the modified Brust–Schiffrin method [74], adopted from reference [75]. The main advantage of this recipe is that the flakes can be grown directly on substrate, without the need for subsequent transfer by drop-casting or similar method. It works with practically any inorganic substrate, e.g. glass or silicon wafer, ITO coated substrates, silicon nitride (SiN) membranes, and other. Apart from the precursor (HAuCl_4), the main ingredient in this method is tetraoctylammonium bromide (ToABr), which acts as a phase transfer catalyst, promoting transfer of AuCl_4^- ions from the aqueous to the organic phase for subsequent endothermic synthesis. The exact recipe is as follows:

1. Preparation of the precursor: dissolving HAuCl_4 in distilled water in concentration 6 mmol/L
2. Preparation of the organic environment: dissolving 1.4 g of ToABr in 5 mL of toluene
3. Mixture of the precursor and the organic solution: 10 min stirring at 5000 RPM
4. Separation of the organic and aqueous phases: solution is left to rest for 10 minutes
5. Preparation of the substrate: washing in acetone, IPA and distilled water, nitrogen blow dry, pre-baking at 200°C
6. Drop-casting few mL of the organic phase onto the substrate
7. Endothermic reaction and crystal growth: sample is kept on hot plate ($120^\circ\text{C} - 180^\circ\text{C}$) for 30 min – 24 h
8. Cleaning the sample: washing in toluene at 75°C , acetone, IPA and distilled water, nitrogen blow dry

The optimal growth temperature and time depend on the thermal conductivity of the substrate and desired size of the flakes. As a rule of thumb, lower temperatures and longer times result in laterally larger and thicker flakes (though with exceptions showing extremely large aspect ratios, approximately 1:2000), whereas high temperatures and short times result in laterally smaller and thinner flakes, often in large amounts. Figure 3.1 shows an example of the flakes synthesized on a SiN membrane at 200°C .

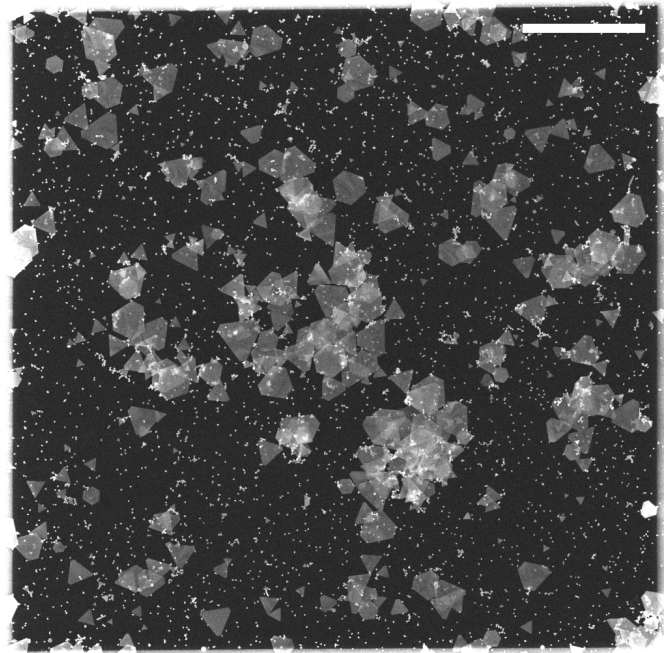


Figure 3.3: SEM image of the gold flakes synthesized on a SiN membrane. Scale bar: 20 μm . Courtesy of Jes Linnet.

Ethylene glycol-based method

An alternative method, which was used for the gold flake synthesis for the fabrication of ultrathin MIM waveguides (described in the next section), utilizes ethylene glycol (EG, $(\text{CH}_2\text{OH})_2$) as an organic environment for endothermic synthesis. The exact recipe is adopted from ref. [72]:

1. Preparation of precursor: dissolving HAuCl_4 in distilled water in concentration 6 mmol/L
2. 30 μL of HAuCl_4 aqueous solution are dissolved in 5 mL of EG in a beaker
3. Preparation of the substrate: washing in acetone, IPA and distilled water, nitrogen blow dry
4. Substrate is fully immersed in the growth solution and left on a hot plate at 100 °C for 24 h
5. Cleaning the sample: washing in acetone, IPA and distilled water, nitrogen blow dry

On average, this method results in laterally large gold flake samples with uniform thickness (less or approx. 100 nm), however some of the flakes tend to vary in thickness, in a terrace-like fashion. fig. 3.4 shows an example of such a sample: several flakes have "plateaus" of constant brightness in the transmitted-light optical micrographs. The apparent brightness of image increases towards the center of these flakes, which suggests that their thickness decreases. Nevertheless, as will be shown in chapter 6, such features, which are clearly disadvantageous for the fabrication of plasmonic devices, can be quite useful for the characterization of thickness-dependent nonlinear optical processes.

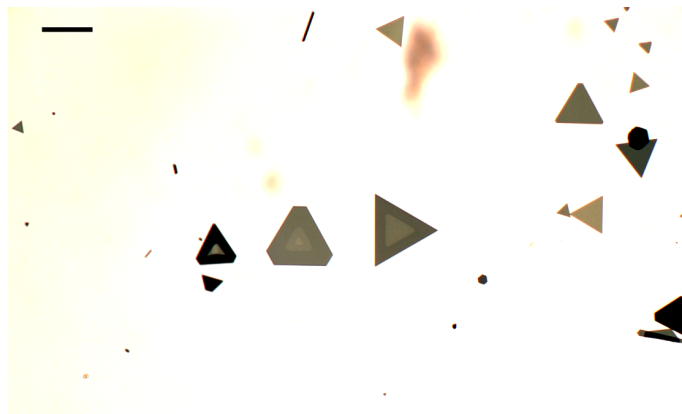


Figure 3.4: Transmitted-light optical micrograph showing gold flake samples with "terraces". Some samples show increase in the light transmittance towards the center, which indicates reduced gold flake thickness. Scale bar: 50 μm

4 Towards nonlocal plasmonics in ultrathin MIM waveguides

As outlined in chapter 2, nonlocal effects in plasmonics are expected to become more important as the characteristic size of the system is reduced to the order of a few nanometers. In the case of planar MIM waveguides, which support highly confined GSP modes, the nonlocal corrections are expected to mostly affect the imaginary part of the effective mode index. This results in a decreased GSP propagation length as compared with LRA calculations. From the experimental point of view, this fact imposes strict requirements on the quality of the waveguide samples: in order to measure the contribution of the nonlocal corrections, all complementary losses caused by metal imperfections (e.g. surface roughness and crystal grains in the bulk) need to be eliminated or at least mitigated to a minimum. Thus, monocrystalline gold flakes present a suitable material platform for an experimental study of nonlocal effects.

This chapter describes an experiment to quantitatively evaluate the importance of nonlocal effects in ultrathin MIM waveguides using a scattering-type scanning near-field optical microscopy (s-SNOM). The required ultrathin dielectric gaps are obtained using the atomic layer deposition (ALD) technique, which allows creating aluminium oxide (Al_2O_3) layers down to approx. 1 nm in thickness. The fabrication of the samples was performed in collaboration with the group of Dr. Jer-Shing Huang from the Leibniz Institute of Photonic Technology (Jena, Germany) and the near-field characterization performed by Dr. Volodymyr Zenin at the Centre for Nano Optics at SDU. At the time of the thesis submission, the optical part of the experiment remains in progress, and hence this chapter reports only preliminary results.

4.1 Description of the experiment

The s-SNOM allows to directly measure the evanescent near-fields (mainly their out-of-plane component [76, 77]) by detecting the light scattered by a sharp tip which scans the area above the surface of the sample. The resolution of s-SNOM imaging is not restricted by the conventional diffraction limit, as the detected signal comes from a small area where the tip interacts with the optical near-field. Thus, the s-SNOM resolution can be deeply subwavelength (down to approx. 10 nm) and is mostly limited by the sharpness of the tip. Besides, heterodyne demodulation of the detected signal permits to retrieve both, amplitude and phase of the evanescent waves. Therefore, the propagating surface waves' effective wavelengths and propagation lengths can be directly measured using s-SNOM imaging.

However, in MIM waveguides, the out-of-plane component of the evanescent field (which corresponds to E_z field component, according to the definitions in chapter 2) is strongly confined in the dielectric gap region (fig. 2.5a). Nevertheless, if one of the semi-infinite metal slabs is replaced with a thin metal layer, the evanescent wave's out-of-plane component will leak through the thin metal film. This change in the geometry will also affect the GSP mode since the new metal-dielectric interface adds new boundary conditions to the problem. Nevertheless, if the thickness of the metal layer is slightly greater than the skin depth of the original GSP, the effective mode index will remain approximately the same, while allowing a small portion of the E_z field to leak-out. This way, it becomes possible to characterize the propagating GSP mode using s-SNOM.

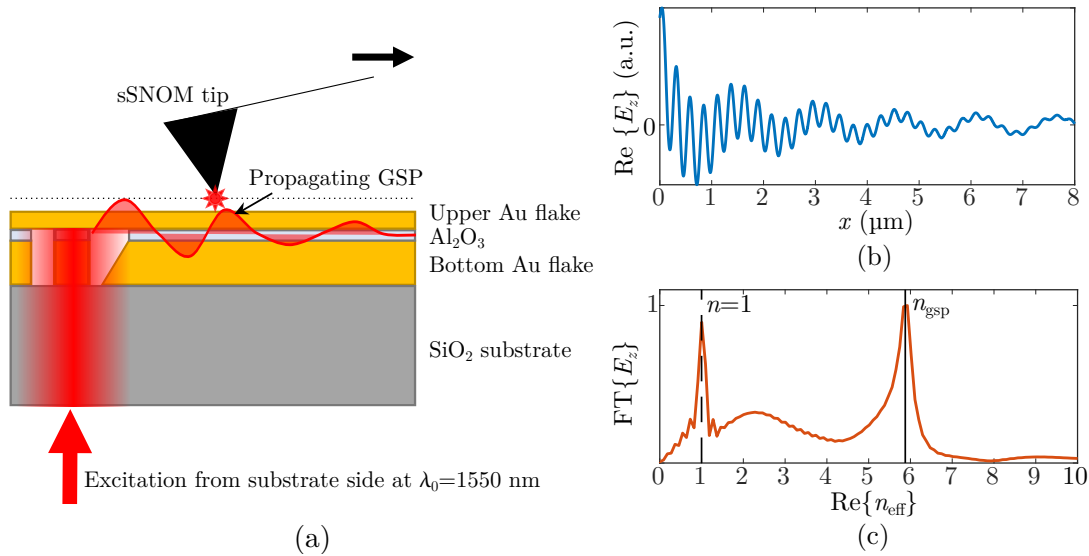


Figure 4.1: (a) Schematic illustration of the experiment: a laser beam ($\lambda_0 = 1550$ nm) is focused on a coupler from the substrate side to excite a propagating GSP mode. s-SNOM detects the evanescent fields (primarily their E_z component) scattered by a tip. Heterodyne demodulation allows to extract both, amplitude and phase of the detected signal. (b) Simulated $\text{Re}\{E_z\}$ field 20 nm above the upper gold layer of MIM waveguide with 5 nm dielectric gap thickness. (c) Fourier transform of the simulated E_z field. (d) Pseudo-color image of the field distribution in the cross-section of a tapered coupling element.

Figure 4.1a shows a schematic illustration of the proposed experiment. Since the s-SNOM at the Centre for Nanooptics at SDU is optimized for operation in the NIR wavelength range, the experiment is designed to operate at a free-space wavelength $\lambda_0 = 1550$ nm. The MIM is comprised of an ultrathin Al_2O_3 layer sandwiched between a thick bottom gold flake and a thin (approx. 30–40 nm) top flake. Focusing a laser beam onto the coupling element milled in the bottom flake excites a propagating GSP mode that is confined to the dielectric gap region; however, a portion of the leaky evanescent field can be scattered by the s-SNOM tip. Scanning the tip above the surface of the upper metal layer allows to record the evolution of the propagating GSP and extract the real and imaginary parts of the propagation constant.

In order to anticipate the outcome of the s-SNOM measurement, the proposed system was simulated using the Wave Optics package of Comsol Multiphysics. An established approach to model the s-SNOM near-field measurement is to evaluate the out-of-plane component of the electric field a few tens of nanometers above the surface, since the s-SNOM tip does not come into direct contact with the surface, but oscillates slightly above it [76, 77].

Figure 4.1b shows the evolution of the real part of the simulated E_z field along the GSP propagation direction 20 nm above the metal surface, excited by a free-space wavelength of 1550 nm (5 nm dielectric gap was considered in this particular simulation). The curve has an intricate oscillatory pattern consisting of several waves with different frequencies and propagation lengths. Taking the Fourier transform of the complex E_z field reveals its spectrum, which is shown in fig. 4.1 in terms of the real part of the effective index $n_{\text{eff}} = k_x/k_0$. The spectrum has two peaks: one at $n_{\text{eff}} \approx 1$, which corresponds to the SPP propagating along the upper metal interface and free-space light propagating at a grazing angle; and the other at $n_{\text{eff}} \approx 5.95$ which corresponds to the GSP mode. Furthermore, the GSP propagation length can be estimated by fitting an exponential function to the spatial evolution of the E_z amplitude. Hence, the simulation confirms that the proposed

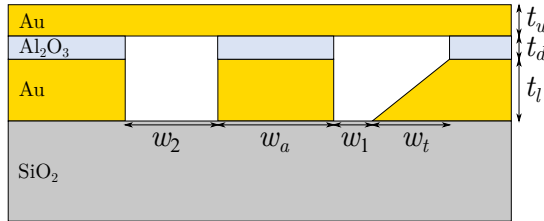
experiment scheme allows to estimate the sought real and imaginary parts of the GSP propagation constant.

4.2 Design of the coupling element

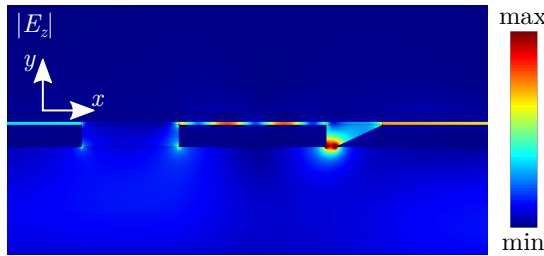
An important aspect of the proposed experiment is efficient coupling of the free-space laser light to the GSP mode, which is a nontrivial problem due to the large \mathbf{k} -vector mismatch, as discussed in chapter 2. Given that the GSP propagation length progressively decreases with decreasing dielectric gap thickness, the usual grating coupler scheme [29] becomes inefficient: due to strong losses the plasmon will not propagate beyond the grating itself and will be scattered at abrupt grating discontinuities. Furthermore, the fabrication tolerances place an additional constraint on the design of the coupler, since the experimentally realizable feature size cannot be arbitrarily small and sharp.

One possible solution for this problem is to design a coupler comprised of a single plasmonic resonator that has a GSP resonance at the desired frequency. If the MIM waveguide is placed in the vicinity of such plasmonic antenna, the near-field coupling of the two can excite the propagating mode. Furthermore, the coupling efficiency can be increased by creating a taper between the waveguide and the resonator, which is a common strategy for plasmon nanofocusing [78].

Figure 4.2a shows a sketch of such a coupling element with indicated geometrical parameters – thicknesses t_u , t_d and t_l of the layers, resonator width w_a , widths w_t and w_1 of the taper and the separation, respectively. Finally, the resonator is placed at a distance w_2 from the waveguide adjacent on the left-hand side. This distance can be chosen such that the separation works as a reflector, redirecting scattered field to the tapered side. This way, a unidirectional GSP excitation is achieved, which further enhances the coupling efficiency.



(a)



(b)

Figure 4.2: (a) Schematic cross-sectional drawing of the tapered coupling element with indicated geometric parameters. (b) Simulated scattered $|E_z|$ -field distribution in the optimized coupling element for $t_d = 5$ nm, illuminated with a Gaussian beam at $\lambda_0 = 1550$ nm

t_d	w_t	w_1	w_a	w_2	η_c
20	150	30	525	310	13.3%
10	120	30	475	410	12.2%
5	150	30	545	325	11.3%
4	145	30	505	395	11.9%
3	140	30	450	455	11.4%
2	145	30	505	415	10.7%
1	135	30	520	380	7.2%

Table 4.1: Optimized geometry parameters of the tapered coupling element for various dielectric gaps t_d , and for fixed $t_u = 30$ nm and $t_l = 70$ nm. All values, except for coupling efficiency η are given in units of nm.

The optimal coupler parameters for the range of considered gap thicknesses are listed in table 4.1. They were obtained by solving the maximization problem using the Nelder–Mead

method as implemented in the optimization module of COMSOL Multiphysics. All four optimization parameters (w_t , w_1 , w_a and w_2) were constrained to a minimal size of 30 nm in order to account for realistic fabrication tolerances. The objective function in this problem is the coupling efficiency, defined as the ratio of powers in excitation and receiving ports: $\eta = P_{\text{in}}/P_{\text{out}}$. The excitation port is configured to launch a weakly focused (NA = 0.15) Gaussian beam towards the resonator and the receiving port is configured to admit only the corresponding GSP mode. Although the COMSOL simulation does not account for nonlocal effects, for the optimization of the coupling geometry, their contribution can be neglected. Since they mainly affect the imaginary part of the GSP effective mode index (see fig. 2.6), the nonlocal corrections would mostly decrease the coupling efficiency value, but would not significantly change the optimal coupler parameters.

As can be seen from table 4.1, the coupling efficiency for small gap thicknesses t_d is on the order of 10%, which is not exceedingly high, but significantly greater than other tested coupler designs (not reported here). The simulations revealed that the coupling efficiency increases with decreasing resonator–taper separation distance: in principle, η can get even higher, if w_1 is allowed to be smaller than 30 nm. However, as mentioned above, the lower limit of the optimization constraint was chosen to be 30 nm to comply with the realistic fabrication tolerances.

Figure 4.2b shows the amplitude of the simulated E_z -field in the vicinity of the coupling element which is optimized for a gap thickness $t_d = 5$ nm. The field is concentrated in the dielectric gap and at the sharp feature of the taper. A standing wave pattern in the dielectric layer above the nanoantenna indicates that it is excited resonantly. Furthermore, the higher field amplitude in the dielectric region on the right-hand side from the nanoantenna shows that the coupling is indeed unidirectional.

4.3 Fabrication of ultrathin MIM waveguides

Having designed the optimal coupling element parameters, we can now turn to the experimental implementation of the ultrathin MIM waveguides. Figure 4.3 shows a schematic flowchart of the fabrication steps. The main fabrication challenge – formation of the coupling element pattern in the lower gold flake – was accomplished using focused ion beam (FIB) milling (performed in collaboration with Zhan-Hong Lin at Leibniz-IPHT in Jena). The FIB instrument utilizes a beam of accelerated gallium ions (Ga^+) to bombard the sample surface, which, at high beam current, allows local removal of the target material with a relatively high spatial resolution (down to few nanometers, depending on the sample material and other process parameters).

The exact fabrication step sequence (including some details that are omitted in fig. 4.3) is as follows:

1. Synthesis of the gold flakes on a glass substrate and identification of suitable samples
2. Coating the sample with a thin (approx. 5 nm) conductive carbon layer which is required for subsequent FIB milling.
3. FIB milling of the designed coupling element patterns
4. Removal of the auxiliary carbon layer using plasma etching
5. ALD of thin Al_2O_3 films (samples with thicknesses 2 – 20 nm were fabricated)
6. Transfer of the upper flake from another substrate on top of the prepared lower flakes

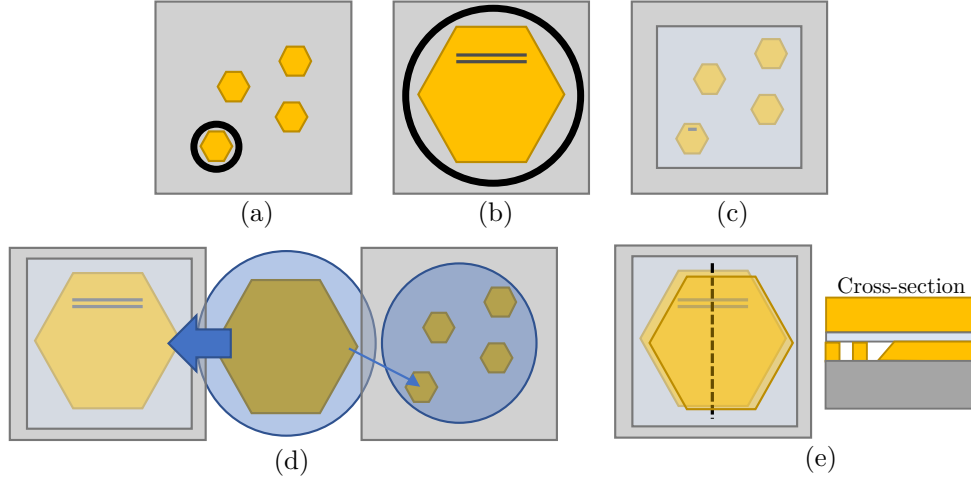


Figure 4.3: Ultrathin MIM waveguide fabrication recipe: (a) synthesis of monocrystalline gold flakes and identification of suitable samples; (b) milling of the coupling elements on the selected flake samples; (c) ALD deposition of Al_2O_3 thin film; (d) transfer of a flake from another substrate to create MIM geometry using a PDMS film as a carrier; (e) final structure and its cross-section.

7. Final plasma cleaning for removal of contamination inflicted during the transfer process

In total, 6 samples were fabricated, with the nominal Al_2O_3 layer thickness of 2, 3, 4, 5, 10 and 20 nm, each containing several coupling elements with the dimensions selected from table 4.1 for the respective thickness. During the trial fabrication we found out that the FIB patterning should be performed prior to ALD coating, as bombardment with energetic Ga^+ ions tends to spoil the quality of the Al_2O_3 film around the milling area (possibly caused by heating-induced damage of thermally unstable thin films). Although in this case the Al_2O_3 layer also covers the taper and slots in the coupling element, supplementary simulations confirmed that this deviation from the optimized design does not deteriorate the coupling efficiency by an appreciable amount. ALD was performed in collaboration with Mario Ziegler, also at the Leibniz-IPHT in Jena.

The transfer of the upper flake was performed using the polydimethylsiloxane (PDMS)-based technique described in ref. [79]. In this method, a PDMS film is used as a carrier substrate to carry thin gold flakes from one sample to another. Due to the temperature dependence of PDMS adhesion properties, gold flakes can be peeled off the cold substrate and stuck to another sample at an elevated temperature. Furthermore, the gold flakes can be precisely positioned on the target sample using an optical microscope equipped with a micromanipulator stage (in this project we used a commercial transfer system TSC1 by hq⁺ graphene).

As an example, fig. 4.4 shows micrographs of one of the fabricated samples with a 5 nm-thick Al_2O_3 layer. SEM images (panels c and d) taken prior to upper flake transfer, reveal the high quality of the FIB-milled coupling elements and smooth surface of the gold flake. Optical micrographs of the completed sample with the transferred upper flake are shown in panels e and f. The thickness of the upper flake, which was estimated using the atomic-force microscope (AFM) integrated in the s-SNOM setup, is approx. 40 nm. This value is slightly larger than the t_u used in the simulations, but still suitable for subsequent s-SNOM characterization. Unfortunately, the transfer of the upper upper flake did not come out ideally – defects and contamination inflicted during the transfer process are clearly visible in the DF optical image. Nevertheless, a sufficiently clean area can be found for a subsequent

s-SNOM characterization of the sample.

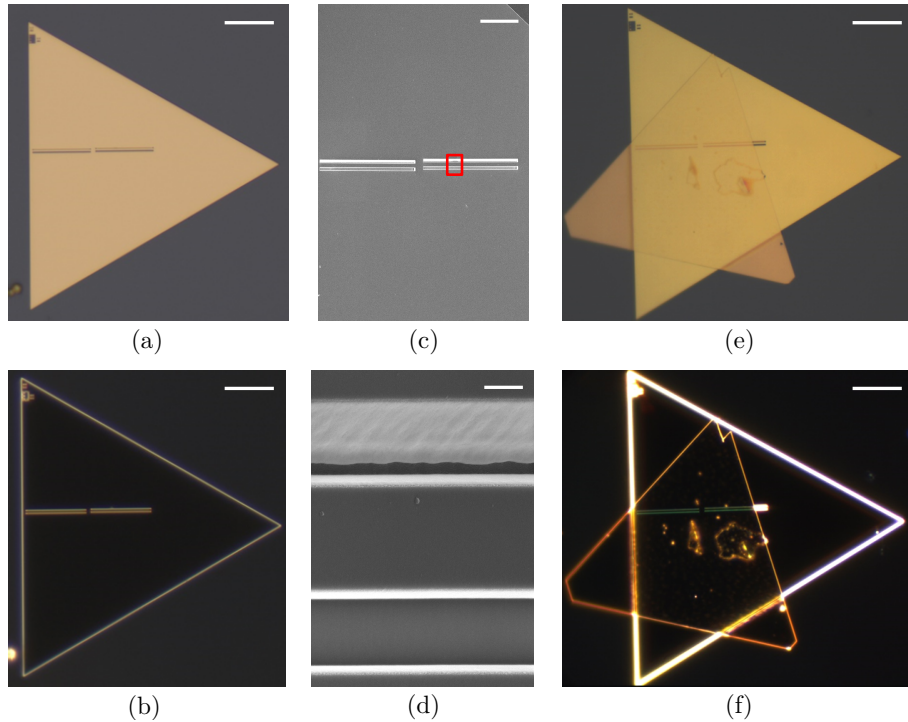


Figure 4.4: Fabricated ultrathin MIM waveguides: (a) BF and (b) DF optical micrographs of the gold flakes with FIB-milled tapered couplers prior to upper flake transfer (scale bars: 10 μm). (c) SEM image of the FIB-milled tapered couplers (scale bar: 5 μm) and (d) close-up of the area marked with the red rectangle (scale bar: 100 nm). (e) BF and (f) DF optical micrographs of the final structure (scale bars: 10 μm). SEM images are courtesy of Zhan-Hong Lin.

4.4 s-SNOM characterization of GSPs

Finally, we have reached the crucial part of this chapter - near-field characterization of the fabricated samples performed by my colleague Dr. Volodymyr Zenin, using the transmission module of a heavily customized setup based on commercial Neaspec neaSNOM microscope.

Figure 4.5 shows the near-field images of the MIM waveguide with a 5 nm dielectric gap. The bright region in panel a corresponds to the area right above the coupling element, where the amplitude of the detected signal is strongest. The oscillations in the amplitude are artifacts of the measurement caused by interference of the SPP waves travelling along the upper surface of the flake and free-space light at a grazing angle. Panels b and c show the phase and the real part of the measured near-field and are more informative. Clear fringes are visible in the right half of the image, which are reminiscent of the simulated E_z -field oscillations from fig. 4.1. Fourier transform along the GSP propagation direction (i.e. along the x -axis) reveals the spectrum of the measured signal. As expected, it shows two peaks: one at $n_{\text{eff}} \approx 1$ and another one at $n_{\text{eff}} = n_{\text{gsp}} \approx 5.2 \pm 0.2$. Further analysis allows to retrieve the imaginary part of the effective index: fitting a single exponential function to the spatial evolution of the extracted GSP mode amplitude gives a value of 0.19 ± 0.06 , which corresponds to approx. 4 μm propagation length.

The measured value of the real part of the effective mode index is slightly less than the simulated one (~ 5.95). This discrepancy can be attributed to an additional air gap between the Al_2O_3 layer and the upper gold flake caused by an imperfect adhesion after transfer step. The validity of this assumption is supported by the simulations shown in

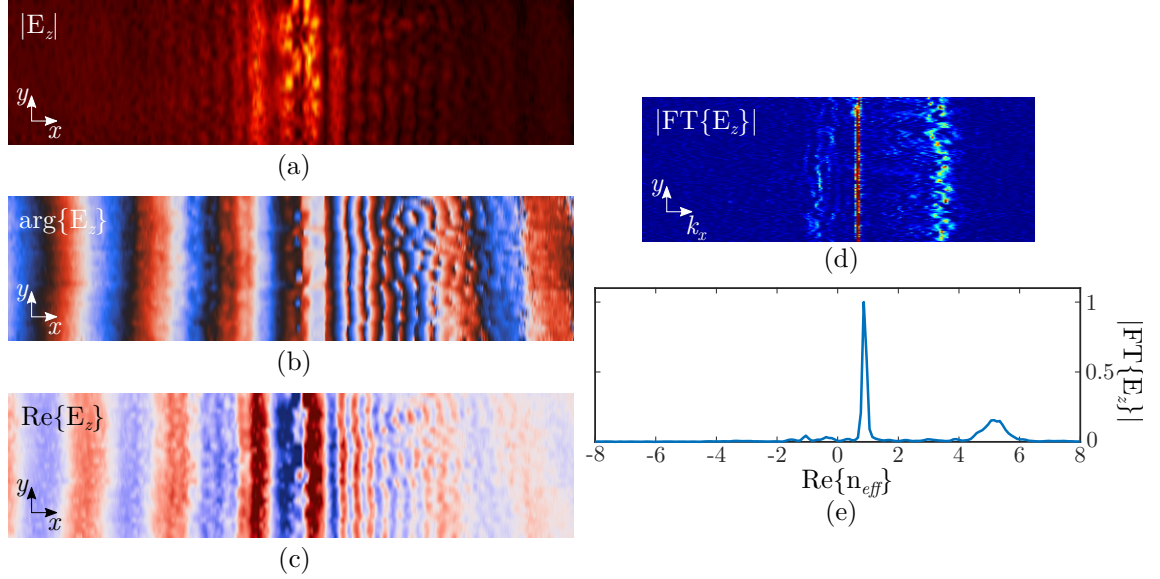


Figure 4.5: s-SNOM measurement of GSP propagation in a MIM waveguide with 5 nm dielectric gap: pseudo-color images of (a) the amplitude, (b) the phase, and (c) the real part of the detected signal, which mostly originates from the E_z component of the electric field above the surface of the sample. (d) pseudo-color image of the Fourier transform (only along the x axis) of the detected signal. (e) plot of the $\text{Re}\{n_{\text{eff}}\} = \text{Re}\{k_x/k_0\}$ spectrum obtained by integrating the image in panel (d) along vertical axis.

fig. 4.6. If a thin (1 or 2 nm) additional air gap is introduced, the dielectric constant of the gap layer can be described by a simple formula from the effective medium theory [33]:

$$\varepsilon_{\text{d,eff}} = \frac{t_{\text{d}}\varepsilon_{\text{Al}_2\text{O}_3}\varepsilon_{\text{air}}}{t_{\text{air}}\varepsilon_{\text{Al}_2\text{O}_3} + t_{\text{Al}_2\text{O}_3}\varepsilon_{\text{air}}}, \quad (4.1)$$

with t_{air} and $t_{\text{Al}_2\text{O}_3}$ being the thickness of air and aluminum layer respectively, and total gap is $t_{\text{d}} = t_{\text{Al}_2\text{O}_3} + t_{\text{air}}$. Calculations as in section 2.5 performed with this new setting for 0, 1 and 2 nm additional air gaps are shown in fig. 4.6a. Increasing the thickness of an additional air gap decreases the effective mode index, especially for small $t_{\text{Al}_2\text{O}_3}$. However, it does not change the shape of the dispersion curve. Setting $t_{\text{air}} = 0.5$ nm gives $n_{\text{gsp}} \approx 5.15$, which fits well with the experimentally obtained value.

Figure 4.6b shows a parametric plot of the effective GSP mode index calculated using LRA and NL models, with an additional 0.5 nm air gap for a range of $t_{\text{Al}_2\text{O}_3}$. Points corresponding to the nominal Al_2O_3 thicknesses in the fabricated samples are marked with the circles. This way of plotting the dispersion is quite instructive, as it clearly reveals the difference between the two models.

As a final remark, I should mention that after the remaining s-SNOM measurements will be completed, adding the experimental data points to fig. 4.6b will allow to judge which of the two models is more appropriate for the description GSPs in ultrathin MIM waveguides.

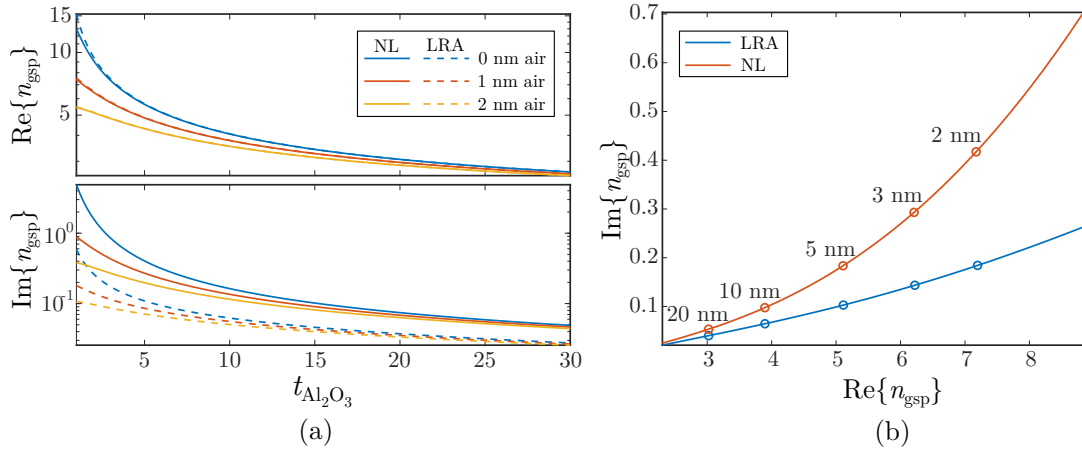


Figure 4.6: Simulations of the influence of an additional air gap on the GSP dispersion relation: (a) real and imaginary parts of the effective mode index calculated using LRA (dashed lines) and NL model (solid lines) for the nominal Al_2O_3 thickness without additional air gap (blue lines), and with 1 nm (orange lines) and 2 nm (yellow lines) additional air gaps. (b) parametric ($\text{Re}\{n_{\text{gsp}}\}$ vs $\text{Im}\{n_{\text{gsp}}\}$) plot of the GSP dispersion for varying gap thickness t_d (2 – 30 nm) with an additional 0.5 nm air gap; points that correspond to the nominal 2, 3, 5, 10 and 20 nm Al_2O_3 thickness values are indicated with circles.

5 Nonlinear light-matter interaction

This chapter provides a brief overview of the basic concepts in nonlinear optics and introduces relevant notation. The material presented here is primarily based on the excellent books on nonlinear optics by R. Boyd [80], Y.R. Shen [81] and P.E. Powers [30]. The nonlinear optical response of gold and relevance of these concepts to plasmonics are discussed in the last section.

5.1 Nonlinear susceptibility and polarization

In nonlinear optics, the material polarization defined in eq. 2.5 can be expanded in a power series of the electric field \bar{E} . Often, this definition is written omitting the spatial and frequency dependence as well as the vectorial nature of the fields:

$$\begin{aligned}\bar{P}(t) &= \bar{P}^{(1)}(t) + \bar{P}^{(2)}(t) + \bar{P}^{(3)}(t) + \dots \\ &= \varepsilon_0 \left(\bar{\chi}^{(1)} \bar{E}(t) + \bar{\chi}^{(2)} \bar{E}^2(t) + \bar{\chi}^{(3)} \bar{E}^3(t) + \dots \right),\end{aligned}\tag{5.1}$$

where $\bar{P}^{(n)}(t)$ and $\bar{\chi}^{(n)}$ are the n^{th} order nonlinear polarization and real-valued susceptibility, respectively. For many problems in nonlinear optics, higher orders in the expansion of the susceptibility can be neglected, as they decrease rapidly in magnitude: $|\bar{\chi}^{(1)}| \gg |\bar{\chi}^{(2)} \bar{E}| \gg |\bar{\chi}^{(3)} \bar{E}^2| \gg \dots$.

In fact, eq. 5.1 is valid only for one-dimensional problems and for *parametric* processes that assume an instantaneous response of the material. Generally, $\bar{\chi}^{(2)}$ is a third rank tensor, which has 27 elements, and $\bar{\chi}^{(3)}$ is a fourth rank tensor with 81 elements. This makes the complete mathematical treatment of the nonlinear polarization quite cumbersome, as will be shown in the following.

Nevertheless, the problem can be significantly simplified by exploiting the symmetry properties of the medium in question. In particular, $\chi^{(3)}$ (as well as other odd orders of nonlinear susceptibility) is present in all media, but the number of non-zero tensor elements depends on the crystal symmetry. For example, FCC crystals (such as gold), have 21 nonzero elements, only 4 of which are independent of each other.

In contrast, $\bar{\chi}^{(2)}$ vanishes in centrosymmetric media within the electric dipole approximation. Second-order interactions require an asymmetric potential function in the equation of the electron motion, which is clearly not the case in media with inversion symmetry. In-depth discussion and comparison with the classical oscillator model can be found in section 1.4 of reference [80]. This condition automatically eliminates a lot of common optical materials (e.g. glass, silicone, gold, etc.) from the discussion of bulk second-order nonlinearities. An example of a non-centrosymmetric material is a beta-barium-borate (BBO) crystal, which is widely used in optical laboratories due to its strong nonlinearity, belongs to the $3m$ crystal class and possesses C_{3v} symmetry. Consequently, it is fully described by 11 non-zero $\bar{\chi}^{(2)}$ tensor elements, only 5 of which are independent of each other.

However, second-order nonlinearities can be observed at the interfaces of centrosymmetric crystals, where the inversion symmetry is broken. Moreover, within the electric quadrupole approximation, second-order effects are allowed even in bulk centrosymmetric crystals. Though, in the case of gold, their contribution was shown to be small compared to the dipolar surface-like response [82, 83] (see section 5.5 and appendix C for the relevant discussion).

In order to take into account dispersion and vectorial fields, eq. 5.1 can be rewritten in a more general form (though still with an assumption of local response):

$$\begin{aligned} \bar{\mathbf{P}}(\mathbf{r}, t) = & \int_0^\infty \bar{\chi}^{(1)}(t') \cdot \bar{\mathbf{E}}(\mathbf{r}, t - t') dt' \\ & + \iint_0^\infty \bar{\chi}^{(2)}(t', t'') : \bar{\mathbf{E}}(\mathbf{r}, t - t') \bar{\mathbf{E}}(\mathbf{r}, t - t'') dt' dt'' \\ & + \iiint_0^\infty \bar{\chi}^{(3)}(t', t'', t''') : \bar{\mathbf{E}}(\mathbf{r}, t - t') \bar{\mathbf{E}}(\mathbf{r}, t - t'') \bar{\mathbf{E}}(\mathbf{r}, t - t''') dt' dt'' dt''', \end{aligned} \quad (5.2)$$

where $:$ and $\dot{}$ denote double and triple dot products respectively. Provided that the electric field can be represented as a sum of harmonic plane waves,

$$\bar{\mathbf{E}}(\mathbf{r}, t) = \text{Re} \left\{ \sum_n \tilde{\mathbf{E}}_n(\mathbf{r}, \omega_n) \right\} = \text{Re} \left\{ \sum_n \mathbf{E}(\omega_n) e^{i(\mathbf{k}_n \cdot \mathbf{r} - \omega_n t)} \right\}, \quad (5.3)$$

then by virtue of Fourier transform, eq. 5.2 can be cast into the frequency space, where it can be represented with a less cumbersome appearance:

$$\mathbf{P}(\omega) = \mathbf{P}^{(1)}(\omega) + \mathbf{P}^{(2)}(\omega) + \mathbf{P}^{(3)}(\omega) \quad (5.4)$$

$$= \chi^{(1)}(\omega) \cdot \mathbf{E}(\omega) + \chi^{(2)}(\omega = \omega_m + \omega_n) : \mathbf{E}(\omega_m) \mathbf{E}(\omega_n) \quad (5.5)$$

$$+ \chi^{(3)}(\omega = \omega_m + \omega_n + \omega_o) : \mathbf{E}(\omega_m) \mathbf{E}(\omega_n) \mathbf{E}(\omega_o). \quad (5.6)$$

In index notation, the second-order polarization is written as

$$P_i^{(2)}(\omega_m + \omega_n) = \varepsilon_0 \sum_{jk} \sum_{(mn)} \chi_{ijk}^{(2)}(\omega_m + \omega_n, \omega_m, \omega_n) E_j(\omega_m) E_k(\omega_n), \quad (5.7)$$

and the third-order polarization is

$$\begin{aligned} P_i^{(3)}(\omega_m + \omega_n + \omega_o) \\ = \varepsilon_0 \sum_{jkl} \sum_{(mno)} \chi_{ijkl}^{(3)}(\omega_m + \omega_n + \omega_o, \omega_m, \omega_n, \omega_o) E_j(\omega_o) E_k(\omega_n) E_l(\omega_m), \end{aligned} \quad (5.8)$$

where the indices i, j, k, l run through the Cartesian coordinates x, y, z , whereas the notation (mno) indicates that summation runs through varying permutations of frequencies $\omega_m, \omega_n, \omega_o$, while maintaining a fixed sum. Following the notation from chapter 2, the frequency dependent complex nonlinear susceptibilities may be written as $\chi^{(2)} = \chi'^{(2)} + i\chi''^{(2)}$ and $\chi^{(3)} = \chi'^{(3)} + i\chi''^{(3)}$.

In most practical problems, it is convenient to treat different orders of the nonlinear polarization separately, as they represent physically distinct processes and require different types of nonlinear materials. Special cases of these nonlinearities, which are relevant to the experimental part of this thesis, are discussed in sections 5.3 and 5.4

5.2 The wave equation in nonlinear media

The physical implications of the nonlinear material susceptibility become clear when the inhomogeneous wave equation is considered with the new definition of the polarization term. In nonlinear optics, it is customary to write eq. 2.3 in a slightly different form,

splitting the polarization into linear and nonlinear parts: $\bar{\mathbf{P}} = \bar{\mathbf{P}}^L + \bar{\mathbf{P}}^{\text{NL}}$, so that the constitutive relation (eq. 2.2) becomes:

$$\bar{\mathbf{D}} = \varepsilon_0 \bar{\mathbf{E}} + \bar{\mathbf{P}} = \varepsilon_0 \bar{\mathbf{E}} + \bar{\mathbf{P}}^L + \bar{\mathbf{P}}^{\text{NL}} = \varepsilon_0 \bar{\varepsilon} \bar{\mathbf{E}} + \bar{\mathbf{P}}^{\text{NL}}. \quad (5.9)$$

With these definitions, the inhomogeneous wave equation in nonlinear media is conveniently written as

$$\nabla \times \nabla \times \bar{\mathbf{E}} - \frac{\bar{\varepsilon}}{c^2} \frac{\partial^2 \bar{\mathbf{E}}}{\partial t^2} = \mu_0 \frac{\partial^2 \bar{\mathbf{P}}^{\text{NL}}}{\partial t^2}. \quad (5.10)$$

With a plane wave ansatz (see section 2.2) the first term can be written in the frequency domain as the inhomogeneous Helmholtz equation with a nonlinear polarization source term:

$$\nabla^2 \mathbf{E}_n(\mathbf{r}, \omega_n) + \frac{\omega_n^2}{c^2} \varepsilon(\omega_n) \mathbf{E}_n(\mathbf{r}, \omega_n) = -\frac{\omega_n^2}{\varepsilon_0 c^2} \mathbf{P}_n^{\text{NL}}(\mathbf{r}, \omega_n). \quad (5.11)$$

Generally, this equation is not easy to solve, hence, some approximations and assumptions are required, the most common being the slowly varying envelope approximation (SVEA). Furthermore, eq. 5.11 has to be satisfied at all frequencies which take part in the nonlinear process, including the frequencies that are not present in the excitation field, but produced by the induced nonlinear polarization.

5.3 Second-order processes

In the context of the experimental part of this thesis, it is interesting to consider a simple one-dimensional example, where the electric field is described by a monochromatic plane wave with the *fundamental frequency* $\omega_m = \omega_n = \omega$:

$$\bar{\mathbf{E}}(t) = \frac{1}{2} (E e^{-i\omega t} + E^* e^{i\omega t}). \quad (5.12)$$

Then, the second-order nonlinear polarization is

$$\bar{\mathbf{P}}^{(2)} = \frac{\varepsilon_0}{2} \left(\chi^{(2)} 2EE^* + \chi^{(2)} E^2 e^{-i2\omega t} + \chi^{(2)} E^{*2} e^{i2\omega t} \right), \quad (5.13)$$

where the frequency dependence and tensorial nature of $\chi^{(2)}$ are omitted for the sake of brevity. The first term is constant (i.e. at zero frequency), whereas the second and third terms oscillate at twice the frequency ω . Since the induced polarization is a source term in eq. 5.10, it leads to the generation of electromagnetic waves at 2ω , and so the associated process is known as *second-harmonic generation* (SHG). The intensity of the second harmonic (SH) radiation, $I_{2\omega}$, is proportional to the square of the intensity I_ω of the field at the fundamental frequency. The constant term does not lead to the generation of electromagnetic radiation, but creates a static electric field across the nonlinear medium through a process known as *optical rectification*.

In a (simplified) quantum-mechanical picture of the SHG process, two photons with energy $\hbar\omega$ are simultaneously absorbed and a new photon with energy $2\hbar\omega$ is created instantly. Thereby SHG is a coherent process. Furthermore, since these transitions are mediated by virtual states, SHG is categorized as a parametric process (i.e. it does not involve transitions to the real quantum-mechanical states of the matter).

The experimental observation of SHG was first reported in 1961 by Franken et al. [84], after the invention of the lasers which could provide sufficiently high intensities of coherent light. Later, SHG at the interfaces of centrosymmetric media was observed experimentally in transmission mode from a calcite crystal in 1962 by Terhune et al. [85] and in reflection mode from a metallic surface in 1965 by Brown et al. [86].

5.4 Third-order processes

A similar procedure as for the second-order nonlinear polarization in eq. 5.13 can be applied to the third-order nonlinear polarization term:

$$\bar{P}^{(3)} = \frac{\epsilon_0}{2} \left(\chi^{(3)} E^3 e^{-i3\omega t} + \chi^{(3)} E^{*3} e^{i3\omega t} + 3\chi^{(3)} |E|^2 E e^{-i\omega t} + 3\chi^{(3)} |E|^2 E^* e^{i\omega t} \right). \quad (5.14)$$

In this case, the induced polarization has terms oscillating at a new frequency 3ω , which represent *third-harmonic generation* (THG). In principle, THG is qualitatively similar to SHG: it is also a coherent, parametric process, where 3 instead of 2 photons with energy $\hbar\omega$ are combined to create a photon with energy $3\hbar\omega$.

The remaining terms in eq. 5.14 oscillate at the fundamental frequency ω , and thus according to eq. 5.11 will have direct impact on the original field, leading to an intensity dependent refractive index (known as the *Kerr effect*) and nonlinear absorption if $\chi^{(3)}$ has a nonzero imaginary part. The latter effect can be shown by considering the time-averaged work done by the electromagnetic field on the medium, along the lines of the linear case in section 2.2.1:

$$\left\langle \bar{E} \cdot \frac{\partial \bar{P}}{\partial t} \right\rangle = \frac{1}{2} \operatorname{Re} \left\{ E \frac{\partial P^*}{\partial t} \right\} = -\frac{3\epsilon_0\omega}{2} |E|^4 \chi''^{(3)}. \quad (5.15)$$

A non zero time-averaged energy transfer to the medium described the nonlinear absorption or gain, depending on the sign of $\chi''^{(3)}$ and .

The third order absorption process is also known as *two-photon absorption* (TPA). In a (again, simplified) quantum-mechanical picture, two photons with energy $\hbar\omega$ are simultaneously (via a virtual state) absorbed to excite an atom (or just an electron) to a real quantum-mechanical state. Thereby, in comparison to THG, TPA is also coherent, but not parametric as it involves transitions to real states.

It should be noted that an incoherent TPA is also possible if the process of absorbing two photons is mediated by a transition to a real intermediate state (in contrast to a virtual intermediate state in the case of coherent absorption). Incoherent TPA is a cascaded $\chi^{(1)} : \chi^{(1)}$ absorption, which is effectively a $\chi^{(3)}$ -processes [87]. The importance of this process for the nonlinear absorption in gold is discussed in the next section.

A brief historical reference concludes this section: the two-photon absorption was predicted by Goepfert-Mayer in 1931 [88], however the first experimental observation followed only 30 years later, also after the invention of lasers, by Kaiser et al. [89].

5.5 Nonlinear optical properties of gold

As outlined in the previous sections, knowledge about the nonlinear electric susceptibility of a material is crucial for the description of nonlinear light-matter interactions. Nevertheless, $\chi^{(2)}$ and $\chi^{(3)}$ are hard to determine experimentally and nontrivial to model theoretically, especially in non-transparent materials, such as gold and other noble metals. This section reviews relevant physical mechanisms and microscopic origins of the second- and third-order nonlinear effects in gold.

5.5.1 Second-order nonlinearities in gold

As gold is a centrosymmetric material, its bulk value of $\chi^{(2)}$ vanishes in the electric dipole approximation. However, inversion symmetry is broken at the boundary of the metal, enabling a second-order nonlinear response at the surface. Furthermore, effective second-order polarization is possible even in the bulk due to electric-quadrupole and magnetic dipole contributions.

These contributions are usually formulated in terms of the surface-tangential, surface-normal and bulk-tangential currents, and were extensively studied within the free electron and hydrodynamic models [90–94]. Some studies indicated that the surface contribution is expected to be dominant [82, 83]. However, there is no unambiguous way to define a boundary that separates the surface of the gold from its bulk [95–97], so the choice of an appropriate model remains under discussion even today [98]. In fact, this ambiguity might also affect the susceptibility values which are extracted from experimentally obtained data. While it was argued that it might not be possible to separate the surface from the bulk response in the overall SHG signal [96], sophisticated polarization-resolved measurements with an analysis based on the phenomenological model by Rudnick and Stern [91] confirmed that the surface contribution indeed dominates over the higher-order multipole bulk nonlinearities [99–101].

Furthermore, the free electron and hydrodynamic models only include the response from quasi-free conduction electrons, while the response of real metals is complicated by the presence of the bound electrons and their contribution to interband transitions [102–104]. Nevertheless, regardless of the exact microscopic origin of the second-order nonlinearity, it remains effectively a surface effect. Even the bulk-like quadrupole response is, in fact, caused by the strong electric field gradients at the metal surface, which extend into the bulk by few tens of nanometers (in contrast to the true surface contribution which originates from the layer of few angstroms in thickness). Hence, the quadrupole contribution is also affected by the structural shape of the surface which defines the field gradients and thus, the overall SHG is highly dependent on the details of sample surface preparation, including aspects such as roughness [105–107], film thickness [108, 109], crystal orientation [99, 110], possible adsorbents [111–114], etc. All these factors, as well as strong dispersion and dependence on the excitation pulse length [115–119], make finding the “true” $\chi^{(2)}$ value of gold very intricate. As a result, values obtained under different experimental conditions differ by orders of magnitude (e.g. $\chi_{zzz}^{(2)\text{surf}} \approx 1.4 \cdot 10^{-19} \text{ m}^2/\text{V}$ was reported in ref. [100] and $\chi_{zzz}^{(2)\text{surf}} \approx 6.5 \cdot 10^{-18} \text{ m}^2/\text{V}$ in ref. [101]). Appendix C presents a paper regarding the anisotropy in SHG from monocrystalline gold flakes, which also includes a relevant general discussion on the topic.

In the case of nanostructured metals, SHG can be significantly enhanced by engineering the shape and size of the constitutive nanoparticles and their arrangements to support excitation of localized surface plasmon resonances at either the fundamental or the SH frequency. As a result, the driving field can be efficiently coupled to the surface plasmon modes and exploit the associated field enhancements to amplify the intrinsic material nonlinearity. Exploration of these effects is a subject of research in the broad field of *nonlinear plasmonics*. The immense progress in this ever-growing field has been summarized in a number of recent reviews [42, 120–123].

5.5.2 Third-order nonlinearities in gold

Even though third-order effects are not symmetry-forbidden in bulk gold, their description and quantitative measurement is by no means trivial. In fact, the discrepancy in the experimentally obtained values of $\chi^{(3)}$ is even worse than in case of $\chi^{(2)}$, and it spans several orders of magnitude, especially in its imaginary part [124]. Apart from the strong dispersion and details of the sample preparation, this discrepancy is caused by differences in the employed experimental methods, as they might exploit different physical processes. For example, the z-scan technique [125] measures the intensity-dependent refractive index (Kerr nonlinearity) or nonlinear absorption, and is particularly sensitive to the imaginary part of $\chi^{(3)}$. In contrast, experiments that employ THG [126] measure the modulus of the complex third-order susceptibility. As THG is not in the scope of the experimental part of

this thesis, the focus in this section is put on the TPA and related physical mechanisms.

In order to understand the involved interactions and the underlying physical origins of TPA in metals, the electronic band structure needs to be considered.

As sketched in fig. 5.1, TPA can occur in several ways, usually near the X and L symmetry points of the first Brillouin zone. These points are associated with approximately parabolic dispersion curves and high DOS due to the van Hove singularities [127, 128]. A first possibility is the coherent absorption of two photons, which is labeled c TPA in the diagram. In this case, two photons are absorbed simultaneously (mediated by a virtual intermediate state) to create a hole in the d -band and an excited electron in the conduction sp -band above the Fermi level, as if a single photon with energy $2\hbar\omega$ was absorbed. However, experimental studies on TPA dynamics indicate that the intermediate state has a lifetime on the order of few hundred femtoseconds [129, 130], suggesting that such transitions have low probabilities [131].

Another possibility is an incoherent, cascaded absorption, which is an effective third-order process involving a real intermediate state. One specific transition sequence is the following: the first photon excites, via an intraband transition, an electron in the sp -band. This creates a vacancy below, and a hot electron above the Fermi level. Both carriers may then relax back to the Fermi level and recombine nonradiatively on the time scale of a picosecond via thermalization [132, 133]. Alternatively, the sp -band vacancy may be filled with an electron from the d -band via an interband transition caused by the absorption of the second photon. If this interband transition actually happens within the lifetime of the sp -band hole, then such an absorption cascade also results in an electron-hole pair as in case of coherent TPA. Thus, the lifetime of the intermediate state is defined by the lifetime of the sp -band vacancy [129, 130].

It is important to note that the first intraband transition requires a source of additional momentum, which photons alone cannot provide. Thus, at least in the electric dipole approximation, TPA is expected to be absent at flat gold surfaces [134]. However, intraband absorption may occur when an electron absorbs a photon and simultaneously undergoes scattering on a phonon or impurity, which compensates the momentum mismatch [135]. For this reason, TPA is significantly enhanced at rough surfaces [136] and in nanostructures, where, due to the strong field gradients, the dipolar approximation is no longer valid [137]. In fact, excitation of plasmonic resonances in the nanostructures at the fundamental frequency often determines the overall TPA efficiency [138, 139].

Eventually, the d -band hole and hot electron may recombine radiatively, i.e. by emitting a photon. This process is called *photoluminescence* (PL), but in the special case when it is initiated by TPA, it is often referred to as two-photon photoluminescence (TPL). However, other nomenclature with similar abbreviations is also widespread in the literature: TPPL, 2PPL, TPEF, 2PEF, etc. Photoluminescence from gold was observed for the first time by Mooradian et al. in 1969 [140].

Since all charge carriers are dynamically redistributed prior to the radiative recombination, TPL emission has a broad distribution in photon energies, spanning the whole visible range (which is indicated with the rainbow-colored arrows in the diagram in fig. 5.1). In the absence of other resonances, the TPL spectrum is expected to show 2 peaks: one at approx. 1.9 eV and the other at approx. 2.4 eV. These energies correspond to the energy differences between the Fermi level and d -band near X and L symmetry points respectively [131]. If the sample is monocrystalline, only one peak may be observed, depending on the crystal orientation. For example, if a monocrystalline gold flake is illuminated along the

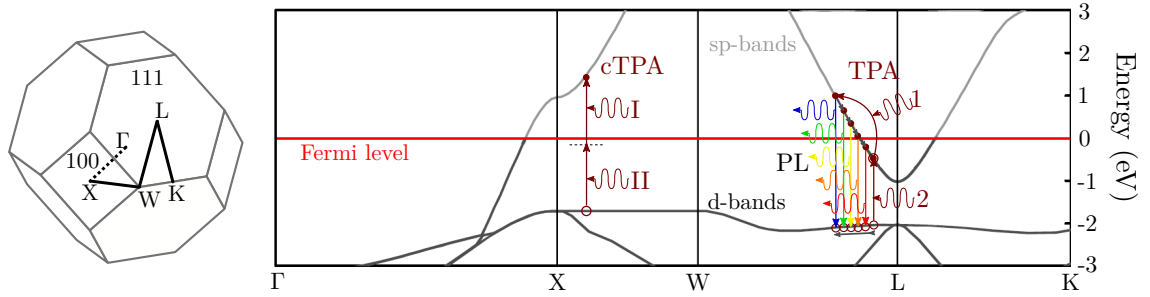


Figure 5.1: First Brillouin zone and band structure of gold with indicated electronic transitions that are associated with third order nonlinear processes: coherent two-photon absorption (cTPA) and incoherent absorption (TPA), both indicated with dark-red arrows. The non-radiative relaxation of hot electrons (thermalization) is shown with gray arrows. The subsequent photoluminescence (PL) is shown with rainbow-colored arrows. Open circles denote holes created in the process, closed circles denote excited electrons. Adapted with permission from ref. [26]. Copyrighted by the American Physical Society.

$\langle 111 \rangle$ crystal axis, only one peak at ≈ 520 nm is present, which corresponds to the ≈ 2.4 eV interband transition at the L symmetry point [26].

Furthermore, hot electrons and holes in the sp -band may also recombine nonradiatively, for example by coupling to surface plasmon modes, which, in turn, may decay radiatively, contributing to the overall TPL emission. In fact, in many cases, the contribution from the localized SPP modes to the TPL from gold nanostructures dominates and shapes its spectrum [141, 142] and emission lifetime [143]. Therefore, various TPL scanning microscopy methods have become widely used tools for mapping the distribution of the plasmonic LDOS and the associated field enhancements [24, 144–149].

However, there are other possibilities for incoherent photon absorption processes which lead to effectively higher-order nonlinear absorption. For example, the vacancy in the sp -band created after the absorption of the first photon may be filled with another sp -band electron via a second intraband absorption, effectively bringing the vacancy inside the sp -band closer to the d -band, and thus increasing opportunities for subsequent interband transitions. Furthermore, hot electrons may gain energy by undergoing another intraband transition to climb higher in the sp -band, resulting in a greater energy of the subsequent PL emission. In principle, any sequence of interband and intraband transitions may contribute to an absorption cascade, resulting in a cumulative *multi-photon absorption* (MPA) [150]. Overall, the number of transitions involved in the cascade defines the dependence on the intensity of incident light, and thus sets the effective order of nonlinearity of the process. Photoluminescence which follows such an absorption cascade is often referred to as multi-photon photoluminescence (MPL), as well as MPPL, MPIF, MAIL, etc. Quite often, TPA and MPA of various orders occur simultaneously, which results in non-integer values of the overall intensity dependence, with exponents ranging from 2 to 5. Typically, the order of nonlinear process depends on the excitation wavelength, intensity [130, 151], and pulse duration [129].

Finally, spectrally resolved MPL measurements show that the blue part of the emission has a higher order dependence on the excitation intensity and a shorter intermediate state lifetime [151, 152], which is consistent with the described MPA mechanism.

6 Nonlinear microscopy of monocrystalline gold flakes

This chapter describes the experimental studies of the nonlinear optical properties of monocrystalline gold flakes and is structured in the following way: the first section provides details about the nonlinear optical setup; the second section is devoted to SH and TPL imaging of the field enhancement associated with sharp features of the gold flakes; the last section of the chapter presents preliminary results on pulse-correlation measurements of ultrafast TPL dynamics in gold flakes with mesoscopic thickness.

6.1 Experimental setup

A significant part of my PhD time was spent on the development of an experimental setup for characterizing nonlinear effects in plasmonics. An old, “home-made” scanning nonlinear optical microscope (a.k.a “TPL setup” at the Centre for Nano Optics became outdated by the year 2018 and required major upgrades. The malfunctioning scanning piezo-stage needed replacement, which entailed rewriting the entire control software to make it compatible with all other electronic devices. Basically, only the femtosecond laser source (mode-locked Titanium:Sapphire laser, Tsunami 3941 by Spectra-Physics) remained unchanged, all other components were upgraded.

A schematic diagram of the nonlinear optical setup is shown in fig. 6.1. Its main part –the scanning optical microscope – allows to scan a tightly focused laser beam across the sample and detect the variation in intensity of the linear and nonlinear reflection, thereby recording an image of the sample pixel by pixel. Tight focusing of the excitation beam and efficient collection of the reflected light is achieved using a high numerical aperture (NA=0.9) apochromatic objective. The nonlinear part of the signal is separated using a dichroic mirror (DM) and can be detected using either a photo-multiplier tube (PMT) or a spectrometer. Reflection at the fundamental frequency is detected using a high-sensitivity photodiode.

The setup is modular and has functionality to switch between free-space and fiber coupling to the microscope module. Although propagation in an optical fiber chirps the fs-pulses in time due to dispersion, it has the advantage of shaping the output beam to a nearly perfect Gaussian profile. Feeding the fiber through an electronic variable optical attenuator (EVOA) allows precise control and stabilization of the average power. Furthermore, fast response time of the EVOA is useful for writing patterns in various materials by laser-heat-induced modification (e.g. laser-printing of structural plasmonic colors, see ref. [21]).

Free space coupling is generally beneficial for TPL and SHG microscopy, as it does not stretch the laser pulses in time. The pulse duration is a crucial parameter in experimental nonlinear optics, as concentrating the electromagnetic energy in a short period of time results in high peak power, which allows the observation of even weak nonlinear effects. Furthermore, as will be shown in section 6.3, ultrashort pulses allow to characterize ultrafast dynamics of cascaded nonlinear processes. However, in order to resolve the timescale of such fast processes, the duration of the pulse itself needs to be characterized. Quoting the words of one of the pioneers of the ultrafast optics field, Prof. Rick Trebino, *“In order to measure an event in time, you must use a shorter one. But then, to measure the shorter event, you must use an even shorter one. And so on. So, now, how do you measure the shortest event ever created?”* [153].

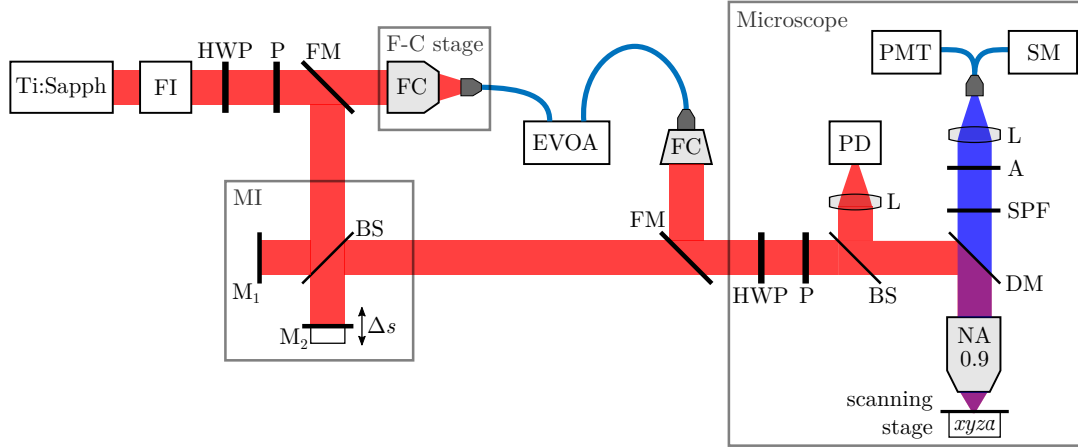


Figure 6.1: Schematic diagram of the nonlinear optical setup: the mode-locked Ti:Sapph laser outputs approx. 100 fs pulses, tunable in the 750 – 900 nm wavelength range. A Faraday insulator (FI) prevents light reflection back to the laser cavity. A combination of a half-wave plate (HWP) and a polarizer (P) are used to adjust the intensity and polarization of the beam. The further beam path can be selected with a flip-mirror (FM): the beam can be either coupled to an optical fiber (F-C stage) or propagate in free-space into a Michelson interferometer (MI). In MI, the mirror M_1 is kept fixed, while M_2 is mounted on a motorized translation stage, allowing precise control over the interferometer arm length difference Δs . In the microscope the excitation beam is focused to a diffraction-limited spot using a NA=0.9 apochromatic objective, which is also used for collection of the reflected light. The nonlinear part of the signal is separated using a dichroic mirror (DM) and can be detected using a fiber-coupled photo-multiplier tube (PMT). Alternatively, the spectrum of the nonlinear signal can be analyzed using a spectrometer (SM). Other labels in the diagram have the following designations: fiber collimator (FC), beam splitter (BS), electronic variable optical attenuator (EVOA), short-pass filter (SPF), lens (L) and photodiode (PD).

The duration of fs-pulses cannot be directly measured using conventional optoelectronic devices, since the response time of usual photodetectors is on the order of nanoseconds, in the best case fractions of a nanosecond. Therefore, methods for the characterization of ultrashort pulses rely on the principles of *optical autocorrelation*. One of the standard approaches is the interferometric autocorrelation (IAC), in which two identical copies of a pulse are created in a Michelson interferometer (MI, schematically depicted in fig. 6.1). At the output of the interferometer, the autocorrelation signal is produced via SHG in a nonlinear crystal. The intensity of the nonlinear signal depends on the time delay τ between the pulses and can be measured using a slow photodetector. Sweeping the time delay by changing the optical path difference between the interferometer arms ($\tau = 2\Delta s/c$) and recording the variation in nonlinear signal allows to get a rough estimate of the pulse duration. Figure 6.2 shows a result of such a sweep for a Ti:Sapph light pulse with 800 nm central wavelength, obtained using a lithium niobate (LiNbO_3) crystal as the nonlinear medium.

However, extracting the exact value of the pulse duration from the intensity autocorrelation data is not trivial, since it is an inverse problem of deconvolution:

$$I_{2\omega}(\tau) \propto \int_{-\infty}^{\infty} |E(t)E(t-\tau)|^2 dt \propto \int_{-\infty}^{\infty} I(t)I(t-\tau) dt. \quad (6.1)$$

Hence, retrieval of $I(t)$ from the measured $I_{2\omega}(\tau)$ requires an assumption of the pulse shape. Luckily, the documentation of our Ti:Sapph laser specifies that pulses have sech^2 shape and suggests to use a deconvolution factor of 0.65 (meaning that the actual pulse duration is shorter than the width of the autocorrelation function approximately by the

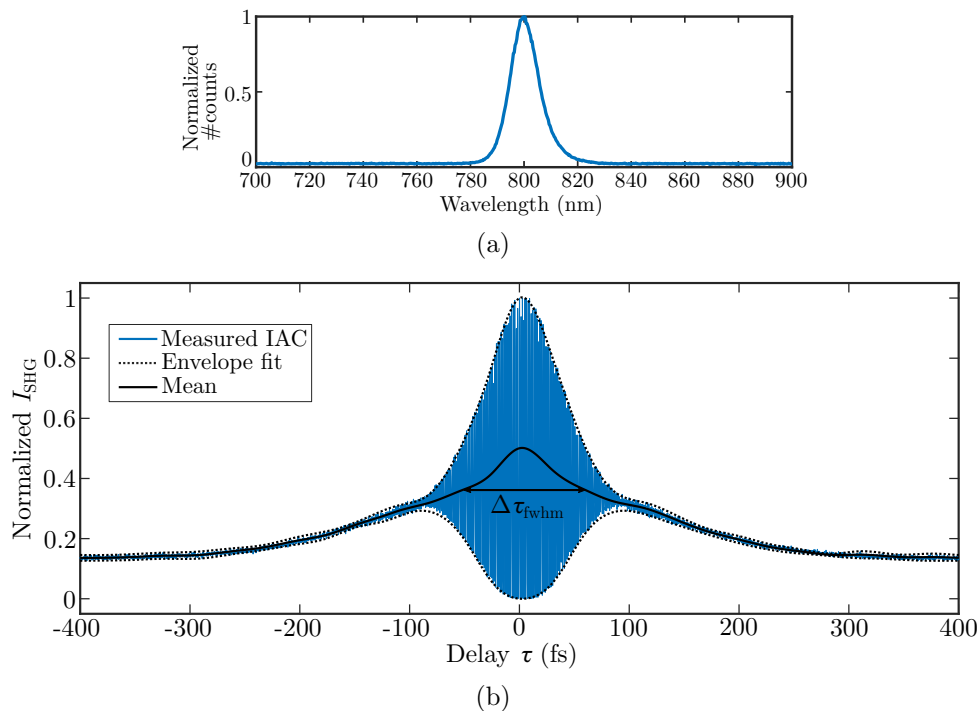


Figure 6.2: (a) Spectrum of the pulsed output of Ti:Sapph tuned to 800 nm central wavelength. (b) Pulse interferometric autocorrelation measurement using a LiNbO_3 nonlinear crystal. The shoulders in the interferogram indicate that the pulse is somewhat chirped due to the dispersion in optical components of the microscope. FWHM of the mean of envelopes is $\Delta\tau_{\text{FWHM}} \approx 175$ fs.

factor 0.65). Thereby, an estimate of a full width at half maximum (FWHM) pulse duration based on the measurement shown in fig. 6.2b yields $\tau_p = 0.65\Delta\tau_{\text{FWHM}} \approx 115$ fs. It should be stressed that this value is only approximate, since an IAC measurement contains only limited information about the phase of the pulse. More sophisticated techniques, such as frequency resolved optical gating (FROG), allow to measure the pulse duration with higher precision [153]. Nevertheless, a simple IAC is easy to implement and is sufficient for the needs of the experiments described in section 6.3.

6.2 SHG and TPL imaging of monocrystalline gold flakes

Figure 6.3 shows a comparison of images of a thick (approx. $2\ \mu\text{m}$) gold flake sample obtained with different microscopy methods. Undoubtedly, among the presented micrographs, the SEM image has the highest resolution and can clearly resolve the morphology of the sample, sharp edges and difference in the adjacent side facets of the crystal. White light reflection microscopy is considerably worse – the sharp edges of the flake appear blurred in BF and two-colored in DF. A detailed discussion on the origin of the distinct colors of adjacent and opposite edges in DF images is provided in appendix A. In short, it is caused by interference of SPP propagating at the side facets and specularly reflected light at a grazing angle. Among the images obtained using the nonlinear microscope, the SH image is the sharpest. Due to the strong SHG at the surface of crystalline gold (described in appendix C) the signal-to-noise ratio in this image is much higher as compared to the TPL map. An increase in the intensity at the flake edges which are perpendicular to the polarization of excitation light are visible in both SH and TPL maps. This can be attributed to the plasmonic field enhancements at the sharp corners of the crystal. As was mentioned in chapter 5, scanning nonlinear microscopy is a widely used tool for mapping localized field

enhancements in plasmonic nanostructures [24, 145, 147, 154].

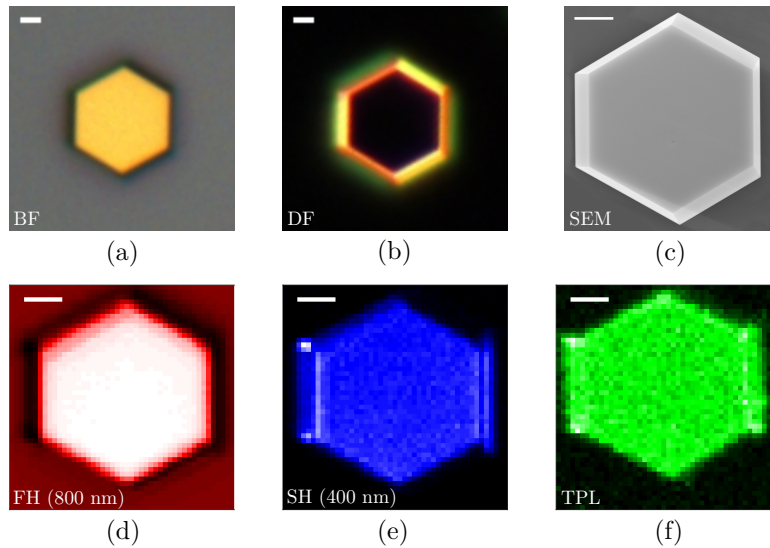


Figure 6.3: Various images of a gold flake sample with approx. $2\ \mu\text{m}$ thickness: (a) white light reflection BF; (b) white light reflection DF; (c) SEM; (d) FH reflection at $800\ \text{nm}$ (e) SH at $400 \pm 10\ \text{nm}$; (f) TPL integrated over the $450 - 650\ \text{nm}$ wavelength range. The optical images in (a) and (b) were obtained using a $\times 100$ magnification objective ($\text{NA}=0.9$). The excitation light at $800\ \text{nm}$ central wavelength in images (d-f) is horizontally polarized.

To better appreciate the resolution limit of SH and TPL microscopy, fig. 6.4 shows close-up images of the corners of the flake sample obtained with $100 \times 100\ \text{nm}$ scanning pixel size. Again, the SH image is clearly the sharpest and displays features that are invisible in the FH image. Although SH microscopy does not allow to see the actual morphology of the crystal, it clearly resolves the edges of the side facets, which are separated by approx. $350\ \text{nm}$, as estimated from the SEM image in fig. 6.3. Thus, the resolution limit of scanning nonlinear microscopy is approx. 25% better than the conventional diffraction limit at $800\ \text{nm}$ wavelength ($d = \lambda/2\text{NA} \approx 440\ \text{nm}$).

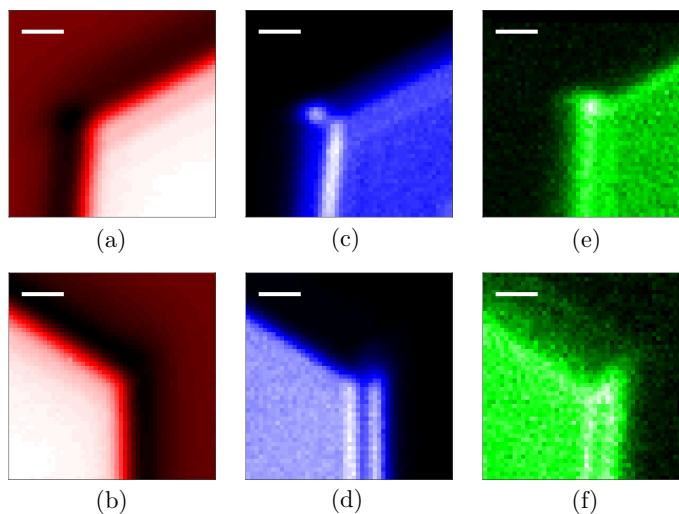


Figure 6.4: High resolution images of the upper left and upper right corners of the flake from fig. 6.3: (a-b) FH; (c-d) SH; (e-f) TPL. Excitation light is horizontally polarized.

6.3 Ultrafast measurement of nonlinear dynamics

Figure 6.5 shows various images of a gold flake sample with thickness varying in a “terraced” fashion (approx 35 – 25 nm). In case of thin flakes, the TPL signal is much stronger than that from optically thick samples and increases with decreasing gold thickness. This is consistent with previous observations reported in ref. [26]. In this work, Großmann et al., attributed the strong increase of TPL intensity to a modification of the band structure in crystalline films with thickness below 30 nm due to quantum surface effects. Due to the finite number of atomic layers in the surface-normal direction (corresponding to the $\langle 111 \rangle$ crystal axis), the sp -band splits into discrete bands near the L symmetry point, which increases the probability of exciting an electron above the Fermi level. These transitions create vacancies below the Fermi level, which, as discussed in section 5.5, can be filled with electrons in lower-lying bands, resulting in a cascaded TPA.

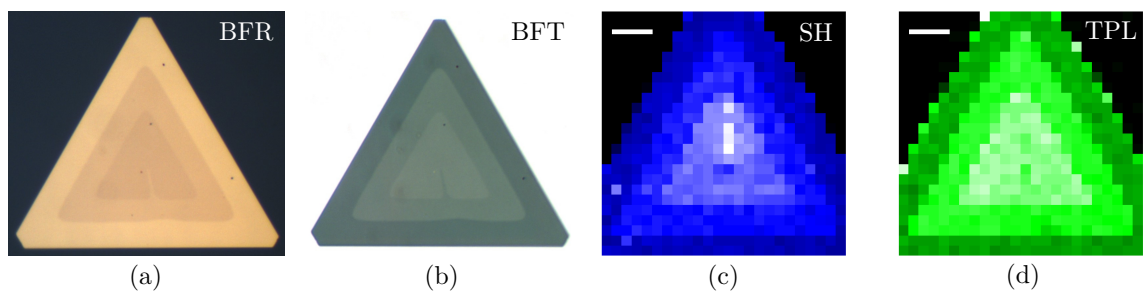


Figure 6.5: Various optical micrographs of a “terraced” flake sample with thickness varying from ~ 35 nm at the edge, to ~ 30 nm and to ~ 25 nm in the center: (a) white light reflection; (b) white light transmission; (c) SH at 400 ± 10 nm; (d) TPL integrated in 450 – 650 nm wavelength range.

Spectra of the nonlinear signal from 3 spots of the sample corresponding to different thicknesses (~ 35 nm, ~ 30 nm and ~ 25 nm, measured using an AFM) are shown in fig. 6.6a. As can be seen, the intensity of both, the SH peak at 400 nm and the broad TPL are increased by more than a factor of two as the gold thickness decreases by 10 nm.

Figure fig. 6.6b shows two-pulse correlation measurements of the TPL intensity from the same three spots of the sample. These measurements are performed in the same way as the interferometric pulse characterization described in section 6.1, only considering larger delays between the two copies of the pulse. Such a characterization allows to investigate the temporal dynamics of hot-carrier relaxation during the cascaded TPA: sweeping the time delay between the two pulses essentially allows to measure the relaxation time of the vacancies in the sp -bands below the Fermi level, which are required as an intermediate state for the cascaded two-photon absorption.

In comparison with the SHG from a LiNbO_3 crystal, which does not depend on the time delay τ if pulses are separated by more than 400 fs, the TPL intensity of gold exponentially decreases with increasing τ . Fitting an exponential function to the data shown fig. 6.6b gives an estimate of the intermediate state lifetime τ_d . This time constant appears to be dependent on the thickness of the gold flake: least-square-fits resulted in $\tau_d \approx 411$ fs, $\tau_d \approx 421$ fs and $\tau_d \approx 438$ fs for ~ 35 nm, ~ 30 nm and ~ 25 nm thicknesses respectively.

Finally, fig. 6.6c shows the power dependence of the nonlinear luminescence. At low excitation powers (below $P = 10$ mW, time-averaged) the intensity shows quadratic dependence, suggesting that the cascaded absorption involves two transitions, which corresponds to an effective third-order TPA. With increasing excitation power, the exponential order of intensity dependence smoothly increases to approx. 4. This suggests that the cascaded absorption involves more intermediate states, which corresponds to a higher-order effective

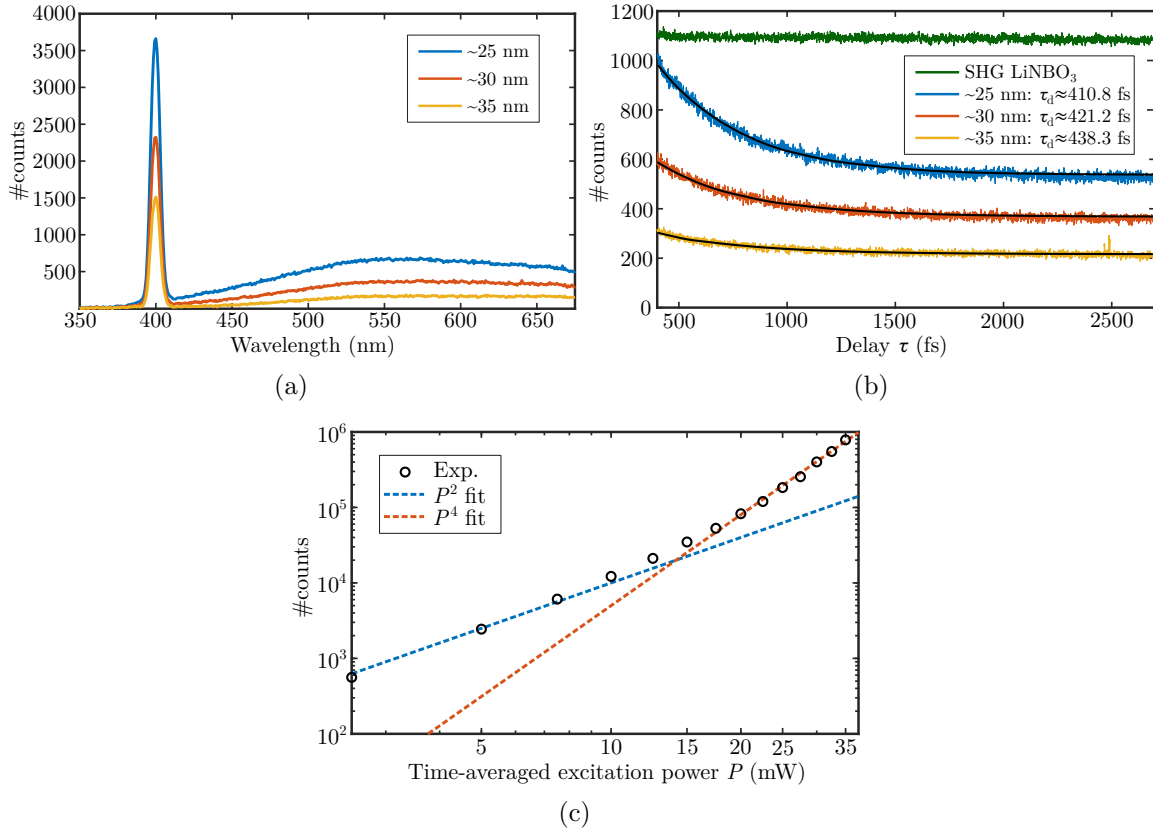


Figure 6.6: (a) Spectrally resolved nonlinear signal from 3 spots with different thicknesses of the gold flake shown in fig. 6.5. (b) Two-pulse correlation measurements of the TPL intensity at the same three spots in comparison with the SHG response from a LiNBO₃ crystal (TPL signal is integrated in 450 – 650 nm wavelength range and SH signal is measured at 400 ± 10 nm). (c) Dependence of the nonlinear luminescence intensity on the excitation power plotted on a double-logarithmic scale: increasing the time-averaged excitation power P increases the effective nonlinear order of the cascaded photon absorption. In all measurements the nonlinear signal was excited by approx. 115 fs pulses at 800 nm central wavelength. The data in (a) and (b) was acquired at approx. 5 mW of time-averaged excitation power.

nonlinear absorption (i.e. three- and four-photon absorption).

Further experiments and theoretical analysis are required in order to get new insights to the ultrafast dynamics of nonlinear processes in mesoscopic gold.

7 Summary and outlook

To summarize, this PhD thesis presents an experimental study of plasmonic properties of monocrystalline gold flakes in linear and nonlinear regimes. Both applied and fundamental aspects are investigated, with a primary focus on nonlocal effects in ultrathin metal-insulator-metal gaps and nonlinear phenomena at gold surfaces.

The opening chapter of the thesis presents an overview of the field and introduces the scope of the study. The theoretical foundations of linear plasmonics, including formalism of nonlocal corrections for gap surface plasmons, are presented in chapter 2. Chapter 3 is devoted to the fabrication of gold flakes and details of their crystal structure. In chapter 4, superior plasmonic properties of the gold flakes are employed in the fabrication of plasmonic waveguides with an extremely small dielectric gap. Furthermore, preliminary results of optical characterization with state of the art near-field microscopy techniques are reported. Chapter 5 provides an overview of the physical principles of nonlinear light-metal interaction. Finally, chapter 6 reports the characterization of nonlinear optical properties of monocrystalline gold flakes using two-photon luminescence and second-harmonic generation scanning microscopy. In addition, two-pulse correlation measurements are used to investigate the ultrafast dynamics of nonlinear absorption in gold flakes with mesoscopic thickness.

The main research findings of the PhD study published as journal articles prior to the thesis submission constitute the appendix. It includes three papers closely related to the general scope of the thesis: interference in edge-scattering from monocrystalline gold flakes; use of monocrystalline gold flakes for gap plasmon-based metasurfaces operating in the visible; anisotropic second-harmonic generation from monocrystalline gold flakes.

Outlook

I hope that this PhD thesis convinced the interested reader that monocrystalline gold flakes are an attractive material platform for the implementation of high-quality nanoplasmonic devices and a nearly ideal “playground” for the experimental research in mesoscopic-scale solid state physics. The results presented here, as well as in other publications that I was glad to co-author in the course of my PhD studies, reveal the potential of crystalline gold films for future applications in quantum-plasmonic devices, plasmonic sensing, high-resolution microscopy, and other.

Preliminary results on the near-field characterization of gap surface plasmon waveguides look promising but are not yet complete to judge the importance of the nonlocal effects. Further experimental and theoretical work is also needed to improve our understanding of the femtosecond-scale dynamics of nonlinear absorption and luminescence processes. This investigation can eventually become useful for improving the existing technologies that rely on plasmon-induced hot carrier generation, such as photodetection, plasmon-assisted photocatalysis and light energy harvesting.

Bibliography

- [1] D. K. Gramotnev and S. I. Bozhevolnyi. “Plasmonics beyond the diffraction limit”. *Nature Photonics* 4 (2010), 83–91.
- [2] J. J. Baumberg et al. “Extreme nanophotonics from ultrathin metallic gaps”. *Nature Materials* 18 (2019), 668–678.
- [3] J. B. Khurgin. “How to deal with the loss in plasmonics and metamaterials”. *Nature Nanotechnology* 10 (2015), 2–6.
- [4] J. B. Khurgin and G. Sun. “In search of the elusive lossless metal”. *Applied Physics Letters* 96 (2010), 181102.
- [5] G. V. Naik, V. M. Shalaev, and A. Boltasseva. “Alternative plasmonic materials: beyond gold and silver”. *Advanced Materials* 25 (2013), 3264–3294.
- [6] S. Nie and S. R. Emory. “Probing single molecules and single nanoparticles by surface-enhanced Raman scattering”. *Science* 275 (1997), 1102–1106.
- [7] L. R. Hirsch et al. “Nanoshell-mediated near-infrared thermal therapy of tumors under magnetic resonance guidance”. *Proceedings of the National Academy of Sciences* 100 (2003), 13549–13554.
- [8] G. Qiu et al. “Dual-functional plasmonic photothermal biosensors for highly accurate severe acute respiratory syndrome coronavirus 2 detection”. *ACS Nano* 14 (2020), 5268–5277.
- [9] C. Haffner et al. “Low-loss plasmon-assisted electro-optic modulator”. *Nature* 556 (2018), 483–486.
- [10] M. Thomaschewski et al. “Plasmonic monolithic lithium niobate directional coupler switches”. *Nature Communications* 11, 748 (2020).
- [11] M. S. Tame et al. “Quantum plasmonics”. *Nature Physics* 9 (2013), 329–340.
- [12] S. I. Bozhevolnyi and J. B. Khurgin. “The case for quantum plasmonics”. *Nature Photonics* 11 (2017), 398–400.
- [13] S. I. Bozhevolnyi and N. A. Mortensen. “Plasmonics for emerging quantum technologies”. *Nanophotonics* 6 (2017), 1185–1188.
- [14] A. I. Fernández-Domínguez, S. I. Bozhevolnyi, and N. A. Mortensen. “Plasmon-enhanced generation of nonclassical light”. *ACS Photonics* 5 (2018), 3447–3451.
- [15] H. Siampour et al. “Ultrabright single-photon emission from germanium-vacancy zero-phonon lines: deterministic emitter-waveguide interfacing at plasmonic hot spots”. *Nanophotonics* 9 (2020), 953–962.
- [16] S. Kumar et al. “Efficient coupling of single organic molecules to channel plasmon polaritons supported by V-grooves in monocrystalline gold”. *ACS Photonics* 7 (2020), 2211–2218.
- [17] N. Yu and F. Capasso. “Flat optics with designer metasurfaces”. *Nature Materials* 13 (2014), 139–150.
- [18] S. Boroviks et al. “Multifunctional metamirror: polarization splitting and focusing”. *ACS Photonics* 5 (2017), 1648–1653.
- [19] J. Zhang et al. “Plasmonic metasurfaces with 42.3% transmission efficiency in the visible”. *Light: Science & Applications* 8, 53 (2019).
- [20] A. Kristensen et al. “Plasmonic colour generation”. *Nature Reviews Materials* 2, 16088 (2017).
- [21] A. S. Roberts et al. “Laser writing of bright colors on near-percolation plasmonic reflector arrays”. *ACS Nano* 13 (2018), 71–77.
- [22] M. L. Brongersma and P. G. Kik. *Surface plasmon nanophotonics*. Vol. 131. Springer, 2007.

- [23] J.-S. Huang et al. “Atomically flat single-crystalline gold nanostructures for plasmonic nanocircuitry”. *Nature Communications* 1, 150 (2010).
- [24] S. Viarbitskaya et al. “Tailoring and imaging the plasmonic local density of states in crystalline nanoprisms”. *Nature Materials* 12 (2013), 426–432.
- [25] B. Frank et al. “Short-range surface plasmonics: Localized electron emission dynamics from a 60-nm spot on an atomically flat single-crystalline gold surface”. *Science Advances* 3 (2017), e1700721.
- [26] S. Großmann et al. “Nonclassical optical properties of mesoscopic gold”. *Physical Review Letters* 122 (2019), 246802.
- [27] K. J. Kaltenecker et al. “Mono-crystalline gold platelets: a high-quality platform for surface plasmon polaritons”. *Nanophotonics* 9 (2020), 509–522.
- [28] D. Griffiths. *Introduction to Electrodynamics*. Pearson, 2013. ISBN: 9780321856562.
- [29] S. Maier. *Plasmonics: Fundamentals and Applications*. Springer US, 2007. ISBN: 9780387378251.
- [30] P. Powers and J. Haus. *Fundamentals of Nonlinear Optics*. CRC Press, 2017. ISBN: 9781498736862.
- [31] N. Ashcroft and N. Mermin. *Solid State Physics*. Cengage Learning, 2011. ISBN: 9788131500521.
- [32] M. P. Marder. *Condensed matter physics*. John Wiley & Sons, 2010. ISBN: 9780470617984.
- [33] W. Cai and V. M. Shalaev. *Optical metamaterials*. Springer-Verlag New York, 2010. ISBN: 9781441911513.
- [34] R. L. Olmon et al. “Optical dielectric function of gold”. *Physical Review B* 86 (2012), 235147.
- [35] P. B. Johnson and R. W. Christy. “Optical Constants of the Noble Metals”. *Physical Review B* 6 (1972), 4370–4379.
- [36] E. D. Palik. *Handbook of optical constants of solids*. 1985.
- [37] B. Hoffmann et al. “New insights into colloidal gold flakes: structural investigation, micro-ellipsometry and thinning procedure towards ultrathin monocrystalline layers”. *Nanoscale* 8 (2016), 4529–4536.
- [38] D. Barchiesi and T. Grosjes. “Fitting the optical constants of gold, silver, chromium, titanium, and aluminum in the visible bandwidth”. *Journal of Nanophotonics* 8 (2014), 083097.
- [39] H. Sehmi, W. Langbein, and E. Muljarov. “Optimizing the Drude-Lorentz model for material permittivity: Method, program, and examples for gold, silver, and copper”. *Physical Review B* 95 (2017), 115444.
- [40] T. Gharbi et al. “Fitting optical properties of metals by Drude-Lorentz and partial-fraction models in the [0.5; 6] eV range”. *Optical Materials Express* 10 (2020), 1129–1162.
- [41] F. Ladstädter et al. “First-principles calculation of hot-electron scattering in metals”. *Physical Review B* 70 (2004), 235125.
- [42] M. B. Raschke, S. Berweger, and J. M. Atkin. “Ultrafast and nonlinear plasmon dynamics”. *Plasmonics: Theory and Applications*. Springer, Dordrecht, 2013, 237–281. ISBN: 9789400778047.
- [43] S. I. Bozhevolnyi and J. Jung. “Scaling for gap plasmon based waveguides”. *Optics Express* 16 (2008), 2676–2684.
- [44] J. B. Khurgin. “Ultimate limit of field confinement by surface plasmon polaritons”. *Faraday Discussions* 178 (2015), 109–122.
- [45] G. Onida, L. Reining, and A. Rubio. “Electronic excitations: density-functional versus many-body Green’s-function approaches”. *Reviews of Modern Physics* 74 (2002), 601.

- [46] A. Varas et al. “Quantum plasmonics: from jellium models to ab initio calculations”. *Nanophotonics* 5 (2016), 409–426.
- [47] F. J. Garcia de Abajo. “Nonlocal effects in the plasmons of strongly interacting nanoparticles, dimers, and waveguides”. *The Journal of Physical Chemistry C* 112 (2008), 17983–17987.
- [48] S. Raza et al. “Unusual resonances in nanoplasmonic structures due to nonlocal response”. *Physical Review B* 84 (2011), 121412.
- [49] Y. Luo et al. “Surface plasmons and nonlocality: a simple model”. *Physical Review Letters* 111 (2013), 093901.
- [50] T. Christensen et al. “Nonlocal response of metallic nanospheres probed by light, electrons, and atoms”. *ACS Nano* 8 (2014), 1745–1758.
- [51] N. A. Mortensen et al. “A generalized non-local optical response theory for plasmonic nanostructures”. *Nature Communications* 5, 3809 (2014).
- [52] Y. Yang et al. “A general theoretical and experimental framework for nanoscale electromagnetism”. *Nature* 576 (2019), 248–252.
- [53] F. Bloch. “Bremsvermögen von Atomen mit mehreren Elektronen”. *Zeitschrift für Physik* 81 (1933), 363–376.
- [54] J. Pitarke et al. “Theory of surface plasmons and surface-plasmon polaritons”. *Reports on Progress in Physics* 70 (2006), 1.
- [55] S. Raza et al. “Nonlocal optical response in metallic nanostructures”. *Journal of Physics: Condensed Matter* 27 (2015), 183204.
- [56] M. Wubs and N. A. Mortensen. “Nonlocal response in plasmonic nanostructures”. *Quantum Plasmonics*. Springer, 2017, 279–302.
- [57] S. Raza et al. “Nonlocal response in thin-film waveguides: loss versus nonlocality and breaking of complementarity”. *Physical Review B* 88 (2013), 115401.
- [58] R. Boidin et al. “Pulsed laser deposited alumina thin films”. *Ceramics International* 42 (2016), 1177–1182.
- [59] K. M. McPeak et al. “Plasmonic Films Can Easily Be Better: Rules and Recipes”. *ACS Photonics* 2 (2015), 326–333.
- [60] R. Méjard et al. “Advanced engineering of single-crystal gold nanoantennas”. *Optical Materials Express* 7 (2017), 1157–1168.
- [61] M. Faraday. “X. The Bakerian Lecture.—Experimental relations of gold (and other metals) to light”. *Philosophical Transactions of the Royal Society of London* (1857), 145–181.
- [62] Y. Xia et al. “Shape-controlled synthesis of metal nanocrystals: simple chemistry meets complex physics?” *Angewandte Chemie International Edition* 48 (2009), 60–103.
- [63] D. M. P. Mingos and J. Broda. *Gold clusters, colloids and nanoparticles I*. Vol. 161. Springer, 2014.
- [64] B. An et al. “Shape/size controlling syntheses, properties and applications of two-dimensional noble metal nanocrystals”. *Frontiers of Chemical Science and Engineering* 10 (2016), 360–382.
- [65] C. Lofton and W. Sigmund. “Mechanisms controlling crystal habits of gold and silver colloids”. *Advanced Functional Materials* 15 (2005), 1197–1208.
- [66] C. Li et al. “Mass synthesis of large, single-crystal Au nanosheets based on a polyol process”. *Advanced Functional Materials* 16 (2006), 83–90.
- [67] J. Xie, J. Y. Lee, and D. I. Wang. “Synthesis of single-crystalline gold nanoplates in aqueous solutions through biomineralization by serum albumin protein”. *The Journal of Physical Chemistry C* 111 (2007), 10226–10232.

- [68] L. Au et al. "Synthesis of gold microplates using bovine serum albumin as a reductant and a stabilizer". *Chemistry—An Asian Journal* 5 (2010), 123–129.
- [69] G. Lin et al. "A simple synthesis method for gold nano- and microplate fabrication using a tree-type multiple-amine head surfactant". *Crystal growth & design* 10 (2010), 1118–1123.
- [70] F. Xu et al. "Facile fabrication of single crystal gold nanoplates with micrometer lateral size". *Colloids and Surfaces A: Physicochemical and Engineering Aspects* 353 (2010), 125–131.
- [71] X. Wu et al. "Single-crystalline gold microplates grown on substrates by solution-phase synthesis". *Crystal Research and Technology* 50 (2015), 595–602.
- [72] E. Krauss et al. "Controlled growth of high-aspect-ratio single-crystalline gold platelets". *Crystal Growth & Design* 18 (2018), 1297–1302.
- [73] R. Tran et al. "Surface energies of elemental crystals". *Scientific Data* 3, 160080 (2016).
- [74] M. Brust et al. "Synthesis of thiol-derivatised gold nanoparticles in a two-phase liquid–liquid system". *Journal of the Chemical Society, Chemical Communications* (1994), 801–802.
- [75] B. Radha and G. Kulkarni. "A real time microscopy study of the growth of giant Au microplates". *Crystal growth & design* 11 (2011), 320–327.
- [76] A. Andryieuski et al. "Direct characterization of plasmonic slot waveguides and nanocouplers". *Nano Letters* 14 (2014), 3925–3929.
- [77] R. Deshpande et al. "Direct characterization of near-field coupling in gap plasmon-based metasurfaces". *Nano Letters* 18 (2018), 6265–6270.
- [78] D. K. Gramotnev and S. I. Bozhevolnyi. "Nanofocusing of electromagnetic radiation". *Nature Photonics* 8 (2014), 13–22.
- [79] H. Li et al. "A universal, rapid method for clean transfer of nanostructures onto various substrates". *ACS Nano* 8 (2014), 6563–6570.
- [80] R. Boyd. *Nonlinear Optics*. Elsevier Science, 2020. ISBN: 9780128110034.
- [81] Y. Shen. *The Principles of Nonlinear Optics*. John Wiley & Sons Inc, 2003. ISBN: 9780471430803.
- [82] N. Bloembergen et al. "Optical second-harmonic generation in reflection from media with inversion symmetry". *Physical Review* 174 (1968), 813.
- [83] P. Guyot-Sionnest, W. Chen, and Y. Shen. "General considerations on optical second-harmonic generation from surfaces and interfaces". *Physical Review B* 33 (1986), 8254.
- [84] P. Franken et al. "Generation of optical harmonics". *Physical Review Letters* 7 (1961), 118.
- [85] R. Terhune, P. Maker, and C. Savage. "Optical harmonic generation in calcite". *Physical Review Letters* 8 (1962), 404.
- [86] F. Brown, R. E. Parks, and A. M. Sleeper. "Nonlinear optical reflection from a metallic boundary". *Physical Review Letters* 14 (1965), 1029.
- [87] M. Sheik-Bahae and M. P. Hasselbeck. "Third-order optical nonlinearities". *Handbook of Optics*. Vol. 4. McGraw-Hill Education, 2000. ISBN: 9780071498920.
- [88] M. Göppert-Mayer. "Über Elementarakte mit zwei Quantensprüngen". *Annalen der Physik* 401 (1931), 273–294.
- [89] W. Kaiser and C. Garrett. "Two-photon excitation in Ca F 2: Eu 2+". *Physical Review Letters* 7 (1961), 229.
- [90] S. S. Jha. "Theory of optical harmonic generation at a metal surface". *Physical Review* 140 (1965), A2020.

- [91] J. Rudnick and E. Stern. “Second-harmonic radiation from metal surfaces”. *Physical Review B* 4 (1971), 4274.
- [92] W. Schaich and A. Liebsch. “Nonretarded hydrodynamic-model calculation of second-harmonic generation at a metal surface”. *Physical Review B* 37 (1988), 6187.
- [93] Y. Zeng et al. “Classical theory for second-harmonic generation from metallic nanoparticles”. *Physical Review B* 79 (2009), 235109.
- [94] C. Ciraci et al. “Second-harmonic generation in metallic nanoparticles: Clarification of the role of the surface”. *Physical Review B* 86 (2012), 115451.
- [95] J. Sipe et al. “Analysis of second-harmonic generation at metal surfaces”. *Physical Review B* 21 (1980), 4389.
- [96] P. Guyot-Sionnest and Y. Shen. “Bulk contribution in surface second-harmonic generation”. *Physical Review B* 38 (1988), 7985.
- [97] Y. Shen. “Optical second harmonic generation at interfaces”. *Annual Review of Physical Chemistry* 40 (1989), 327–350.
- [98] Y. Shen. “Revisiting the basic theory of sum-frequency generation”. *The Journal of Chemical Physics* 153 (2020), 180901.
- [99] D. Koos, V. Shannon, and G. Richmond. “Surface-dipole and electric-quadrupole contributions to anisotropic second-harmonic generation from noble-metal surfaces”. *Physical Review B* 47 (1993), 4730.
- [100] D. Krause, C. W. Teplin, and C. T. Rogers. “Optical surface second harmonic measurements of isotropic thin-film metals: Gold, silver, copper, aluminum, and tantalum”. *Journal of Applied Physics* 96 (2004), 3626–3634.
- [101] F. X. Wang et al. “Surface and bulk contributions to the second-order nonlinear optical response of a gold film”. *Physical Review B* 80 (2009), 233402.
- [102] M. Weber and A. Liebsch. “Density-functional approach to second-harmonic generation at metal surfaces”. *Physical Review B* 35 (1987), 7411.
- [103] A. Liebsch and W. Schaich. “Second-harmonic generation at simple metal surfaces”. *Physical Review B* 40 (1989), 5401.
- [104] T. Luce, W. Hübner, and K. Bennemann. “Theory for the nonlinear optical response at noble-metal surfaces with nonequilibrium electrons”. *Zeitschrift für Physik B Condensed Matter* 102 (1997), 223–232.
- [105] C. Chen, A. R. B. de Castro, and Y. Shen. “Surface-enhanced second-harmonic generation”. *Physical Review Letters* 46 (1981), 145.
- [106] G. Boyd et al. “Local-field enhancement on rough surfaces of metals, semimetals, and semiconductors with the use of optical second-harmonic generation”. *Physical Review B* 30 (1984), 519.
- [107] M. I. Stockman et al. “Enhanced second-harmonic generation by metal surfaces with nanoscale roughness: nanoscale dephasing, depolarization, and correlations”. *Physical Review Letters* 92 (2004), 057402.
- [108] F. X. Wang et al. “Enhancement of bulk-type multipolar second-harmonic generation arising from surface morphology of metals”. *New Journal of Physics* 12 (2010), 063009.
- [109] A. Wokaun et al. “Surface second-harmonic generation from metal island films and microlithographic structures”. *Physical Review B* 24 (1981), 849.
- [110] J. Sipe, D. Moss, and H. Van Driel. “Phenomenological theory of optical second- and third-harmonic generation from cubic centrosymmetric crystals”. *Physical Review B* 35 (1987), 1129.
- [111] T. F. Heinz et al. “Spectroscopy of molecular monolayers by resonant second-harmonic generation”. *Physical Review Letters* 48 (1982), 478.

- [112] H. Tom et al. “Surface studies by optical second-harmonic generation: The adsorption of O₂, CO, and sodium on the Rh (111) surface”. *Physical Review Letters* 52 (1984), 348.
- [113] M. Buck et al. “Second-order nonlinear susceptibilities of surfaces”. *Applied Physics A* 60 (1995), 1–12.
- [114] P.-M. Gassin et al. “How to distinguish various components of the SHG signal recorded from the solid/liquid interface?” *Chemical Physics Letters* 664 (2016), 50–55.
- [115] E. Wong and G. Richmond. “Examination of the surface second harmonic response from noble metal surfaces at infrared wavelengths”. *The Journal of Chemical Physics* 99 (1993), 5500–5507.
- [116] G. Farkas et al. “Wavelength dependence of harmonic generation efficiency at metal surfaces induced by femtosecond Ti: sapphire laser pulses”. *Optics Communications* 132 (1996), 289–294.
- [117] C. Matranga and P. Guyot-Sionnest. “Absolute intensity measurements of the optical second-harmonic response of metals from 0.9 to 2.5 eV”. *The Journal of Chemical Physics* 115 (2001), 9503–9512.
- [118] T. Iwai and G. Mizutani. “Optical second harmonic spectroscopy of a Au (1 0 0) 5 × 20 reconstructed surface”. *Applied Surface Science* 237 (2004), 279–283.
- [119] T. Iwai and G. Mizutani. “Optical second harmonic spectroscopy of reconstructed Au (100) and (111) surfaces”. *Physical Review B* 72 (2005), 233406.
- [120] M. Kauranen and A. V. Zayats. “Nonlinear plasmonics”. *Nature Photonics* 6 (2012), 737–748.
- [121] A. Boardman and A. Zayats. “Nonlinear plasmonics”. *Handbook of Surface Science*. Vol. 4. Elsevier, 2014, 329–347. ISBN: 9780444595263.
- [122] J. Butet, P.-F. Brevet, and O. J. Martin. “Optical second harmonic generation in plasmonic nanostructures: from fundamental principles to advanced applications”. *ACS Nano* 9 (2015), 10545–10562.
- [123] P. Dombi et al. “Strong-field nano-optics”. *Reviews of Modern Physics* 92 (2020), 025003.
- [124] R. W. Boyd, Z. Shi, and I. De Leon. “The third-order nonlinear optical susceptibility of gold”. *Optics Communications* 326 (2014), 74–79.
- [125] M. Sheik-Bahae et al. “Sensitive measurement of optical nonlinearities using a single beam”. *IEEE Journal of Quantum Electronics* 26 (1990), 760–769.
- [126] N. Bloembergen, W. Burns, and M. Matsuoka. “Reflected third harmonic generated by picosecond laser pulses”. *Optics Communications* 1 (1969), 195–198.
- [127] M. Guerrisi, R. Rosei, and P. Winsemius. “Splitting of the interband absorption edge in Au”. *Physical Review B* 12 (1975), 557.
- [128] M. R. Beversluis, A. Bouhelier, and L. Novotny. “Continuum generation from single gold nanostructures through near-field mediated intraband transitions”. *Physical Review B* 68 (2003), 115433.
- [129] P. Biagioni et al. “Dependence of the two-photon photoluminescence yield of gold nanostructures on the laser pulse duration”. *Physical Review B* 80 (2009), 045411.
- [130] P. Biagioni et al. “Dynamics of four-photon photoluminescence in gold nanoantennas”. *Nano Letters* 12 (2012), 2941–2947.
- [131] K. Imura, T. Nagahara, and H. Okamoto. “Near-field two-photon-induced photoluminescence from single gold nanorods and imaging of plasmon modes”. *The Journal of Physical Chemistry B* 109 (2005), 13214–13220.
- [132] C.-K. Sun et al. “Femtosecond-tunable measurement of electron thermalization in gold”. *Physical Review B* 50 (1994), 15337.

- [133] C. Guo, G. Rodriguez, and A. J. Taylor. “Ultrafast dynamics of electron thermalization in gold”. *Physical Review Letters* 86 (2001), 1638.
- [134] P. N. Melentiev et al. “Giant enhancement of two photon induced luminescence in metal nanostructure”. *Optics Express* 23 (2015), 11444–11452.
- [135] H. Petek et al. “Optical phase control of coherent electron dynamics in metals”. *Physical Review Letters* 79 (1997), 4649.
- [136] G. Boyd, Z. Yu, and Y. Shen. “Photoinduced luminescence from the noble metals and its enhancement on roughened surfaces”. *Physical Review B* 33 (1986), 7923.
- [137] P. Bharadwaj, B. Deutsch, and L. Novotny. “Optical antennas”. *Advances in Optics and Photonics* 1 (2009), 438–483.
- [138] P. Muehlschlegel et al. “Resonant optical antennas”. *Science* 308 (2005), 1607–1609.
- [139] X.-F. Jiang et al. “Excitation nature of two-photon photoluminescence of gold nanorods and coupled gold nanoparticles studied by two-pulse emission modulation spectroscopy”. *The Journal of Physical Chemistry Letters* 4 (2013), 1634–1638.
- [140] A. Mooradian. “Photoluminescence of metals”. *Physical Review Letters* 22 (1969), 185.
- [141] V. Knittel et al. “Nonlinear photoluminescence spectrum of single gold nanostructures”. *ACS Nano* 9 (2015), 894–900.
- [142] C. Molinaro et al. “Two-photon luminescence of single colloidal gold nanorods: revealing the origin of plasmon relaxation in small nanocrystals”. *The Journal of Physical Chemistry C* 120 (2016), 23136–23143.
- [143] E. Sakat et al. “Time-resolved photoluminescence in gold nanoantennas”. *ACS Photonics* 3 (2016), 1489–1493.
- [144] A. Bouhelier, M. R. Beversluis, and L. Novotny. “Characterization of nanoplasmonic structures by locally excited photoluminescence”. *Applied Physics Letters* 83 (2003), 5041–5043.
- [145] J. Beermann and S. I. Bozhevolnyi. “Two-photon luminescence microscopy of field enhancement at gold nanoparticles”. *Physica Status Solidi (c)* 2 (2005), 3983–3987.
- [146] K. Imura, T. Nagahara, and H. Okamoto. “Photoluminescence from gold nanoplates induced by near-field two-photon absorption”. *Applied Physics Letters* 88 (2006), 023104.
- [147] P. Ghenuche, S. Cherukulappurath, and R. Quidant. “Mode mapping of plasmonic stars using TPL microscopy”. *New Journal of Physics* 10 (2008), 105013.
- [148] J.-S. Huang et al. “Mode imaging and selection in strongly coupled nanoantennas”. *Nano Letters* 10 (2010), 2105–2110.
- [149] N. Verellen et al. “Two-photon luminescence of gold nanorods mediated by higher order plasmon modes”. *ACS Photonics* 2 (2015), 410–416.
- [150] V. Knittel. “Ultrafast nonlinear response of plasmonic nanoantennas”. PhD thesis. 2018.
- [151] V. Knittel et al. “Dispersion of the nonlinear susceptibility in gold nanoantennas”. *Physical Review B* 96 (2017), 125428.
- [152] R. Mejjard et al. “Energy-resolved hot-carrier relaxation dynamics in monocrystalline plasmonic nanoantennas”. *ACS Photonics* 3 (2016), 1482–1488.
- [153] R. Trebino. *Frequency-resolved optical gating: the measurement of ultrashort laser pulses*. Springer Science & Business Media, 2012. ISBN: 9781461511816.
- [154] A. Hohenau et al. “Spectroscopy and nonlinear microscopy of Au nanoparticle arrays: Experiment and theory”. *Physical Review B* 73 (2006), 155404.

A Interference in edge-scattering from monocrystalline gold flakes



Interference in edge-scattering from monocrystalline gold flakes [Invited]

SERGEJS BOROVIKS,¹ CHRISTIAN WOLFF,¹ JES LINNET,¹
YUANQING YANG,¹ FRANCESCO TODISCO,¹
ALEXANDER S. ROBERTS,¹ SERGEY I. BOZHEVOLNYI,^{1,2} BERT
HECHT,³ AND N. ASGER MORTENSEN^{1,2,*}

¹Center for Nano Optics, University of Southern Denmark, Campusvej 55, DK-5230 Odense M, Denmark

²Danish Institute for Advanced Study, University of Southern Denmark, Campusvej 55, DK-5230 Odense M, Denmark

³Nano-Optics and Biophotonics Group, Experimentelle Physik 5, Physikalisches Institut, Wilhelm-Conrad-Röntgen-Center for Complex Material Systems, Universität Würzburg, Würzburg, Germany

*asger@mailaps.org

Abstract: We observe strongly dissimilar scattering from the two types of sidewall configurations (here referred to as "edges") in hexagonal quasi-monocrystalline gold flakes with thicknesses around 1 micron. As the origin of the phenomena, we identify the interference between a direct, quasi-specular scattering and an indirect scattering process involving an intermediate surface-plasmon state. The dissimilarity between the two types of edges is a direct consequence of the three-fold symmetry around the [111]-axis and the intrinsic chirality of a face-centered cubic lattice. We propose that this effect can be potentially used to estimate dielectric function of the monocrystalline gold.

© 2018 Optical Society of America under the terms of the [OSA Open Access Publishing Agreement](#)

1. Introduction

Historically, the field of plasmonics [1] has explored the interaction of light with the free electron gas, with a predominant attention to amorphous and polycrystalline noble metal nanostructures and thin films, [2] while less attention has been devoted to plasmons supported by monocrystalline materials. More recently, chemically synthesized monocrystalline gold flakes have been receiving increasing attention within the plasmonic community. In many aspects, such colloidal gold nanoparticles show superior plasmonic properties, as compared to evaporated polycrystalline films. [3–6] Atomic flatness and well-defined crystal structure offer larger plasmon propagation lengths and sharper resonances due to lower Ohmic losses and reduced surface scattering. [7] These favorable properties have been utilized in the design and fabrication of various plasmonic devices, such as nano-circuits, [3, 8] nano-antennas, [9–11] tapers, [12] and plasmon billiards. [13, 14] However, flat metal crystals are rarely true single crystals, but rather twins joined at pairs of stacking faults. [15] This is no coincidence, because the strong lateral growth involving {100}-facets requires the presence of at least 2 stacking faults within the seed. [6] These defects play an important role in the crystal growth [5] and might exhibit interesting plasmonic phenomena of electronic 2D states. This, along with the well defined material properties of single crystals, renders them excellent candidates for the observation of quantum effects, [16, 17] or of anisotropic nonlinear or nonlocal response e.g. due to the deviation of the Fermi surface from a perfect sphere. This is especially true for sub-micron particles, as quantum corrections to the classical electrodynamics manifest increasingly when approaching the subwavelength scale and reaching the atomic dimensions. [18, 19]

Differences between the material properties of mono- and polycrystalline metals are both important for applications as well as interesting in their own right. Moreover, the highly ordered

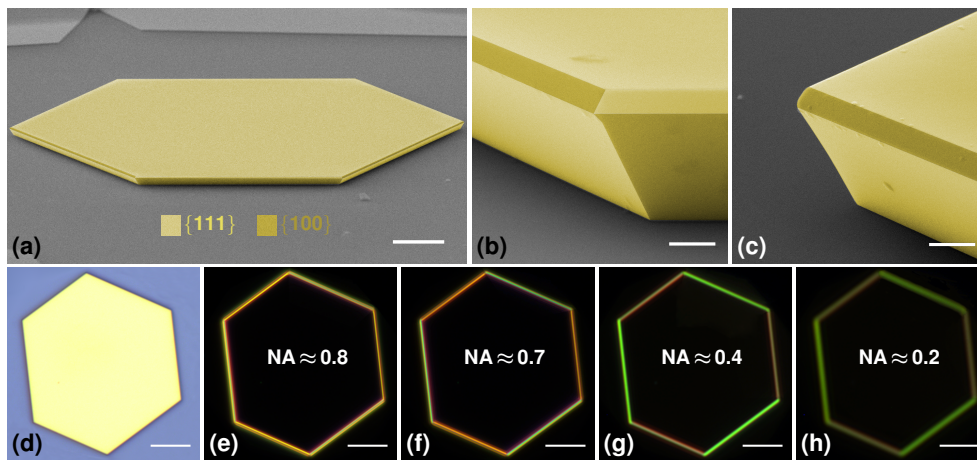


Fig. 1. (a) SEM image of the Au monocrystalline flake (75° tilted view, scale bar: $10\ \mu\text{m}$); (b) and (c) close-up high resolution SEM images of the two corners of the flake (75° tilted view, scale bars: $500\ \text{nm}$). Artificial coloration is used to highlight different crystallographic planes of the facets: light yellow for $\{111\}$ and dark yellow for $\{100\}$. (d) Bright-field and (e)-(h) dark-field optical images of the flake captured with 4 different NA's, indicated in the images (scale bars: $10\ \mu\text{m}$).

atomic structure of single crystals is also reflected in their geometry with very well defined angles, atomically flat surfaces and sharp edges. The quality of these features is well beyond what is currently achievable with state-of-the-art nano-patterning of polycrystalline films, [20] and they provide valuable material for the basic research of nanoplasmonics in finite-size metal geometries e.g. on the propagation of surface-plasmon polaritons (SPP) along the edges of gold crystals. [21, 22] Several examples for such studies have been conducted for particles that are small compared to the wavelength of light. [23–26]

Crystal-related morphologic features are of course by no means restricted to subwavelength-sized particles, but also appear in fairly large objects such as the gold flakes studied in this paper with lateral dimensions greater than $10\ \mu\text{m}$ and thicknesses around $1\ \mu\text{m}$. One such non-trivial feature is the fact that the sidewalls (for convenience referred to as "edges") of our nearly hexagonal flakes are asymmetrically tapered and that two types of such edge terminations alternate around the flake. As a result, each edge is dissimilar to both adjacent edges and the opposing one. This lack of symmetry with respect to mirroring and 180° rotation can be seen in high-resolution scanning-electron microscope (SEM) images (Fig. 1(a)-(c)). Yet quite often, this detail is ignored and the edges are simply approximated as rectangular truncations [21, 22]. However, it reflects the fact that the face-centered cubic (FCC) gold lattice is symmetric with respect to neither a 180° -rotation nor a mirror operation about the $[111]$ -axis. It is therefore a large-scale manifestation of the atomic order and can lead to a significant difference in the optical far-field properties as we show here.

In this work we report on a distinct difference in the scattering of visible light from the two types of edge terminations of colloiddally grown gold flakes with thicknesses around one micron. Even though in an optical bright-field (BF) our flake looks perfectly hexagonal (Fig. 1(d)) and seemingly exhibits six fold symmetry, difference in scattering appears as differently colored edges when observed in an optical dark-field (DF) microscope under lower numerical aperture (NA) collection conditions (see Fig. 1(e)-(h)). We conclude that this is the far-field manifestation

of the fact that opposing flake edges make different angles with the substrate, which in turn is a macroscopic consequence of the inherent chirality along the $[111]$ -axis of the FCC lattice.

2. Results and discussion

We grew quasi-monocrystalline gold flakes on a silicon wafer substrates from chloroauric acid in the modified Brust–Schiffrin method [27] involving thermolysis of the precursor instead of chemical reduction (see Methods section for further details). This is known to yield flakes, which are large [28] and feature hexagonal, triangular and truncated triangular shapes with high aspect ratios up to 100. We obtain lateral sizes of up to 100 microns with thicknesses between several dozen nanometers and few microns. From the symmetries of the FCC gold lattice, one would expect the crystals to be bounded by facets of $\{111\}$ - and $\{100\}$ -types with threefold and fourfold symmetries, respectively. This is illustrated in Fig. 1(a)-(c), which show SEM images with artificial colorization indicating crystal planes of the corresponding facets. Therefore, it seems safe to assume the large top and bottom faces to be of $\{111\}$ -type. [5] As a result, each of the three or six edges of the flakes is composed of one $\{111\}$ - and one $\{100\}$ -type facet, which meet at an angle of $\approx 125.3^\circ$ and make angles $\alpha = \arccos(1/\sqrt{3}) \approx 54.7^\circ$ and $\beta = \arccos(1/3) \approx 70.5^\circ$ with the central plane, respectively. Consequently, the cross sections of the flakes consist of an upper and a lower trapezoids with different heights h_u and h_l , but fixed angles, as illustrated in Fig. 2.

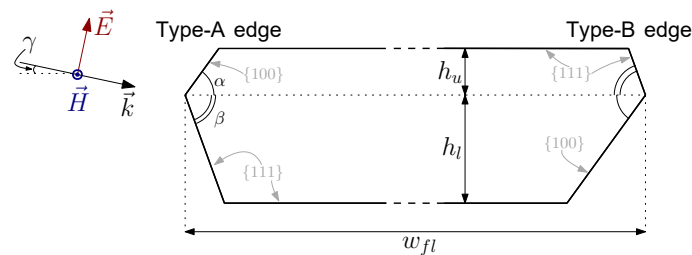


Fig. 2. Schematic drawing of the flake's cross-section (cut trough two opposite edges) with indicated geometrical parameters and Miller indices of the the facets.

The strong imbalance in the size of the top and bottom $\{111\}$ -planes over all others is due to stacking faults (more precisely multiple twin planes), which form in the early stage of the crystal growth. Such defects commonly appear in the metals with FCC crystal structure, especially in gold, as they have some of the lowest defect energies [29]. They lead to quite different growth rates along different crystal axes and thus cause high aspect ratio of the crystals. Therefore, such thin flakes are not strictly speaking monocrystalline, as commonly referred to, but twins.

It is noteworthy that the FCC-lattice has only three-fold symmetry in the $\{111\}$ -plane even though such a crystal facet might be perfectly hexagonal, as one shown in Fig. 1(d). This is the result of the chirality of the FCC-lattice along the $[111]$ -axis, which is due to the existence of two different stacking patterns. Macroscopically, it manifests in the aforementioned two types of flake edges, which appear with threefold symmetry. In the following, we refer to edges where the side facet touching the substrate is of $\{111\}$ -type or $\{100\}$ -type as type-A or type-B edges, respectively. As it turns out, this three-fold symmetry and therefore the lattice chirality can be directly observed with an optical microscope.

We noticed that flakes which look almost perfectly hexagonal in the optical bright-field and high-NA dark-field (Fig. 1(d),(e)) exhibit very different scattering spectra from the two types of edges. This is visible to the naked eye under DF conditions and becomes more prominent

with decreasing collection NA, as shown in Fig. 1(f)-(h). Images were acquired using the same objective lens and the same illumination conditions (light from DF condenser impinging on the sample at a grazing angle $\gamma \approx 12^\circ$), and filtering the collected light in the Fourier plane, as described in details in the Methods section.

We find behavior that is qualitatively similar to that depicted here, yet with different shades of red, yellow and green commonly for flakes with thicknesses around 1 micron, so it appears to be a geometry-related effect. In order to further understand the underlying process, we first performed 2D finite-element calculations in p-polarization. This is sufficient for qualitative results, because we observed experimentally that with polarized illumination only the edges perpendicular to the incident polarization appear in dark-field and that the scattered light is p-polarized itself. We then post-processed the data with a far-field filtering procedure that mimics the effect of a low-NA objective (see Methods section for further details). Figure 3 shows experimental spectra acquired with $NA \approx 0.4$, which provides good contrast while keeping sufficiently strong signal, for two adjacent edges of the flake shown in Fig. 1. Alongside is shown a numerical spectrum calculated using nominal dimensions ($h_u = 130$ nm and $h_l = 580$ nm, as measured on the real flake), idealized illumination conditions and the permittivity of monocrystalline gold given by interpolated experimental data from Olmon [30]. Although we clearly do not obtain quantitative agreement, the experimental and numerical results show the same qualitative features: a peak for the type-A edge surrounded by troughs and a similar behavior for the type-B edge red-shifted by some 100 nm. We postpone the discussion of possible origins for this mismatch and first focus on the physical mechanism. However, we do emphasize at this point that the spectra of different flakes differ significantly in the positions of peaks and troughs, but always show the general features of an interference pattern.

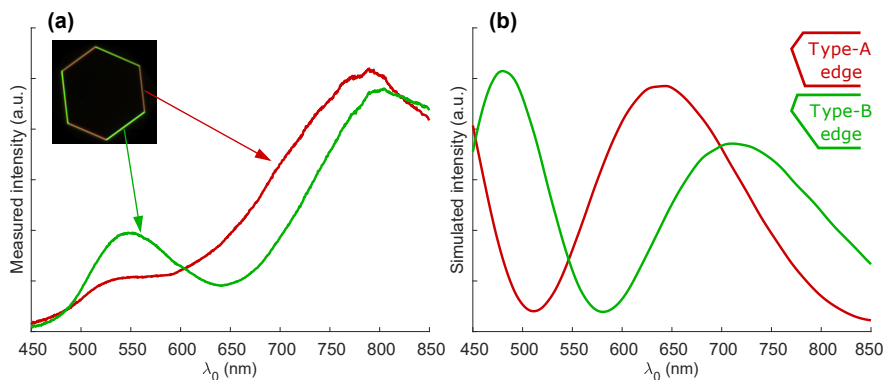


Fig. 3. (a) Experimental and (b) simulated DF spectra of the two types of edges of the flake with nominal dimensions $h_u = 130$ nm and $h_l = 580$ nm. Both experimental and simulated spectra are acquired with $NA = 0.4$.

The physical origin of the different scattering spectra of the type-A and the type-B edges is the interference between a surface-plasmon wave and free-space propagation of light, which we concluded from a careful analysis of the numerical simulations, especially for varying values of the flake thickness parameters h_u and h_l . We observe that light scattered directly into a low-NA objective stems predominantly from the upper facet (characterized by h_u), while the direct scattering from the lower facet is directed predominantly downwards, as one would expect from geometric optics or basic diffraction theory. Varying the parameter h_u in our calculations caused broad-band changes to the scattering efficiency while leaving the beating period virtually

unchanged. The upper edge appears to act as an effective point-like dipole. This holds true in simulations even if $h_u \approx h_l$. In contrast, varying h_l mainly changed the beating period and strongly shifted the peaks, so the resonances are linked to the length of the lower facet. Standing waves on that facet were considered, but did not match the observed beating period. As the illumination both in the experiment and the simulation is essentially at the Brewster angle for an air/silicon interface, light reflected from the substrate also does not enter the picture. Although the light scattered by the edge downwards hits the substrate at a different angle and might participate in the interference, we anticipate it as a weak effect.

This leads to the following explanation: the light emanating from the upper facet has two main contributions. Firstly, the scattered light is coming from direct illumination of the upper facet (blue arrow in Fig. 4(a)). However, there is also a second, indirect path illustrated by red arrows in Fig. 4. Like every metallic surface discontinuity, the lower corner of the crystal couples incident light to SPP. The resulting SPP travels up the facet, where it couples out to the far-field and contributes to the scattered radiation. Depending on the phase accumulated in this process, the direct and indirect radiation interfere constructively or destructively in the far-field, leading to a scattering spectrum that depends sensitively on h_l , the edge type, the grazing angle γ , the collection NA and the SPP dispersion relation. The in-coupling of the secondary path is significantly enhanced by the presence of a high-index substrate – with low-index substrates the effect is much less prominent, as we observed both experimentally and in simulations.

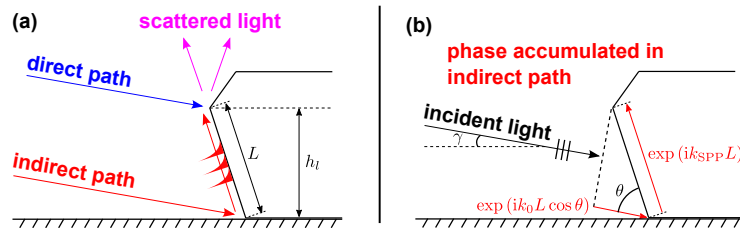


Fig. 4. Schematics of the enhanced-scattering mechanism. (a) The dark-field illumination has two possible paths to scatter upwards into the objective: a direct path is the quasi-specular reflection at the upper facet; an additional indirect path is by coupling to a surface wave at the lowest corner, travelling along the lower facet and coupling out at the upper facet. (b) The indirect path is delayed with respect to the direct path by a phase that depends on thickness of the lower flake part and on the angle θ , included by the direction of grazing illumination and the lower facet. This leads to a distinct interference effect in the far-field.

The phase difference between the direct and the indirect path is sketched in Fig. 4(b). The sample is illuminated by the DF objective under a grazing angle $\gamma \approx 12^\circ$, which means that the illumination light impinges the lower flake facet at an angle $\theta = \beta - \gamma$ or $\theta = \alpha - \gamma$ for type-A and type-B edges, respectively. As a result, the upper and the lower corners of the edge are excited with a phase difference $\Phi_1 = \exp(ik_0 L \cos \theta)$, where k_0 is the vacuum wave number of the light and L is the length of the facet, i.e. $L = h_l / \sin \beta$ or $L = h_l / \sin \alpha$ for type-A and type-B edges, respectively. Afterwards, the indirect path gains an additional phase $\Phi_2 = \exp(ik_{SPP} L)$ while traveling along the facet, where k_{SPP} is the wave number of the SPP. Thus, the total phase difference between the direct and the indirect path (excluding other phase contributions from additional processes such as standing waves on the lower facet, nonzero SPP excitation phase at the lower corner and scattering phase at the upper facet that are different from the incident

wave's phase) is

$$\Delta\Phi = \exp[i(k_{\text{SPP}} + k_0 \cos \theta)L] \quad (1)$$

and we expect that the scattering spectra of either edge type depend periodically on the parameter h_l with a periodicity of

$$\Delta h_l^{(A)} = \frac{2\pi \sin \beta}{k_{\text{SPP}} + k_0 \cos(\gamma - \beta)} \quad (2)$$

for the type-A edge and with α instead of β for the type-B edge. Using the permittivity $\epsilon_{\text{Au}} = -16 + 1.1i$ for monocrystalline gold [30] at a vacuum wavelength of $\lambda_0 = 700$ nm as an example, and assuming $\gamma = 12^\circ$, we find:

$$\Delta h_l^{(A)} \approx 420 \text{ nm} \quad \text{and} \quad \Delta h_l^{(B)} \approx 320 \text{ nm}.$$

This means that we expect the scattering intensity observed at type-A or type-B edges to exhibit interference oscillations with the periods of 420 nm or 320 nm, respectively, when h_l parameter is varied.

These values for the periodicity are to be compared to the numerically simulated spectra in the Fig. 5, where the upwards scattered power for both types of edges at a fixed wavelength (700 nm) is plotted as a function of the lower flake thickness h_l with all other parameters (e.g. γ , h_u , etc.) kept as in Fig. 3. We observe distinct oscillations with a periodicity of ≈ 340 nm for type-B edges, which is in good agreement with the simple interference model. The periodicity of the type-A spectra is slightly less consistent as the spectrum is not a pure sinusoid (distances between minima, maxima and turning points give different "periodicities"). Anyhow, the periodicity is greater than for type-B edges and we extract a value of ≈ 380 nm. This is still in qualitative agreement with the interference model. We attribute the disparity to the existence of a second, weaker resonant effect, potentially a Fabry-Pérot-like standing wave on the lower facet. Yet, the main effect is clearly visible, especially since no alternative explanation predicts oscillations in the 300–400 nm range.

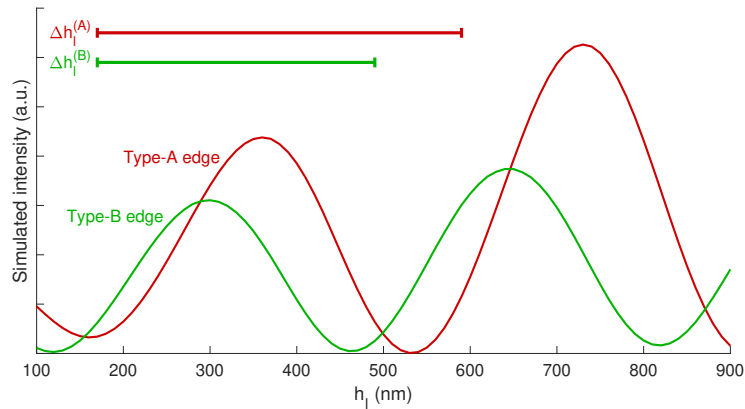


Fig. 5. Simulated scattering intensity at $\lambda_0 = 700$ nm for the two types of edges with $h_u = 130$ nm and range of h_l values. Estimated periodicity of the oscillations are ≈ 380 nm for the type-A and ≈ 340 nm for the type-B edge. The horizontal lines show the estimates for $\Delta h_l^{(A)} \approx 420$ nm and $\Delta h_l^{(B)} \approx 320$ nm, according to Eq. (2).

So far, we have not discussed the agreement between experimental and numerical spectra (Fig. 3). Both panels show qualitatively similar behavior. The most striking differences are an overall red-shift by some 100 nm of all features in the experimental spectrum and a significantly reduced amplitude towards the blue spectral range. This is partially due to simplifications and uncertainties in the numerical model. Firstly, in our simulations we choose a 2D finite-element model with plane-wave illumination impinging normally on the edge. In contrast, the illumination in our dark-field experiment is from a range of azimuthal angles covering a sector of 60° . We expect that non-normal incidence would lead to considerable red-shift of the interference effect. Secondly, also the angle of grazing illumination in the experiment is not well defined. Illumination light arrives at the edge from an indefinite range of grazing angles around approximately 12° . In the numerical model, we assume a plane wave from a grazing angle $\gamma = 12^\circ$. These two angular distributions lead to a smearing and potentially to a partial destruction of the interference pattern, especially at higher orders, i.e. shorter wavelength. Thirdly, we have conducted simulations with different common models for the permittivity of gold and found that variations in the plasmon dispersion relation can easily account for 50 nm shift in the spectral features, too. Finally, even though the flakes appear clean in the SEM micrographs, we suspect that the flake is covered by residue from the fabrication process, which again would lead to spectral red-shift and potentially to increased loss at shorter wavelengths.

The dependence of the observed edge color (and hence measured spectra) on the collection NA, which is clearly visible in Fig. 1(e)-(h), was also observed in the numerical simulations: interference peaks become wider and less prominent with the increasing value of NA in the above-mentioned post-processing filter. However, the effect is not as pronounced as in the experiment, presumably due to the idealized illumination conditions in the simulations. This behavior also fits well with the analytical model: directionality of the interferential scattering (that manifests in collection NA-dependent apparent edge colors) is expected due to quasi-specular reflection in the direct path, and it should become more prominent with the increasing distribution of the illumination angles.

Within the limits of these uncertainties, we are confident that we have identified the main origin for the thickness-dependent dissimilar scattering spectra from type-A and type-B edges in quasi-monocrystalline gold flakes.

3. Methods

In the following subsections experimental and numerical methods used in this work are described.

3.1. Sample preparation

Gold monocrystalline flakes were prepared using the modified Brust–Schiffrin [27] method for colloidal gold synthesis in a two-phase liquid-liquid system via thermolysis [28]. In this method, an aqueous solution of the chloroauric acid ($\text{HAuCl}_4 \cdot 3 \text{H}_2\text{O}$) in concentration 0.5 g mol^{-1} is used as the precursor. It is mixed with a solution of tetraoctylammonium bromide (TOABr) in toluene in a vial and stirred using a magnetic stirrer for approximately 10 minutes at 5000 RPM. During this process AuCl_4^- ions are transferred from aqueous solution to the toluene and TOABr acts as a phase transfer catalyst. After that the mixture is left in rest for approximately 10 minutes, during which two phases – aqueous and organic – separate. The substrate (n-type Si wafer) is prepared: a piece of silicon wafer is pre-cleaned using ultrasonic bath in acetone, isopropyl alcohol (IPA) and ultrapure water (Milli-Q). After drying with nitrogen gas the substrate is pre-baked on a hot plate at 200°C for approximately 5 minutes for dehydration purposes. In the following step few microlitres of the organic phase are drop-casted onto a substrate which is then kept on the hot-plate at 160°C for 30 minutes. After that the sample is cleaned in toluene at 75°C temperature, acetone and IPA, which removes the greater part of the organic solvent. After the sample is dried with a mild nitrogen blow, a large number and variety of gold flakes are found on

the surface of the substrate.

3.2. Spectroscopy

DF spectroscopy measurements were performed using the Zeiss Observer microscope (Epiplan-Neofluar HD objective 50x, NA=0.80) and Andor Kymera 193i spectrograph equipped with Andor Newton CCD camera. Additionally, two lenses (achromatic doublets with focal lengths 15 and 20 cm) and an iris diaphragm were used to create the so-called 4f correlator system for spatial filtering (i.e. NA selection). For the measurements described in this work we have calibrated diaphragm opening to correspond to $NA \approx 0.4$. This value of the collection NA was chosen because it gives good contrast between two types of edges, while keeping sufficiently strong signal and high spatial resolution. Lenses with different focal lengths were chosen intentionally to obtain appropriate image magnification on the camera screen.

A standard tungsten-halogen lamp was used as an illumination unit in this setup. In order to achieve "one-sided" illumination, the DF mirror cube was modified to restrict the range of azimuthal angles of incidence, i.e. DF illumination ring was partially covered with an opaque sheet and only a sector of $\approx 60^\circ$ was left open. Reported spectra were normalized to a reference spectrum, obtained by illuminating a white scatterer in the same conditions.

Additionally, a linear polarizer and analyzer were used to select appropriate polarization of the illumination and detected light (i.e. p-polarization for the specified edge of the flake).

In order to avoid any systematic error due to the experimental setup, we measured different edges by rotating the sample while keeping fixed all other settings.

3.3. Numerical simulations

Numerical simulations were performed in the frequency domain using a commercially available finite-element method (FEM) solver (Comsol Multiphysics 5.3). The geometry of the model is two-dimensional, implying homogeneity along z -axis direction (axis orthogonal to the plane of the flake's cross-section). We consider this simplification to be appropriate as lateral dimensions of the flake are much larger than the thickness (i.e. $w_{fl} \gg h_u + h_l$). The model assumes a plane wave with wavelength λ_0 at a grazing angle γ . In the first step, the model solves for the electric field distribution in the vicinity of the air/silicon interface. For the refractive index of Si, we used interpolated experimental data by Aspens [31]. In the second step, a gold particle is placed on the substrate with the shape shown in Fig. 2 and fields calculated in the first step are used as a background source to obtain the scattered fields. The refractive index of monocrystalline gold is described by interpolated experimental data from Olmon [30]. The model uses triangular meshing (5 nm maximum element size in the metal domain, 8 nm in silicon) and fourth order polynomial basis functions. We have performed mesh refinement study, from which we assess second order convergence and estimate relative error in the reported numerical data to be less than one percent.

In the subsequent step, the simulated fields were post processed using a dedicated filtering method, which mimics operation of the microscope objective, i.e. selects only traveling waves which propagate within a given NA.

4. Conclusions

To summarize, in this work we have exemplified that the differences in the scattering spectra of the adjacent edges of the gold monocrystalline flakes, which we have first observed experimentally in the DF microscope, are far-field manifestation of the subwavelength-scale morphological features. We have developed a numerical model and filtering method which allows to simulate the experimental conditions fairly accurately. Through a careful analysis of numerical simulations, we have found that the height of the lower trapezoid in the cross-section of the flake (h_l) is the main parameter for determination of the scattering spectrum. Guided by analysis of numerical

results, we have developed an analytical model where the physical mechanism, which gives the main contribution to the observed scattering spectrum, is the interference between a surface plasmon in the lower facet of the flake's edge and free space waves. The difference in the lengths of the facets of adjacent and opposite edges explains the difference in scattering spectra of those.

Finally, we speculate that the strong sensitivity to the plasmon dispersion relation in the described effect offers a possibility to estimate permittivity function of the monocrystalline gold flakes, provided they are known to be clean. Given that the flakes have well-determined geometries, and with possibilities for high resolution measurement of the length scales, simulations can be matched with the experimental spectra using permittivity as the fitting parameter. However, we emphasize that perfect matching can only be achieved with virtually plane wave-like illumination, which implies substantially improved control over the sample illumination e.g. by using a goniometer.

Author contributions

S. B. contributed to materials synthesis, sample fabrication, structural characterization, optical measurements, and simulations. J. L. contributed to materials synthesis and structural characterization. C. W. contributed the theory, modeling, and simulations. Y.Y. contributed to materials synthesis. F. T. contributed to optical microscopy and measurements. A. S. R. contributed to the optical microscopy and structural characterization. B. H. introduced materials synthesis and initial materials. The project was supervised by C. W., S. I. B., and N. A. M. All authors participated in the interpretation of results and the writing of the manuscript.

Funding

Marie Skłodowska-Curie COFUND Action (grant agreement No. 713694); European Research Council (grant 341054, PLAQNAP); VILLUM FONDEN (grant 16498); University of Southern Denmark (SDU 2020 funding).

Acknowledgments

We thank C. Tserkezis and J.-S. Huang for stimulating discussions, and P. Trimby (Oxford Instruments) for experimental assistance characterizing the crystal directions of the gold flakes. Simulations were supported by the DeIC National HPC Centre, SDU.

References

1. A. I. Fernández-Domínguez, F. J. García-Vidal, and L. Martín-Moreno, "Unrelenting plasmons," *Nat. Photon.* **11**, 8–10 (2017).
2. K. M. McPeak, S. V. Jayanti, S. J. P. Kress, S. Meyer, S. Iotti, A. Rossinelli, and D. J. Norris, "Plasmonic films can easily be better: Rules and recipes," *ACS Photonics* **2**, 326–333 (2015).
3. J.-S. Huang, V. Callegari, P. Geisler, C. Brüning, J. Kern, J. C. Prangma, X. Wu, T. Feichtner, J. Ziegler, P. Weinmann, M. Kamp, A. Forchel, P. Biagioni, U. Sennhauser, and B. Hecht, "Atomically flat single-crystalline gold nanostructures for plasmonic nanocircuitry," *Nat. Commun.* **1**, 150 (2010).
4. X. Wu, R. Kullock, E. Krauss, and B. Hecht, "Single-crystalline gold microplates grown on substrates by solution-phase synthesis," *Cryst. Res. Technol.* **50**, 595–602 (2015).
5. B. Hoffmann, M. Y. Bashouti, T. Feichtner, M. Mačković, C. Dieker, A. M. Salaheldin, P. Richter, O. D. Gordan, D. R. T. Zahn, E. Spiecker, and S. Christiansen, "New insights into colloidal gold flakes: structural investigation, micro-ellipsometry and thinning procedure towards ultrathin monocrystalline layers," *Nanoscale* **8**, 4529–4536 (2016).
6. E. Krauss, R. Kullock, X. Wu, P. Geisler, N. Lundt, M. Kamp, and B. Hecht, "Controlled growth of high-aspect-ratio single-crystalline gold platelets," *Cryst. Growth & Des.* **18**, 1297–1302 (2018).
7. R. Méjard, A. Verdy, O. Demichel, M. Petit, L. Markey, F. Herbst, R. Chassagnon, G. C. des Francs, B. Cluzel, and A. Bouhelier, "Advanced engineering of single-crystal gold nanoantennas," *Opt. Mater. Express* **7**, 1157–1168 (2017).
8. W.-H. Dai, F.-C. Lin, C.-B. Huang, and J.-S. Huang, "Mode conversion in high-definition plasmonic optical nanocircuits," *Nano Lett.* **14**, 3881–3886 (2014).

9. J. C. Prangsma, J. Kern, A. G. Knapp, S. Grossmann, M. Emmerling, M. Kamp, and B. Hecht, "Electrically connected resonant optical antennas," *Nano Lett.* **12**, 3915–3919 (2012).
10. W.-L. Chen, F.-C. Lin, Y.-Y. Lee, F.-C. Li, Y.-M. Chang, and J.-S. Huang, "The modulation effect of transverse, antibonding, and higher-order longitudinal modes on the two-photon photoluminescence of gold plasmonic nanoantennas," *ACS Nano* **8**, 9053–9062 (2014).
11. J. Kern, R. Kullock, J. Prangsma, M. Emmerling, M. Kamp, and B. Hecht, "Electrically driven optical antennas," *Nat. Photon.* **9**, 582 (2015).
12. S. Schmidt, B. Piglosiewicz, D. Sadiq, J. Shirdel, J. S. Lee, P. Vasa, N. Park, D.-S. Kim, and C. Lienau, "Adiabatic nanofocusing on ultrasmooth single-crystalline gold tapers creates a 10-nm-sized light source with few-cycle time resolution," *ACS Nano* **6**, 6040–6048 (2012).
13. G. Spektor, D. Kilbane, A. K. Mahro, B. Frank, S. Ristok, L. Gal, P. Kahl, D. Podbiel, S. Mathias, H. Giessen, F. J. Meyer zu Heringdorf, M. Orenstein, and M. Aeschlimann, "Revealing the subfemtosecond dynamics of orbital angular momentum in nanoplasmonic vortices," *Science* **355**, 1187–1191 (2017).
14. B. Frank, P. Kahl, D. Podbiel, G. Spektor, M. Orenstein, L. Fu, T. Weiss, M. Horn-von Hoegen, T. J. Davis, F.-J. Meyer zu Heringdorf, and H. Giessen, "Short-range surface plasmonics: Localized electron emission dynamics from a 60-nm spot on an atomically flat single-crystalline gold surface," *Sci. Adv.* **3**, e1700721 (2017).
15. C. Lofton and W. Sigmund, "Mechanisms controlling crystal habits of gold and silver colloids," *Adv. Func. Mater.* **15**, 1197–1208 (2005).
16. K. Ding and C. T. Chan, "Plasmonic modes of polygonal rods calculated using a quantum hydrodynamics method," *Phys. Rev. B* **96**, 125134 (2017).
17. A. Cuche, M. Berthel, U. Kumar, G. Colas des Francs, S. Huant, E. Dujardin, C. Girard, and A. Drezet, "Near-field hyperspectral quantum probing of multimodal plasmonic resonators," *Phys. Rev. B* **95**, 121402 (2017).
18. S. I. Bozhevolnyi and N. A. Mortensen, "Plasmonics for emerging quantum technologies," *Nanophotonics* **6**, 1185–1188 (2017).
19. A. I. Fernández-Domínguez, S. I. Bozhevolnyi, and N. A. Mortensen, "Plasmon-enhanced generation of non-classical light," *ACS Photonics* **5** (2018).
20. Y. Xiong and X. Lu, "Synthesis of gold colloids," in *"Metallic Nanostructures: From Controlled Synthesis to Applications I"*, D. M. P. Mingos, ed. (Springer International Publishing, 2014).
21. S. Luo, H. Yang, Y. Yang, D. Zhao, X. Chen, M. Qiu, and Q. Li, "Controlling wave-vector of propagating surface plasmon polaritons on single-crystalline gold nanoplates," *Sci. Rep.* **5**, 13424 (2015).
22. T. A. Major, M. S. Devadas, S. S. Lo, and G. V. Hartland, "Optical and dynamical properties of chemically synthesized gold nanoplates," *J. Phys. Chem. C* **117**, 1447–1452 (2013).
23. F. Qin, T. Zhao, R. Jiang, N. Jiang, Q. Ruan, J. Wang, L.-D. Sun, C.-H. Yan, and H.-Q. Lin, "Thickness control produces gold nanoplates with their plasmon in the visible and near-infrared regions," *Adv. Opt. Mater.* **4**, 76–85 (2015).
24. S. Viarbitskaya, A. Teulle, A. Cuche, J. Sharma, C. Girard, E. Dujardin, and A. Arbouet, "Morphology-induced redistribution of surface plasmon modes in two-dimensional crystalline gold platelets," *Appl. Phys. Lett.* **103**, 131112 (2013).
25. A. Cuche, S. Viarbitskaya, J. Sharma, A. Arbouet, C. Girard, and E. Dujardin, "Modal engineering of surface plasmons in apertured au nanoprisms," *Sci. Rep.* **5**, 16635 (2015).
26. S. Viarbitskaya, A. Teulle, R. Marty, J. Sharma, C. Girard, A. Arbouet, and E. Dujardin, "Tailoring and imaging the plasmonic local density of states in crystalline nanoprisms," *Nat. Mater.* **12**, 426 (2013).
27. M. Brust, M. Walker, D. Bethell, D. J. Schiffrin, and R. Whyman, "Synthesis of thiol-derivatised gold nanoparticles in a two-phase liquid-liquid system," *J. Chem. Soc., Chem. Commun.* **7**, 801–802 (1994).
28. B. Radha and G. U. Kulkarni, "A real time microscopy study of the growth of giant au microplates," *Cryst. Growth Des.* **11**, 320–327 (2011).
29. Y. Xia, Y. Xiong, B. Lim, and S. Skrabalak, "Shape-controlled synthesis of metal nanocrystals: Simple chemistry meets complex physics?" *Angew. Chem. Int. Ed.* **48**, 60–103 (2009).
30. R. L. Olmon, B. Slovick, T. W. Johnson, D. Shelton, S.-H. Oh, G. D. Boreman, and M. B. Raschke, "Optical dielectric function of gold," *Phys. Rev. B* **86**, 235147 (2012).
31. D. E. Aspnes and A. A. Studna, "Dielectric functions and optical parameters of si, ge, gap, gaas, gasb, inp, inas, and insb from 1.5 to 6.0 ev," *Phys. Rev. B* **27**, 985–1009 (1983).

B Use of monocrystalline gold flakes for gap plasmon-based metasurfaces



Use of monocrystalline gold flakes for gap plasmon-based metasurfaces operating in the visible

SERGEJS BOROVIKS,¹  FRANCESCO TODISCO,¹ N. ASGER MORTENSEN,^{1,2}  AND SERGEY I. BOZHEVOLNYI^{1,2,*}

¹Center for Nano Optics, University of Southern Denmark, Campusvej 55, DK-5230 Odense M, Denmark

²Danish Institute for Advanced Study, University of Southern Denmark, Campusvej 55, DK-5230 Odense M, Denmark

*seib@mci.sdu.dk

Abstract: Gap plasmon-based optical metasurfaces have been extensively used for demonstration of flat optical elements with various functionalities efficiently operating at near-infrared and telecom wavelengths. Extending their operation to the visible is however impeded by the progressively increased plasmon absorption for shorter wavelengths. We investigate the possibility to improve the performance of gap plasmon-based metasurfaces in the visible by employing monocrystalline gold flakes as substrates instead of evaporated polycrystalline gold films, while using the electron-beam lithography patterning of the evaporated thin gold films for fabrication of top gold nanobricks, which define gap-plasmon resonator elements of the metasurfaces. We demonstrate that the efficiency can be improved by modest but noticeable amount of $\approx 5\%$ if all other configuration parameters are preserved.

© 2019 Optical Society of America under the terms of the [OSA Open Access Publishing Agreement](#)

1. Introduction

Development of the optical metasurfaces [1–3] in the recent years allowed to overcome the limitations of the conventional optical components [4–7]. The main advantages of the metasurfaces as compared to their traditional counterparts are compactness (sub-wavelength thickness) [8–10], multi-functionality [11–15], active and reversible control of the dynamic response [16–23]. This advantage revealed many features and functionalities that were not attainable with conventional optical components [24–27]. One of the classes of the metasurfaces – gap surface plasmon (GSP) [28–31] based – represented by metal-insulator-metal (MIM) configuration and typical operation in reflection mode, in theory, were reported to exhibit relatively high efficiency (up to 90% in the near infrared and 80% in the visible spectral range) [32].

However, in practice efficiency of the metasurface performance is significantly reduced by fabrication imperfections: in addition to deviations from the nanostructure design dimensions (typical tolerances are ± 5 nm), it also suffers from roughness and polycrystallinity of the evaporated metal films, that are commonly employed. These intrinsic properties of the evaporated metal films lead to increased surface scattering and greater Ohmic losses that inevitably decrease the quality of fabricated devices and thus their efficiency. In fact, absorption and scattering losses in typical nanostructures fabricated using the evaporated gold films are so high, that in order to obtain realistic values for the efficiency in numerical simulations, the imaginary part of gold's refractive index has to be pragmatically increased by a factor of 4 [28].

We distinguish two main factors that limit performance of the metasurfaces: deviation from the design dimensions of the constitutive elements caused by lithographic patterning imperfections and intrinsic defects in the polycrystalline metal films that are typically used in the fabrication. Polycrystalline and amorphous noble metals are commonly used for plasmonic metasurface fabrication due to wide availability, relative cheapness and technological simplicity. Thin metal

films are typically deposited by thermal evaporation, electron beam physical vapor deposition or sputtering [33]. While improving the nanofabrication accuracy might require heavy investments in more sophisticated equipment, elimination of material imperfections can be achieved by modifying (at a reasonable cost) the fabrication recipes.

An alternative material platform, which has been receiving increasing attention in the plasmonic community over recent years, is represented by chemically synthesized monocrystalline flakes, also referred to as platelets [34–36]. Due to their atomic flatness and well-defined crystal structure, such plasmonic films and nanoparticles exhibit larger plasmon propagation lengths and sharper resonances due to lower Ohmic losses and reduced surface scattering [37,38]. These superior plasmonic properties have been utilized in the fabrication of plasmonic nano-circuits [39,40], nano-antennae [37,41,42], and other structures [43–45]. It is therefore relatively easy to eliminate material imperfections (at least) in the substrate by using monocrystalline flakes, a seemingly straightforward approach that promises the GSP-based metasurface efficiency improvement by modest, but noticeable $\approx 5\%$, as suggested by the numerical simulations discussed below.

In this work, using numerical simulations and experimental investigations, we study the possibility to improve the performance of beam-steering GSP metasurfaces in the visible by employing monocrystalline gold flakes as substrates (Fig. 1), while using the widely available and well-established electron-beam lithography (EBL) patterning of the evaporated thin gold films for fabrication of top gold nanobricks defining GSP elements of the metasurfaces.

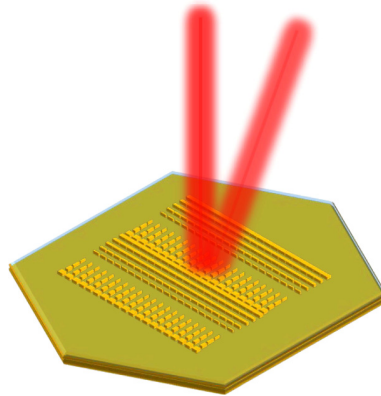


Fig. 1. Beam-steering GSP metasurface on a monocrystalline gold flake: artistic view.

2. Results and discussion

In order to directly evaluate the influence of the material quality of the substrate on the performance of the GSP metasurfaces, we have chosen one of the the simplest designs – the so-called beam steering metasurface that functionally mimics blazed grating, in which a greater part of the incident power is deflected into the non-zero diffraction order. Implementation of such functionality is well studied [28,46] and it is obtained by imposing a linear reflection phase gradient:

$$\Delta\phi_r = \frac{2\pi}{\lambda_0} \sin \theta_r = \frac{2\pi}{\Lambda_s} \quad (1)$$

where θ_r is the beam-steering (first diffraction order) angle, λ_0 is the free space wavelength, Λ_s is the period of the metasurface supercell or grating periodicity as will be explained further. We have chosen the design wavelength $\lambda_0 = 633$ nm, as we expected to observe more pronounced difference between monocrystalline and polycrystalline substrate in the visible range. Besides,

this wavelength is the operational wavelength of the widely used helium-neon (He-Ne) laser. As another design constraint, we have chosen $\theta_r \approx 20^\circ$ due to practical reasons, as it gives well-measurable separation of the diffraction orders and lies in the range of acceptance cone of an objective to be used for optical characterization (which has a numerical aperture of $NA = 0.5$, see Methods sections for the details).

The constitutive elements, or unit cells, of the metasurface are comprised of a widely used configuration – gap plasmon resonator, consisting of a top nanobrick and a thick substrate made of gold, which are separated by a thin silicon dioxide layer, as schematically illustrated in Fig. 2(a). The two degrees of freedom in this system are the lateral dimensions of the nanobrick L_x and L_y , which allow to engineer the local reflection phase and amplitude response, whereas other dimensions – thicknesses of the layers $t = 50$ nm and $t_s = 50$ nm, as well as unit cell period $\Lambda = 180$ nm are kept constant. Reflection amplitude and phase response of the described system is simulated using a commercially available finite-element method (FEM) frequency-domain solver (see Methods section for the details). Based on these simulations we design the supercell of the metasurface, that is represented by a sequence of unit cells, which satisfies the imposed phase gradient (Eq. (1)) in a number of abrupt steps. Given that the unit cell period is $\Lambda = 180$ nm, we have chosen the number of the elements in the supercell n_{el} to be 10, which results in the value of 1st order diffraction angle $\theta_r \approx 20.5$, as

$$\theta_r = \sin^{-1} \frac{\Delta\phi_r \lambda_0}{2\pi} = \sin^{-1} \frac{\lambda_0}{\Lambda_s} = \sin^{-1} \frac{\lambda_0}{\Lambda n_{el}}. \quad (2)$$

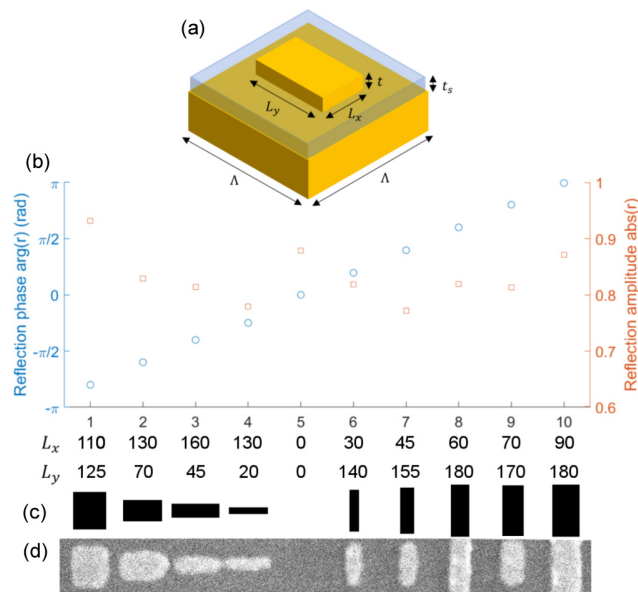


Fig. 2. Design and fabrication of the beam steering gradient GSP metasurface: (a) metasurface unit cell; (b) reflection phase and amplitude of the elements of the supercell; (c) dimensions of the supercell elements; (d) Scanning-electron microscope (SEM) image of the fabricated metasurface supercell.

The dimension L_x and L_y of the elements in the supercell are chosen to have the highest possible reflection amplitude and the smallest deviation from the imposed relative reflection phase, as shown in Fig. 2(b)–(c).

Furthermore, we numerically explore the potential to improve the efficiency of the performance of the metasurface. For that, we carry out full-field simulations of the metasurface supercell to

calculate the power distribution diffraction over the diffraction orders. In the simulations we represent the optical response of the monocrystalline gold described by the electric permittivity $\varepsilon = \varepsilon' + i\varepsilon''$, obtained from the experimental data from Johnson and Christy [47]. In turn, evaporated gold is described by the same permittivity functions, only with the imaginary part ε'' increased by a factor of 4, which mimics additional losses of the polycrystalline material [28]. We compare two cases: a system where both substrate and top nanobricks are described by a lossy permittivity function, and a system where only the top nanobricks are described by the dielectric function with increased imaginary part, whereas the substrate is considered to have less losses. As can be seen from Fig. 3, under the above-mentioned assumptions, the efficiency could improve by modest, but noticeable $\approx 5\%$.

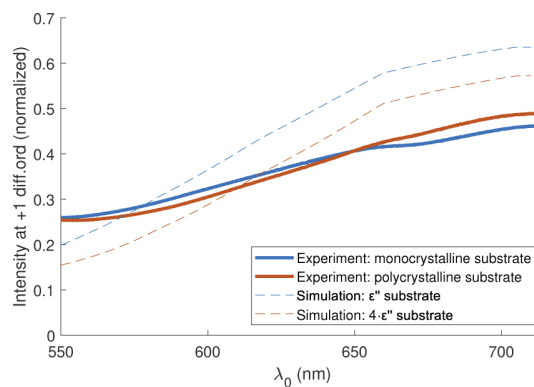


Fig. 3. Efficiency characterization of the metasurface: comparison of numerical simulations (dashed lines) and experiment (solid lines).

For experimental demonstration, we fabricate the designed metasurfaces on two types of gold substrates: evaporated polycrystalline films and chemically synthesized monocrystalline flakes. Descriptions of the preparation of the both substrates can be found in the Methods section. As can be seen from Fig. 3, in practice the effect is not as pronounced as numerical simulations predicted, presumably due to a number of experimental limitations and issues, which will be discussed further.

First of all, significant decrease in the performance efficiency of prototypes as compared to the numerical simulations is ascribed to the fabrication imperfections and uncertainties in the material properties. Tolerances of the EBL fabrication are ± 5 nm that undoubtedly lowers the overall performance of the metasurfaces. As for comparison between monocrystalline and polycrystalline substrates, deviations from the imposed nanobrick dimensions are further increased due to uneven resist deposition on the surface of the flakes caused by a step height at the edges of the flakes, which makes the exact reproducibility of the metasurface very challenging. In order to address this issue, we have fabricated several metasurface patterns with different exposure doses (in a range of $\pm 30\%$ from the dose found to be optimal for the polycrystalline gold substrate).

Another source of the deviation from numerical predictions is caused by the fact that we had to deposit 2 nm of titanium on both, evaporated and monocrystalline gold surfaces for the adhesion purposes, before and after depositing SiO₂ spacer layer. Without this preparatory step, during the sputtering process SiO₂ does not stick uniformly to the gold surface, but rather forms droplets and bubbles that are easy to remove from the surface. Furthermore, we believe that this auxiliary titanium layer contaminates the monocrystalline gold substrate to the extent, that its presence counterbalances the 5% improvement in the efficiency anticipated from the simulations. Also, unsystematic errors in the resist thickness contributes to the reduced observed difference between

mono- and polycrystalline substrates by introducing unavoidable deviations from the design supercell dimensions.

In general, beam-steering GSP metasurfaces are expected to exhibit broadband operation [28]. However, it is somewhat surprising that both experimental and simulated wavelength dependences of the metasurface efficiency exhibit a clear tendency of increasing for longer (than the design) wavelength. We attribute this tendency to the fact that Ohmic losses in gold decrease rapidly when tuning the wavelength away from the interband absorption range towards longer wavelengths. As a result, the metasurfaces operate even more efficiently at wavelengths longer than the design wavelength of 633 nm, reaching efficiencies of $\approx 60\%$ in theory and $\approx 45\%$ in experiment at 700 nm (Fig. 3). Concerning the fact that the efficiency of the metasurface on the polycrystalline substrate surpasses that on the monocrystalline one by few percent at longer wavelengths, we ascribe it to the aforementioned fabrication limitations that become progressively more important for weaker absorption contributions.

Though experimental comparison did not show prominent difference between metasurfaces with mono- and polycrystalline substrates, we have conducted another experiment to clearly demonstrate the superior plasmonic properties of the monocrystalline gold flakes in the absence of fabrication imperfections described above. Specifically, we have measured the propagation length of surface plasmon polaritons (SPP) at the gold-air interface, using the so-called direct scattered intensity (DSI) measurement, that is known to be straightforward and robust method [48,49]. Here, using EBL, we have fabricated a series of ridge gratings at different separations (see inset of Fig. 4 and Methods section for further details). Each grating consists of 3 ridges with thickness 50 nm, width 200 nm and length $20\ \mu\text{m}$ and period 605 nm that approximately corresponds to the SPP wavelength at the vacuum wavelength of $\lambda_0 = 633\ \text{nm}$. As can be seen from Fig. 4, SPP propagation length measurements suggest that propagation losses at the wavelength of interest are significantly (by $\approx 1.6\ \mu\text{m}$, $\approx 11.1\ \mu\text{m}$ for monocrystalline gold versus $\approx 9.5\ \mu\text{m}$ for polycrystalline gold) smaller at the surface of monocrystalline gold.

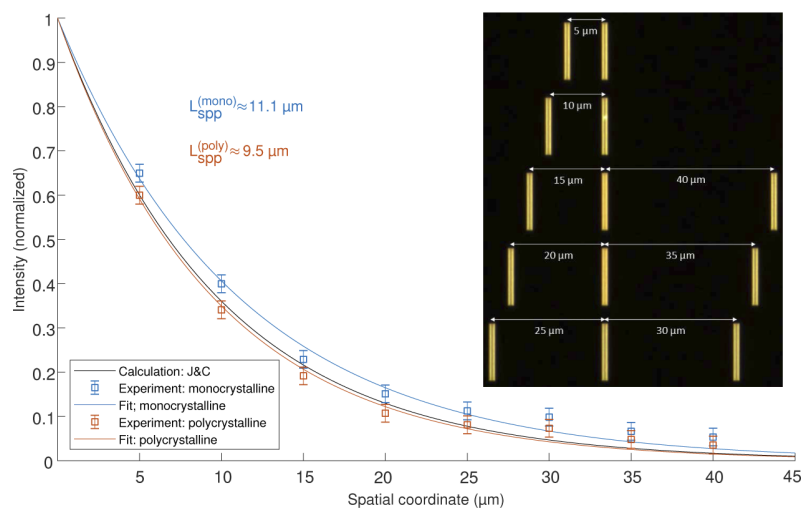


Fig. 4. SPP propagation length measurement at $\lambda_0 = 633\ \text{nm}$: measured data points and exponential fit. Inset: DF optical image of the gratings fabricated on the gold flake for L_{SPP} measurement.

3. Methods

In this section details on experiments and simulations are provided.

3.1. Numerical simulations

Simulations were performed in frequency domain using the wave optics module of the commercially available FEM solver Comsol Multiphysics 5.3. The model implements an excitation by a plain wave at a normal incidence launched from the excitation port, exploiting also appropriate periodic boundary conditions at the borders of the unit cell (or super cell) and receiving port for reflection coefficient (or power distribution over the diffraction orders for the super cell simulation). Tetrahedral meshing (with maximum element sizes of 5 nm in metal, 10 nm in dielectric spacer and 40 nm in air) and third-order polynomial basis functions are used in the simulations to ensure numerically well-converged results. For the permittivity function of gold we have used interpolated experimental data by Johnson and Christy [47], with the imaginary part increased four times in some simulations to mimic the losses caused by fabrication imperfections [28]. The refractive index of dielectric spacer is kept constant ($n = 1.45$). By performing a mesh refinement study we have estimated the relative error in the simulated spectra to be less than one percent.

3.2. Sample fabrication

For the monocrystalline gold flake preparation was used the modified Brust–Schiffrin [50] method for colloidal gold synthesis in a two-phase liquid-liquid system via thermolysis [51], as described in details in the preceding paper [52]. In short, the samples were prepared as following: an aqueous solution of the chloroauric acid in concentration 0.5 M is mixed with a solution of tetraoctylammonium bromide (TOABr) in toluene. After vigorous stirring, the mixture is left in rest allowing aqueous and organic phases to separate. Further, few microlitres of the organic phase are drop-casted onto a substrate (pre-cleaned silicon substrate) which is then kept on the hot-plate at 160°C for 30 minutes. After that the sample is cleaned sequentially in hot toluene, acetone and IPA, that promotes removal of organic solvent. After that the sample is dried under the nitrogen flow, leaving a variety of gold flakes on the surface of the substrate.

For the polycrystalline gold substrate we deposited a 150 nm-thick layer of Au, using standard thermal evaporation method (Cryofox TORNADO 405 evaporation system by Polyteknik).

Further, a 2 nm-thin titanium layer (for adhesion purpose) was evaporated and 50 nm of SiO₂ was radio-frequency sputtered on both substrates.

Further, a 100 nm layer of PMMA 950 A2 e-resist (MicroChem), was spin-coated and metasurface pattern was written using standard EBL (JEOL-640LV SEM with an ELPHY Quantum lithography attachment). The top part of the gap plasmon resonators were formed by thermal evaporation of 2 nm of Ti and 50 nm of Au followed by a lift-off process (etching away stencil material).

3.3. Metasurface optical characterization

Characterization of the metasurfaces performance was performed using Fourier imaging spectroscopy, which allows to clearly observe diffraction orders and evaluate power distribution among them. Optical measurements were performed using the Zeiss Observer microscope (Epiplan-Neofluar HD objective 20×, NA = 0.5) and Andor Kymera 193i spectrograph equipped with Andor Newton CCD camera. Additional lens (achromatic doublet with focal 20 cm) was used to transform real image at the output port of the port of the microscope to Fourier image and project it onto the camera screen. A standard tungsten-halogen lamp was used as an illumination unit in this setup with narrowly closed aperture diaphragm to imitate normal plane wave-like

illumination. Obtained spectra were normalized using reference reflection spectra of silver mirror. Measurements were repeated for several samples ($N = 3$) and presented results are averages.

3.4. SPP propagation length measurement

The same equipment was used for SPP propagation length measurement, with an additional lens to produce real image on the camera screen. As a light source was used super-continuum white light laser (Super K Extreme by NKT Photonics) in conjunction with acousto-optic filter (Super K select) tuned at 633 nm wavelength. The excitation spot was aligned with excitation grating to provide maximum out-coupling signal, which was subsequently recorded, and this procedure was repeated for 8 different separations of the in- and out-coupling gratings. For the determination of propagation distance measurements were fitted with an exponential function.

4. Conclusions

Despite the recent advancement in the nanofabrication methods, the ease of EBL technique is still attractive due to wide availability and low cost. Focused ion beam (FIB) milling technology, that is more expensive, offers better fabrication tolerances, but has other drawbacks, such as surface contamination due to the contamination with working material (e.g. gallium) and re-deposition of the removed material. This fact makes attractive investigation of alternative possibilities for fabrication of plasmonic metasurfaces with improved efficiency.

In this work we show that it is possible to get rid of material imperfections, haunting the performance of plasmonic metasurfaces in the visible, at least in the substrate. Thus, the beam-steering GSP metasurface efficiency can be improved by modest, but noticeable amount of $\approx 5\%$ if all other configuration parameters are preserved. In the practice, however, the effect might not be that pronounced due to other experimental limitations, such as the necessity to deposit few nanometers of titanium as an adhesion layer for SiO_2 spacer layer, unequal deposition of the resist material on the flake surface, and intrinsic tolerances of the EBL fabrication method. The results obtained should serve as guidelines in ever continuing developments towards improving the performance and increasing the efficiency of plasmonic metasurface-based flat optical components.

Funding

H2020 Marie Skłodowska-Curie Actions (713694); H2020 European Research Council (341054); Villum Fonden (16498); V. Kann Rasmussen Foundation (Award in Technical and Natural Sciences 2019); Syddansk Universitet (SDU 2020).

References

1. A. V. Kildishev, A. Boltasseva, and V. M. Shalaev, "Planar photonics with metasurfaces," *Science* **339**(6125), 1232009 (2013).
2. N. Yu and F. Capasso, "Flat optics with designer metasurfaces," *Nat. Mater.* **13**(2), 139–150 (2014).
3. N. Meinzer, W. L. Barnes, and I. R. Hooper, "Plasmonic meta-atoms and metasurfaces," *Nat. Photonics* **8**(12), 889–898 (2014).
4. Y. Zhao, X.-X. Liu, and A. Alù, "Recent advances on optical metasurfaces," *J. Opt.* **16**(12), 123001 (2014).
5. A. A. High, R. C. Devlin, A. Dibos, M. Polking, D. S. Wild, J. Perczel, N. P. de Leon, M. D. Lukin, and H. Park, "Visible-frequency hyperbolic metasurface," *Nature* **522**(7555), 192–196 (2015).
6. D. Lin, P. Fan, E. Hasman, and M. L. Brongersma, "Dielectric gradient metasurface optical elements," *Science* **345**(6194), 298–302 (2014).
7. R. Paniagua-Domínguez, Y. F. Yu, E. Khaidarov, S. Choi, V. Leong, R. M. Bakker, X. Liang, Y. H. Fu, V. Valuckas, L. A. Krivitsky, and A. I. Kuznetsov, "A metalens with a near-unity numerical aperture," *Nano Lett.* **18**(3), 2124–2132 (2018).
8. A. Pors, M. G. Nielsen, R. L. Eriksen, and S. I. Bozhevolnyi, "Broadband focusing flat mirrors based on plasmonic gradient metasurfaces," *Nano Lett.* **13**(2), 829–834 (2013).
9. A. Pors and S. I. Bozhevolnyi, "Efficient and broadband quarter-wave plates by gap-plasmon resonators," *Opt. Express* **21**(3), 2942–2952 (2013).

10. S. Choudhury, U. Guler, A. Shaltout, V. M. Shalaev, A. V. Kildishev, and A. Boltasseva, "Pancharatnam–Berry phase manipulating metasurface for visible color hologram based on low loss silver thin film," *Adv. Opt. Mater.* **5**(10), 1700196 (2017).
11. S. Boroviks, R. A. Deshpande, N. A. Mortensen, and S. I. Bozhevolnyi, "Multifunctional metamirror: Polarization splitting and focusing," *ACS Photonics* **5**(5), 1648–1653 (2018).
12. P. C. Wu, W. Zhu, Z. X. Shen, P. H. J. Chong, W. Ser, D. P. Tsai, and A.-Q. Liu, "Broadband wide-angle multifunctional polarization converter via liquid-metal-based metasurface," *Adv. Opt. Mater.* **5**(7), 1600938 (2017).
13. E. Maguid, I. Yulevich, D. Veksler, V. Kleiner, M. L. Brongersma, and E. Hasman, "Photonic spin-controlled multifunctional shared-aperture antenna array," *Science* **352**(6290), 1202–1206 (2016).
14. E. Maguid, I. Yulevich, M. Yannai, V. Kleiner, M. L. Brongersma, and E. Hasman, "Multifunctional interleaved geometric-phase dielectric metasurfaces," *Light: Sci. Appl.* **6**(8), e17027 (2017).
15. F. Ding, R. Deshpande, and S. I. Bozhevolnyi, "Bifunctional gap-plasmon metasurfaces for visible light: polarization-controlled unidirectional surface plasmon excitation and beam steering at normal incidence," *Light: Sci. Appl.* **7**(4), 17178 (2018).
16. P. Gutruf, C. Zou, W. Withayachumnankul, M. Bhaskaran, S. Sriram, and C. Fumeaux, "Mechanically tunable dielectric resonator metasurfaces at visible frequencies," *ACS Nano* **10**(1), 133–141 (2016).
17. A. Karvounis, B. Gholipour, K. F. MacDonald, and N. I. Zheludev, "All-dielectric phase-change reconfigurable metasurface," *Appl. Phys. Lett.* **109**(5), 051103 (2016).
18. J. Sautter, I. Staude, M. Decker, E. Rusak, D. N. Neshev, I. Brener, and Y. S. Kivshar, "Active tuning of all-dielectric metasurfaces," *ACS Nano* **9**(4), 4308–4315 (2015).
19. M. L. Tseng, J. Yang, M. Semmlinger, C. Zhang, P. Nordlander, and N. J. Halas, "Two-dimensional active tuning of an aluminum plasmonic array for full-spectrum response," *Nano Lett.* **17**(10), 6034–6039 (2017).
20. Y.-W. Huang, H. W. H. Lee, R. Sokhoyan, R. A. Pala, K. Thyagarajan, S. Han, D. P. Tsai, and H. A. Atwater, "Gate-tunable conducting oxide metasurfaces," *Nano Lett.* **16**(9), 5319–5325 (2016).
21. M. Rahmani, L. Xu, A. E. Miroschnichenko, A. Komar, R. Camacho-Morales, H. Chen, Y. Zárate, S. Kruk, G. Zhang, D. N. Neshev, and Y. S. Kivshar, "Reversible thermal tuning of all-dielectric metasurfaces," *Adv. Funct. Mater.* **27**(31), 1700580 (2017).
22. Q. Wang, E. T. Rogers, B. Gholipour, C.-M. Wang, G. Yuan, J. Teng, and N. I. Zheludev, "Optically reconfigurable metasurfaces and photonic devices based on phase change materials," *Nat. Photonics* **10**(1), 60–65 (2016).
23. F. Cheng, L. Qiu, D. Nikolov, A. Bauer, J. P. Rolland, and A. N. Vamivakas, "Mechanically tunable focusing metamirror in the visible," *Opt. Express* **27**(11), 15194–15204 (2019).
24. F. Ding, A. Pors, and S. I. Bozhevolnyi, "Gradient metasurfaces: fundamentals and applications," *Rep. Prog. Phys.* **81**(2), 026401 (2018).
25. S. B. Glybovski, S. A. Tretyakov, P. A. Belov, Y. S. Kivshar, and C. R. Simovski, "Metasurfaces: From microwaves to visible," *Phys. Rep.* **634**, 1–72 (2016).
26. H.-H. Hsiao, C. H. Chu, and D. P. Tsai, "Fundamentals and applications of metasurfaces," *Small Methods* **1**(4), 1600064 (2017).
27. A. Kristensen, J. K. W. Yang, S. I. Bozhevolnyi, S. Link, P. Nordlander, N. J. Halas, and N. A. Mortensen, "Plasmonic colour generation," *Nat. Rev. Mater.* **2**(1), 16088 (2017).
28. A. Pors, O. Albrektsen, I. P. Radko, and S. I. Bozhevolnyi, "Gap plasmon-based metasurfaces for total control of reflected light," *Sci. Rep.* **3**(1), 2155 (2013).
29. H. T. Miyazaki and Y. Kurokawa, "Controlled plasmon resonance in closed metal/insulator/metal nanocavities," *Appl. Phys. Lett.* **89**(21), 211126 (2006).
30. S. I. Bozhevolnyi and T. Søndergaard, "General properties of slow-plasmon resonant nanostructures: nano-antennas and resonators," *Opt. Express* **15**(17), 10869–10877 (2007).
31. A. S. Roberts, A. Pors, O. Albrektsen, and S. I. Bozhevolnyi, "Subwavelength plasmonic color printing protected for ambient use," *Nano Lett.* **14**(2), 783–787 (2014).
32. F. Ding, Y. Yang, A. Deshpande Rucha, and I. Bozhevolnyi Sergey, "A review of gap-surface plasmon metasurfaces: fundamentals and applications," *Nanophotonics* **7**(6), 1129–1156 (2018).
33. K. M. McPeak, S. V. Jayanti, S. J. Kress, S. Meyer, S. Iotti, A. Rossinelli, and D. J. Norris, "Plasmonic films can easily be better: rules and recipes," *ACS Photonics* **2**(3), 326–333 (2015).
34. X. Wu, R. Kullock, E. Krauss, and B. Hecht, "Single-crystalline gold microplates grown on substrates by solution-phase synthesis," *Cryst. Res. Technol.* **50**(8), 595–602 (2015).
35. B. Hoffmann, M. Y. Bashouti, T. Feichtner, M. Mačković, C. Dieker, A. M. Salaheldin, P. Richter, O. D. Gordan, D. R. T. Zahn, E. Spiecker, and S. Christiansen, "New insights into colloidal gold flakes: structural investigation, micro-ellipsometry and thinning procedure towards ultrathin monocrystalline layers," *Nanoscale* **8**(8), 4529–4536 (2016).
36. E. Krauss, R. Kullock, X. Wu, P. Geisler, N. Lundt, M. Kamp, and B. Hecht, "Controlled growth of high-aspect-ratio single-crystalline gold platelets," *Cryst. Growth Des.* **18**(3), 1297–1302 (2018).
37. R. Méjard, A. Verdy, O. Demichel, M. Petit, L. Markey, F. Herbst, R. Chassagnon, G. Colas-des Francs, B. Cluzel, and A. Bouhelier, "Advanced engineering of single-crystal gold nanoantennas," *Opt. Mater. Express* **7**(4), 1157–1168 (2017).

38. K. J. Kaltenecker, E. Krauss, L. Casses, M. Geisler, B. Hecht, N. A. Mortensen, P. U. Jepsen, and N. Stenger, "Mono-crystalline gold platelets: A high quality platform for surface plasmon polaritons," arXiv:1909.08321.
39. F. Cardano, M. Maffei, F. Massa, B. Piccirillo, C. de Lisio, G. De Filippis, V. Cataudella, E. Santamato, and L. Marrucci, "Atomically flat single-crystalline gold nanostructures for plasmonic nanocircuitry," *Nat. Commun.* **1**(1), 150 (2010).
40. W.-H. Dai, F.-C. Lin, C.-B. Huang, and J.-S. Huang, "Mode conversion in high-definition plasmonic optical nanocircuits," *Nano Lett.* **14**(7), 3881–3886 (2014).
41. J. C. Prangma, J. Kern, A. G. Knapp, S. Grossmann, M. Emmerling, M. Kamp, and B. Hecht, "Electrically connected resonant optical antennas," *Nano Lett.* **12**(8), 3915–3919 (2012).
42. J. Kern, R. Kulloock, J. Prangma, M. Emmerling, M. Kamp, and B. Hecht, "Electrically driven optical antennas," *Nat. Photonics* **9**(9), 582–586 (2015).
43. S. Schmidt, B. Piglosiewicz, D. Sadiq, J. Shirdel, J. S. Lee, P. Vasa, N. Park, D.-S. Kim, and C. Lienau, "Adiabatic nanofocusing on ultrasmooth single-crystalline gold tapers creates a 10-nm-sized light source with few-cycle time resolution," *ACS Nano* **6**(7), 6040–6048 (2012).
44. B. Frank, P. Kahl, D. Podbiel, G. Spektor, M. Orenstein, L. Fu, T. Weiss, M. Horn-von Hoegen, T. J. Davis, F.-J. Meyer zu Heringdorf, and H. Giessen, "Short-range surface plasmonics: Localized electron emission dynamics from a 60-nm spot on an atomically flat single-crystalline gold surface," *Sci. Adv.* **3**(7), e1700721 (2017).
45. H. Siampour, O. Wang, V. A. Zenin, S. Boroviks, P. Siyushev, Y. Yang, V. A. Davydov, L. F. Kulikova, V. N. Agafonov, A. Kubanek, N. A. Mortensen, F. Jelezko, and S. I. Bozhevolnyi, "Unidirectional single-photon emission from germanium-vacancy zero-phonon lines: Deterministic emitter-waveguide interfacing at plasmonic hot spots," arXiv:1903.05446.
46. N. Yu, P. Genevet, M. A. Kats, F. Aieta, J.-P. Tetienne, F. Capasso, and Z. Gaburro, "Light propagation with phase discontinuities: Generalized laws of reflection and refraction," *Science* **334**(6054), 333–337 (2011).
47. P. B. Johnson and R. W. Christy, "Optical constants of the noble metals," *Phys. Rev. B* **6**(12), 4370–4379 (1972).
48. C.-Y. Wang, H.-Y. Chen, L. Sun, W.-L. Chen, Y.-M. Chang, H. Ahn, X. Li, and S. Gwo, "Giant colloidal silver crystals for low-loss linear and nonlinear plasmonics," *Nat. Commun.* **6**(1), 7734 (2015).
49. P. Nagpal, N. C. Lindquist, S.-H. Oh, and D. J. Norris, "Ultrasmooth patterned metals for plasmonics and metamaterials," *Science* **325**(5940), 594–597 (2009).
50. M. Brust, M. Walker, D. Bethell, D. J. Schiffrin, and R. Whyman, "Synthesis of thiol-derivatised gold nanoparticles in a two-phase liquid–liquid system," *J. Chem. Soc., Chem. Commun.* **0**(7), 801–802 (1994).
51. B. Radha and G. U. Kulkarni, "A real time microscopy study of the growth of giant au microplates," *Cryst. Growth Des.* **11**(1), 320–327 (2011).
52. S. Boroviks, C. Wolff, J. Linnet, Y. Yang, F. Todisco, A. S. Roberts, S. I. Bozhevolnyi, B. Hecht, and N. A. Mortensen, "Interference in edge-scattering from monocrystalline gold flakes," *Opt. Mater. Express* **8**(12), 3688–3697 (2018).

C Anisotropic second-harmonic generation from monocrystalline gold flakes

Anisotropic Second Harmonic Generation From Monocrystalline Gold Flakes

Sergejs Boroviks,¹ Torgom Yezekyan,¹ Álvaro Rodríguez Echarri,^{2,1} F. Javier García de Abajo,^{2,3}
Joel D. Cox,^{1,4} Sergey I. Bozhevolnyi,^{1,4} N. Asger Mortensen,^{1,4} and Christian Wolff¹

¹*Centre for Nano Optics, University of Southern Denmark, Campusvej 55, DK-5230 Odense M, Denmark*

²*ICFO — Institut de Ciències Fotoniques, The Barcelona Institute of Science and Technology, 08860 Castelldefels (Barcelona), Spain*

³*ICREA — Institució Catalana de Recerca i Estudis Avançats, Passeig Lluís Companys 23, 08010 Barcelona, Spain*

⁴*Danish Institute for Advanced Study, University of Southern Denmark, Campusvej 55, DK-5230 Odense M, Denmark*

(Dated: December 21, 2020)

Noble metals with well-defined crystallographic orientation constitute an appealing class of materials for controlling light-matter interactions on the nanoscale. Nonlinear optical processes, being particularly sensitive to anisotropy, are a natural and versatile probe of crystallinity in nano-optical devices. Here we study the nonlinear optical response of monocrystalline gold flakes, revealing a polarization dependence in second-harmonic generation from the {111} surface that is markedly absent in polycrystalline films. Apart from suggesting an approach for directional enhancement of nonlinear response in plasmonic systems, we anticipate that our findings can be used as a rapid and non-destructive method for characterization of crystal quality and orientation that may be of significant importance in future applications.

The experimental discovery of second-harmonic generation (SHG) from a metallic boundary [1] triggered extensive studies of nonlinear optical processes in metals that have spanned several decades. One of the early pioneering works [2] reported SHG in reflection from various metal surfaces and established the central theoretical treatment of this phenomenon. Effectively, the induced second-order polarization can be expressed as [3]

$$P_i(2\omega) = \sum_{jk} \chi_{ijk}^{(2)} E_j(\omega) E_k(\omega), \quad (1)$$

where $\chi_{ijk}^{(2)}$ is the effective second-order susceptibility tensor component, i, j, k indices run over Cartesian coordinates x, y, z , and E_i denotes the electric field vector component i at the fundamental frequency ω .

In their natural form, noble-metal crystals occur in centro-symmetric form, as face-centre-cubic (FCC) lattice crystals, rendering SHG symmetry-forbidden within the dipole approximation, while multipole interactions enable weak second-order nonlinear effects even in centro-symmetric media [4]. Nonetheless, SHG from noble metals can be observed in reflection from metal-dielectric interfaces, where the inversion symmetry of the bulk crystal is broken and the second-order nonlinear response is no longer prohibited. The exact nature of this phenomenon remained a matter of debate over decades in the nonlinear optics community, with the main focus placed on the separation between the dipole surface-like contribution (occurring due to breaking of translation symmetry at the interface) and quadrupole bulk-like contributions (associated with strong field gradients at the metal surface) [5–8]. Important theoretical developments by Rudnick and Stern [9] eventually showed that both surface and bulk induced currents may be important, and the two can be related to the corresponding $\chi^{(2)}$ tensor via phenomenological constants. A significant breakthrough

in the experimental investigation of this question was made by Wang *et al.* [10], who showed, using sophisticated two-beam SHG measurements, that surface dipole effects dominate the nonlinearity in sputtered (implying polycrystalline) gold films.

In contrast to surfaces of polycrystalline metal films, their monocrystalline counterparts are known to exhibit anisotropic surface SHG, which manifests in the dependence of the emitted light polarization on the orientation of the sample relative to the excitation polarization. One of the first experimental observations was obtained from the silicon {111} surface [11], later also extended to surfaces of noble-metal crystals [12–17]. These experimental demonstrations agree well with predictions of the phenomenological model developed by Sipe *et al.* [18], who derived expressions for the second-order susceptibility tensor components arising from both bulk- and surface-like contributions, based on symmetry considerations for three conventional FCC crystal surfaces — {100}, {110}, and {111}.

In this work, we experimentally investigate SHG from monocrystalline gold flakes, which have recently become a material platform of interest for high-quality plasmonic devices [19–21], owing to the moderate optical damping associated with both their atomic-scale surface flatness and high degree of crystallinity [22, 23]. We show that the {111} surface of the gold flakes exhibits polarization-dependent second-harmonic generation, which is nearly order of magnitude stronger than that observed in isotropic SH emission of evaporated gold films. The anisotropic nonlinear optical response we report here may be of crucial importance for directional enhancement of harmonic generation in metal nanostructures [24–27]. Furthermore, we suggest that our findings can be used as a fast and non-destructive method for characterization of crystallinity and lattice orientation of metal substrates, which is an important asset for ongoing

experimental activities on quantum surface effects and future plasmonic applications [28–30].

Monocrystalline gold flake samples are synthesized using a modified Brust–Schiffrin method [31], as described in detail elsewhere [32]. The gold flakes have high aspect ratio, typically spanning $\approx 100\ \mu\text{m}$ in lateral directions and a few hundred nanometers in thickness. Optical micrographs of the gold flake sample investigated in this Letter are presented in Fig. 1(a) and (b), revealing the absence of defects or contamination on the surface of the sample. The gold flakes have a FCC crystal lattice and their hexagonal faces are of the $\{111\}$ type [33], as illustrated schematically in Fig. 1(c) alongside our definition of the coordinate frame and relevant angles. The evaporated gold film sample was prepared in a Cryofox TORNADO 405 evaporation system by Polyteknik, by depositing a 120 nm gold layer on a silicon substrate previously coated with a 3 nm titanium layer for adhesion purposes. Such gold films are known to be intrinsically polycrystalline [34].

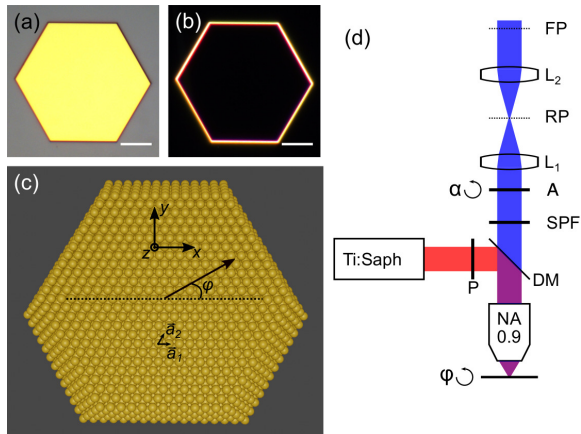


FIG. 1. (a) Bright-field and (b) dark-field optical microscope images of the investigated gold flake. Scale bars are $20\ \mu\text{m}$. (c) Illustration of the crystal lattice of the gold flake with indicated $\{111\}$ surface lattice primitive vectors \vec{a}_1 and \vec{a}_2 , the sample orientation angle ϕ with respect to excitation polarization and coordinate axis. (d) Schematics of the experimental setup: a laser beam from a Ti:Saph oscillator is filtered using a polarizer (P) and then focused on to a sample with an apochromatic objective. The nonlinear reflection is collected with the same objective and filtered out using a dichroic mirror (DM) and a short-pass filter (SPF). The polarization of the nonlinear signal is resolved using an analyzer (A), whereas the signal can be recorded either in the real image plane (RP) or Fourier image plane (FP) created by lenses L_1 and L_2 , respectively.

The experimental setup, schematically depicted in Fig. 1 (d), is a custom-made scanning nonlinear microscope equipped with interchangeable detectors, namely: spectrograph (Ocean Optics QEPro), photo-multiplying tube (Hamamatsu R3235-01) and sCMOS camera (Thorlabs CS235MU). The sample is mounted on a computer-controlled scanning stage with an in-plane rotation stage,

which allows us to investigate the anisotropy of the sample. The laser source used in the experiment is a mode-locked Titanium-Sapphire (Ti:Saph) laser (Tsunami 3941 by Spectra-Physics), tunable in the 780–840 nm wavelength range, with pulse duration of $\approx 1\ \text{ps}$. The excitation and collection of the SH signal is performed using a high (0.9) numerical aperture (NA) objective (Olympus MPLFN100X). All measurements described in this work were performed with $\approx 100\ \text{mW}$ average power focused to the diffraction-limited ($\approx 450\ \text{nm}$) excitation spot. Finally, the polarization state and angular distribution of the SH emission can be analyzed, for example, by recording polarization-resolved Fourier images.

First, we study spectra of the nonlinear emission from the monocrystalline gold flake in the 780–840 nm range of excitation wavelengths and compare it with the evaporated gold film. Fig. 2 shows that the SH intensity generated at a crystalline surface is almost one order of magnitude stronger than at its polycrystalline counterpart, which can be explained by the presence of a large anisotropic contribution in former and absence of it in latter, as will be discussed below.

The main trend for both monocrystalline and polycrystalline surfaces is that the efficiency of SHG increases with increasing wavelength, which may be attributed to the excitation of a plasmon resonance at the fundamental frequency [35, 36] and reduced coupling of SH fields to the interband transitions [15]. In addition, two-photon luminescence (TPL), characterized by emission in the broad 450–550 nm range, is found to decrease with increasing wavelength. TPL arises from a third-order nonlinear process [37], which is incoherent and known to be significantly enhanced at rough surfaces and higher excitation energies [38, 39]. Here, we also observe approximately 35% less TPL emission from the smoother crystalline gold surface.

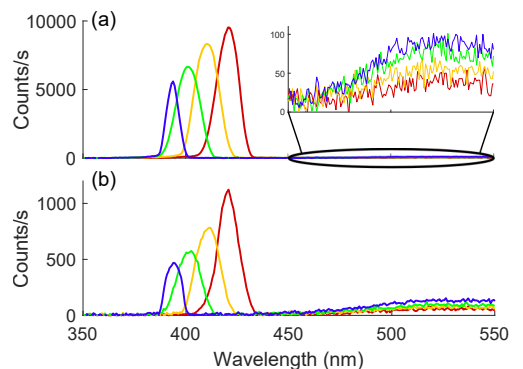


FIG. 2. Spectrum of the nonlinear reflection from (a) a $\{111\}$ surface of a monocrystalline gold flake and (b) evaporated polycrystalline gold. The inset in (a) shows a zoom-in of the measured TPL spectral region (450–550 nm). Curve colors indicate excitation wavelength: 780 nm (blue), 800 nm (green), 820 nm (yellow), and 840 nm (red).

The symmetry group of the large $\{111\}$ surfaces of

our gold flakes is not the hexagonal point group C_{6v} that one might expect from the arrangement of the top layer of atoms; it is rather the trigonal point group C_{3v} due to the stacking order of the FCC crystal breaking some of the hexagonal symmetries. Based on the above mentioned symmetry argument, it was generally shown that the second-order susceptibility $\chi_{ijk}^{(2)}$, which is a third-rank tensor, should have 11 non-zero and 5 independent elements [18, 40]. One can separate anisotropic and isotropic contributions, as some of the tensor components explicitly reflect the sample orientation angle ϕ with respect to the excitation polarization: $\chi_{xxx}^{(2)} = -\chi_{xyy}^{(2)} = -\chi_{yxy}^{(2)}$ are associated with SHG $\propto \sin(3\phi)$; $\chi_{xxy}^{(2)} = \chi_{yxx}^{(2)} = -\chi_{yyy}^{(2)}$ are associated with SHG $\propto \cos(3\phi)$; and $\chi_{zxx}^{(2)} = \chi_{zyy}^{(2)}$, $\chi_{xzz}^{(2)} = \chi_{yzz}^{(2)}$ and $\chi_{zzz}^{(2)}$ are associated with isotropic SHG. The indices of the $\chi^{(2)}$ tensor correspond to the axis defined in Fig. 1(c). Noticeably, anisotropic tensor components that give rise to in-plane induced polarization interact only with the in-plane E -field components E_x and E_y .

With this phenomenological treatment, the dependence of SHG on the sample orientation angle can be described with a simple model for co-polarized and cross-polarized detection:

$$I_{\parallel}(2\omega) \propto |a_{i\parallel} - a_{a\parallel} \sin 3\phi|^2 I^2(\omega), \quad (2a)$$

$$I_{\perp}(2\omega) \propto |a_{i\perp} + a_{a\perp} \cos 3\phi|^2 I^2(\omega), \quad (2b)$$

where $I_{\parallel}(2\omega)$ and $I_{\perp}(2\omega)$ denote co-polarized and cross-polarized detected intensity, $I(\omega)$ is the excitation intensity, while a_i and a_a are the corresponding complex-valued phenomenological constants describing isotropic and anisotropic contributions to SHG, respectively.

As can be seen from Fig. 3(a), we indeed observe such variation in the SH intensity for the gold flake at 800 nm excitation wavelength. By fitting the data to the model we estimate amplitude and phase ratios of the isotropic and anisotropic constants to obtain $a_{i\parallel}/a_{a\parallel} \approx 0.4e^{i91^\circ}$ and $a_{i\perp}/a_{a\perp} \approx 0.1e^{i90^\circ}$. In contrast, evaporated gold samples do not exhibit any anisotropy in SHG [Fig. 3(f)], which can be explained by the fact that the overall response of a polycrystalline film is the average of the individual, randomly oriented domains.

In addition, we study Fourier images of the SH emission, shown in Fig. 3(b)–(e), (g), and (h). We find that the weak isotropic contribution can be separated from any strong anisotropic contribution when the excitation polarization is parallel to one of the primitive surface lattice vectors \vec{a} (i.e., $\phi = 0^\circ$) in co-polarized detection. The depletion of intensity in the center and the petal-shaped intensity distribution indicate that the SH signal is emitted at off-normal angles. The anisotropic contribution is dominant in cross-polarized detection for the same flake orientation and in co-polarized detection when $\phi = 30^\circ$. Its intensity is concentrated mainly in the center of the Fourier images, indicating that SH emission occurs in the direction normal to the sample surface. Finally, the polycrystalline gold sample shows only inten-

sity at slanted angles in co-polarized detection, implicitly indicating that only isotropic components of the second-order susceptibility tensor are probed by the out-of-plane electric field components.

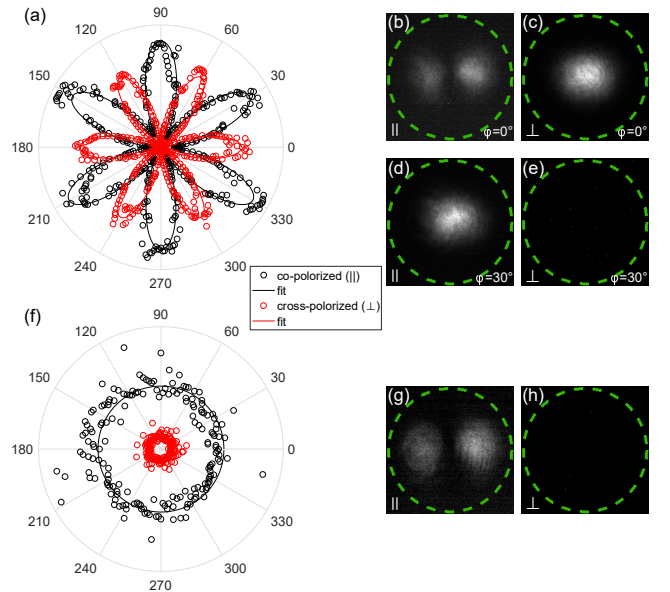


FIG. 3. Polarization-resolved measurements of (a)–(e) mono- and (f)–(h) polycrystalline samples. (a) Polar plot of SH intensity as a function of crystal orientation angle for co-polarized and cross-polarized detection. (b)–(e) Fourier images of the SH emission from the $\{111\}$ surface of a monocrystalline gold flake in co-polarized and cross-polarized detection with orientations $\phi = 0^\circ$ and $\phi = 30^\circ$, respectively. (f) Polar plot, (g) co-polarized, and (h) cross-polarized Fourier images of SH emission from an evaporated gold sample. Green-dashed circles in panels (b)–(e), (g), and (h) indicate the border of the acceptance angle of the objective (NA = 0.9), which also corresponds to the size of the excitation spot in the Fourier plane.

Relative intensities and angular distributions of the isotropic and anisotropic SH emission can be also attributed to the electric field profile of the excitation beam in the focal plane. Fig. 4(a)–(c) shows the electric field distributions of a tightly focused Gaussian beam (TFGB) calculated by numerical evaluation of the diffraction integral of the angular spectrum, with parameters chosen to approximately match experimental conditions (800 nm wavelength, NA = 0.9) [41]. Fig. 4(d)–(f) shows spatial distributions of the second-order polarization induced by the TFGB fields. Clearly, P_x , the in-plane component of the polarization parallel to that of the Gaussian beam, is dominant, whereas P_z is one order of magnitude weaker and P_y is nearly absent. Thus, the relative intensity of the anisotropic SH is more prominent, as it is generated only by the strong in-plane field E_x , in comparison to the out-of-plane polarization induced by the much weaker E_z component. Additionally, the spatial distribution of P_z , which can be interpreted as two dipole-like sources separated by a distance of one wavelength, is consistent

with the observed petals in the angular distribution of the isotropic SH [Fig. 4(d) and (f)], which arises due to far-field interference of the two in-phase oscillating dipoles.

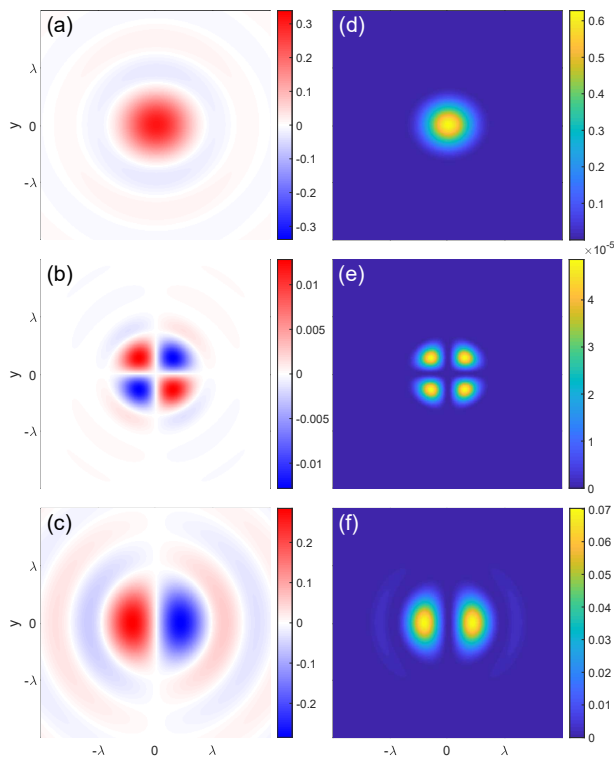


FIG. 4. (a) E_x , (b) E_y , and (c) E_z components of the electric field at the fundamental frequency ω in the focal plane of a TFGB. (d) P_x , (e) P_y , and (f) P_z components of the induced second-order polarization at frequency 2ω . The color scales in all plots are normalized to yield the same maximum intensity of the E -field at frequency ω .

To summarize, we report strong anisotropy in the SHG from monocrystalline gold flakes, which is related to the three-fold symmetry of the $\{111\}$ surface. The

anisotropic elements of the $\chi^{(2)}$ tensor interact mainly with the in-plane electric field components and correspondingly induce in-plane second-order polarization, which leads to SH emission at angles close to the surface normal. Such anisotropy is absent in polycrystalline gold films due to the random orientation of the crystal domains, which effectively averages out the anisotropic contribution to zero and thus decreases the overall SH emission by approximately one order of magnitude under the given experimental conditions. In contrast, an isotropic SHG component, caused by the out-of-plane fields that produce emission at angles slanted off the surface normal, is present for both poly- and monocrystalline gold surfaces. We anticipate that our findings will serve as a method for probing sample crystallinity and surface lattice orientation, and may guide future efforts to enhance the efficiency of second-order nonlinear optical processes in high-quality nonlinear plasmonic devices.

FUNDING

C. W. and T. Y. acknowledge funding from MULTIPLY fellowships under the Marie Skłodowska-Curie COFUND Action (grant agreement No. 713694). A.R.E acknowledges the Secretaria d'Universitats i Recerca del Departament d'Empresa i Coneixement de la Generalitat de Catalunya, as well as the European Social Fund (L'FSE inverteix en el teu futur)-FEDER. FJGA acknowledges support from the Spanish MINECO (MAT2017-88492-R and SEV2015-0522). N. A. M. is a VILLUM Investigator supported by VILLUM FONDEN (grant No. 16498) and Independent Research Funding Denmark (grant no. 7026-00117B). The Center for Nano Optics is financially supported by the University of Southern Denmark (SDU 2020 funding).

DISCLOSURES

The authors declare no conflicts of interest.

-
- [1] F. Brown, R. E. Parks, and A. M. Sleeper, Nonlinear optical reflection from a metallic boundary, *Phys. Rev. Lett.* **14**, 1029 (1965).
 - [2] N. Bloembergen, R. K. Chang, S. S. Jha, and C. H. Lee, Optical second-harmonic generation in reflection from media with inversion symmetry, *Phys. Rev.* **174**, 813 (1968).
 - [3] R. W. Boyd, *Nonlinear optics* (Academic press, 2019).
 - [4] P. Guyot-Sionnest and Y. R. Shen, Bulk contribution in surface second-harmonic generation, *Phys. Rev. B* **38**, 7985 (1988).
 - [5] J. E. Sipe, V. C. Y. So, M. Fukui, and G. I. Stegeman, Analysis of second-harmonic generation at metal surfaces, *Phys. Rev. B* **21**, 4389 (1980).
 - [6] P. Guyot-Sionnest, W. Chen, and Y. R. Shen, General considerations on optical second-harmonic generation from surfaces and interfaces, *Phys. Rev. B* **33**, 8254 (1986).
 - [7] M. Weber and A. Liebsch, Density-functional approach to second-harmonic generation at metal surfaces, *Phys. Rev. B* **35**, 7411 (1987).
 - [8] W. L. Schaich and A. Liebsch, Nonretarded hydrodynamic-model calculation of second-harmonic generation at a metal surface, *Phys. Rev. B* **37**, 6187 (1988).
 - [9] J. Rudnick and E. A. Stern, Second-harmonic radiation from metal surfaces, *Phys. Rev. B* **4**, 4274 (1971).
 - [10] F. X. Wang, F. J. Rodríguez, W. M. Albers, R. Ahorinta, J. E. Sipe, and M. Kauranen, Surface and bulk contribu-

- tions to the second-order nonlinear optical response of a gold film, *Phys. Rev. B* **80**, 233402 (2009).
- [11] H. W. K. Tom, T. F. Heinz, and Y. R. Shen, Second-harmonic reflection from silicon surfaces and its relation to structural symmetry, *Phys. Rev. Lett.* **51**, 1983 (1983).
- [12] A. Friedrich, B. Pettinger, D. Kolb, G. Lüpke, R. Steinhoff, and G. Marowsky, An in situ study of reconstructed gold electrode surfaces by second harmonic generation, *Chem. Phys. Lett.* **163**, 123 (1989).
- [13] G. Lüpke, G. Marowsky, R. Steinhoff, A. Friedrich, B. Pettinger, and D. M. Kolb, Symmetry superposition studied by surface second-harmonic generation, *Phys. Rev. B* **41**, 6913 (1990).
- [14] D. A. Koos, V. L. Shannon, and G. L. Richmond, Surface-dipole and electric-quadrupole contributions to anisotropic second-harmonic generation from noble-metal surfaces, *Phys. Rev. B* **47**, 4730 (1993).
- [15] E. K. L. Wong and G. L. Richmond, Examination of the surface second harmonic response from noble metal surfaces at infrared wavelengths, *J. Chem. Phys.* **99**, 5500 (1993).
- [16] I. Yagi, S. Nakabayashi, and K. Uosaki, In situ optical second harmonic rotational anisotropy measurements of an au(111) electrode during electrochemical deposition of tellurium, *J. Phys. Chem. B* **102**, 2677 (1998).
- [17] C. Matranga and P. Guyot-Sionnest, Absolute intensity measurements of the optical second-harmonic response of metals from 0.9 to 2.5 eV, *J. Chem. Phys.* **115**, 9503 (2001).
- [18] J. E. Sipe, D. J. Moss, and H. M. van Driel, Phenomenological theory of optical second- and third-harmonic generation from cubic centrosymmetric crystals, *Phys. Rev. B* **35**, 1129 (1987).
- [19] J.-S. Huang, V. Callegari, P. Geisler, C. Brüning, J. Kern, J. C. Prangma, X. Wu, T. Feichtner, J. Ziegler, P. Weinmann, *et al.*, Atomically flat single-crystalline gold nanostructures for plasmonic nanocircuitry, *Nat. Commun.* **1**, 150 (2010).
- [20] K. J. Kaltenecker, E. Krauss, L. Casses, M. Geisler, B. Hecht, N. A. Mortensen, P. U. Jepsen, and N. Stenger, Mono-crystalline gold platelets: a high-quality platform for surface plasmon polaritons, *Nanophotonics* **9**, 509 (2020).
- [21] H. Siampour, O. Wang, V. A. Zenin, S. Boroviks, P. Siyushev, Y. Yang, V. A. Davydov, L. F. Kulikova, V. N. Agafonov, A. Kubanek, *et al.*, Ultrabright single-photon emission from germanium-vacancy zero-phonon lines: deterministic emitter-waveguide interfacing at plasmonic hot spots, *Nanophotonics* **9**, 953 (2020).
- [22] R. Méjard, A. Verdy, O. Demichel, M. Petit, L. Markey, F. Herbst, R. Chassagnon, G. Colas-des Francs, B. Cluzel, and A. Bouhelier, Advanced engineering of single-crystal gold nanoantennas, *Opt. Mater. Express* **7**, 1157 (2017).
- [23] S. Boroviks, F. Todisco, N. A. Mortensen, and S. I. Bozhevolnyi, Use of monocrystalline gold flakes for gap plasmon-based metasurfaces operating in the visible, *Opt. Mater. Express* **9**, 4209 (2019).
- [24] P. Mühlischlegel, H.-J. Eisler, O. J. F. Martin, B. Hecht, and D. W. Pohl, Resonant optical antennas, *Science* **308**, 1607 (2005), <https://science.sciencemag.org/content/308/5728/1607.full.pdf>.
- [25] J. Renger, R. Quidant, and L. Novotny, Enhanced nonlinear response from metal surfaces, *Optics Express* **19**, 1777 (2011).
- [26] M. Kauranen and A. V. Zayats, Nonlinear plasmonics, *Nature photonics* **6**, 737 (2012).
- [27] J. Butet, P.-F. Brevet, and O. J. Martin, Optical second harmonic generation in plasmonic nanostructures: from fundamental principles to advanced applications, *ACS nano* **9**, 10545 (2015).
- [28] S. Großmann, D. Friedrich, M. Karolak, R. Kullock, E. Krauss, M. Emmerling, G. Sangiovanni, and B. Hecht, Nonclassical optical properties of mesoscopic gold, *Phys. Rev. Lett.* **122**, 246802 (2019).
- [29] A. R. Echarri, P. A. D. Gonçalves, C. Tserkezis, F. J. García de Abajo, N. A. Mortensen, and J. D. Cox, Optical response of noble metal nanostructures: Quantum surface effects in crystallographic facets, arXiv preprint (2020), arXiv:2009.10821.
- [30] Z. M. Abd El-Fattah, V. Mkhitarian, J. Brede, L. Fernández, C. Li, Q. Guo, A. Ghosh, A. R. Echarri, D. Naveh, F. Xia, *et al.*, Plasmonics in atomically thin crystalline silver films, *ACS Nano* **13**, 7771 (2019).
- [31] M. Brust, M. Walker, D. Bethell, D. J. Schiffrin, and R. Whyman, Synthesis of thiol-derivatised gold nanoparticles in a two-phase liquid-liquid system, *J. Chem. Soc., Chem. Commun.* **7**, 801 (1994).
- [32] S. Boroviks, C. Wolff, J. Linnet, Y. Yang, F. Todisco, A. S. Roberts, S. I. Bozhevolnyi, B. Hecht, and N. A. Mortensen, Interference in edge-scattering from monocrystalline gold flakes, *Opt. Mater. Express* **8**, 3688 (2018).
- [33] E. Krauss, R. Kullock, X. Wu, P. Geisler, N. Lundt, M. Kamp, and B. Hecht, Controlled growth of high-aspect-ratio single-crystalline gold platelets, *Crystal Growth & Design* **18**, 1297 (2018).
- [34] K. M. McPeak, S. V. Jayanti, S. J. Kress, S. Meyer, S. Iotti, A. Rossinelli, and D. J. Norris, Plasmonic films can easily be better: rules and recipes, *ACS Photonics* **2**, 326 (2015).
- [35] D. Krause, C. W. Teplin, and C. T. Rogers, Optical surface second harmonic measurements of isotropic thin-film metals: Gold, silver, copper, aluminum, and tantalum, *Journal of Applied Physics* **96**, 3626 (2004).
- [36] X. Wang, H. Shi, N. Wang, L. Cheng, Y. Gao, L. Huang, and Y. Jiang, Two-photon luminescence and second harmonic generation from gold micro-plates, *Sensors* **14**, 18328 (2014).
- [37] P. Biagioni, M. Celebrano, M. Savoini, G. Grancini, D. Brida, S. Mátéfi-Tempfli, M. Mátéfi-Tempfli, L. Duò, B. Hecht, G. Cerullo, and M. Finazzi, Dependence of the two-photon photoluminescence yield of gold nanostructures on the laser pulse duration, *Phys. Rev. B* **80**, 045411 (2009).
- [38] G. T. Boyd, Z. H. Yu, and Y. R. Shen, Photoinduced luminescence from the noble metals and its enhancement on roughened surfaces, *Phys. Rev. B* **33**, 7923 (1986).
- [39] S. I. Bozhevolnyi, J. Beer mann, and V. Coello, Direct observation of localized second-harmonic enhancement in random metal nanostructures, *Phys. Rev. Lett.* **90**, 197403 (2003).
- [40] O. Aksamitov, I. Baranova, and Y. A. Il'inskii, Surface contribution to the generation of reflected second harmonic light for centrosymmetric semiconductors, *Zh. Eksp. Teor. Fiz* **91**, 287 (1986).
- [41] L. Novotny and B. Hecht, *Principles of nano-optics* (Cambridge university press, 2012).

Authorship agreements

Authorship Agreement

This authorship agreement concerns the published research work conducted by PhD Student Sergejs Boroviks, Christian Wolff, Jes Linnet, Yuanqing Yang, Francesco Todisco, Alexander S. Roberts, Sergey I. Bozhevolnyi, Bert Hecht, and N. Asger Mortensen.

The research work includes following article:

Interference in edge-scattering from monocrystalline gold flakes
Opt. Mater. Express 8, 3688-3697 (2018)

In accordance with the criteria put forward at the Vancouver Convention for authorship (www.icmje.org), the undersigned Sergejs Boroviks hereby confirms that he as first author is responsible for the initial drafting of the article, a substantial contribution of the intellectual content, the acquisition and interpretation of experimental evidence, and finalization of the versions to be published.

Similarly, the undersigned Christian Wolff, Jes Linnet, Yuanqing Yang, Francesco Todisco, Alexander S. Roberts, Sergey I. Bozhevolnyi, Bert Hecht confirm that they as co-authors have contributed quantitatively and qualitatively to the conception and design, the interpretation of the experimental evidence, the critical revision for important intellectual content, and the final approval of the versions to be published.

As senior researcher, N. Asger Mortensen stands as guarantor and takes public responsibility for the integrity of the research work as a whole, from inception to published articles.



First author, Sergejs Boroviks



Co-author, Christian Wolff



Co-author, Jes Linnet



Co-author, Yuanqing Yang



Co-author, Francesco Todisco



Co-author, Alexander S. Roberts



Co-author, Sergey I. Bozhevolnyi



Co-author, Bert Hecht



Co-author, N. Asger Mortensen

Authorship Agreement

This authorship agreement concerns the published research work conducted by PhD Student Sergejs Boroviks, Francesco Todisco, N. Asger Mortensen and Sergey I. Bozhevolnyi.

The research work includes following article:

Use of monocrystalline gold flakes for gap plasmon-based metasurfaces operating in the visible
Opt. Mater. Express 9, 4209-4217 (2019)

In accordance with the criteria put forward at the Vancouver Convention for authorship (www.icmje.org), the undersigned Sergejs Boroviks hereby confirms that he as first author is responsible for the initial drafting of the article, a substantial contribution of the intellectual content, the acquisition and interpretation of experimental evidence, and finalization of the versions to be published.

Similarly, the undersigned Francesco Todisco and Sergey I. Bozhevolnyi confirm that they as co-authors have contributed quantitatively and qualitatively to the conception and design, the interpretation of the experimental evidence, the critical revision for important intellectual content, and the final approval of the versions to be published.

As senior researcher, N. Asger Mortensen stands as guarantor and takes public responsibility for the integrity of the research work as a whole, from inception to published articles.



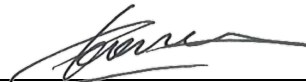
First author, Sergejs Boroviks



Co-author, Francesco Todisco



Co-author, N. Asger Mortensen



Co-author, Sergey I. Bozhevolnyi

Authorship Agreement

This authorship agreement concerns the research work conducted by PhD Student Sergejs Boroviks, Torgom Yezekyan, Álvaro Rodríguez Echarri, F. Javier García de Abajo, Joel D. Cox, Sergey I. Bozhevolnyi, N. Asger Mortensen, and Christian Wolff.

The research work includes following article:

Anisotropic Second Harmonic Generation From Monocrystalline Gold Flakes
Submitted to a journal. Available preprint: arXiv:2010.10982

In accordance with the criteria put forward at the Vancouver Convention for authorship (www.icmje.org), the undersigned Sergejs Boroviks hereby confirms that he as first author is responsible for the initial drafting of the article, a substantial contribution of the intellectual content, the acquisition and interpretation of experimental evidence, and finalization of the versions to be published.

Similarly, the undersigned Torgom Yezekyan, Álvaro Rodríguez Echarri, F. Javier García de Abajo, Joel D. Cox, Sergey I. Bozhevolnyi, and Christian Wolff confirm that they as co-authors have contributed quantitatively and qualitatively to the conception and design, the interpretation of the experimental evidence, the critical revision for important intellectual content, and the final approval of the versions to be published.

As senior researcher, N. Asger Mortensen stands as guarantor and takes public responsibility for the integrity of the research work as a whole, from inception to published articles.



First author, Sergejs Boroviks



Co-author, Torgom Yezekyan



Co-author, Álvaro Rodríguez Echarri



Co-author, F. Javier García de Abajo



Co-author, Joel D. Cox



Co-author, Sergey I. Bozhevolnyi



Co-author, Christian Wolff



Co-author, N. Asger Mortensen